Investigations of the Light Meson Spectrum with COMPASS using Final States containing Neutral Particles

Diploma Thesis

by

Stefan Pflüger

July 2011

Physik Department E18
Technische Universität München

Abstract

This thesis is dedicated to light meson spectroscopy, dealing with the classification and precise measurement of such states. In the year 2008, the COMPASS experiment at CERN collected data of diffractive production on a liquid hydrogen target, using a negative pion beam of 190 GeV. Using this data, several investigations in the light meson sector with the $\pi^-\pi^0\pi^0$ final state are performed in this thesis.
The first part of this thesis presents a cross-check of the two partial wave programs *compassPWA* and *rootPWA*, providing a general comparison and an exchange of information for both programs, helpful for the future developments. In addition, the agreement of the partial wave analysis results with the measured data is studied using the weighted Monte Carlo method.
The second part is dedicated to improvements of the $\pi^-\pi^0\pi^0$ event selection with respect to statistics and signal to background ratio. The performance of the individual improvements are studied with partial wave analysis, that are carried out on the data sets of these event selections. Finally, using the optimal event selection, a partial wave analysis was performed on the majority of collected data of the year 2008.

Contents

List of Figures

List of Tables

Chapter 1

Introduction

Over centuries the composition and characterization of matter has been one of the main fields of interests in physics. Today this branch of physics is known as particle physics and has reached a level of complexity that introduces many new challenges. On the one hand the energies needed to scan the yet unexplored mass ranges demand immense energies. On the other hand these observed particles may leave behind only little evidence, which then complicates their extraction from the overall measurement, requiring high statistics and precision.

Specifically the sub-topic of hadron spectroscopy, dealing with the classification and precise measurement of the vast amount of hadronic states, requires large statistics. Currently the Constituent Quark Model (CQM) classifies these states astonishingly well, despite its simplicity. However, as the interaction is only taken into account in form of an effective mass, Quantum-Chromo-Dynamics (QCD), the theory for strong interactions, already indicates some of the limits of the constituent quark model. From the classification of the quark model, if follows that certain combinations of quantum number for states are forbidden. Therefore an observation of such a state is a direct evidence for states beyond the CQM, and are explained in QCD as gluon contributions. These forbidden states by the quark model are called "spin-exotics".

A more thorough motivation will be given in chapter 2. Additionally the question of how one expects to produce such spin-exotic states is discussed in this chapter. Because the lifetime of produced states is extremely low, due to the scale of strong interactions, the decay products are actually measured in the experiment. As many different states are created which decay into the same final state, the overall measurement is a superposition of the energy dependent angular distribution of all these decay products. The procedure of the Partial Wave Analysis (PWA) can disentangle the various contributions from the overall measurement and is also presented in chapter 2.

This thesis is dedicated solely to the $\pi^-\pi^0\pi^0$ final state. Actually measurements in the charged channel $\pi^-\pi^-\pi^+$ are far easier and more precise, yielding higher statistics. The reason for studying the neutral $\pi^-\pi^0\pi^0$ final state next to the charged one, is the completely different type of detection, resulting in two independent acceptance corrections. Hence an observation of exotic signals in both channels strongly strengthens the overall result. The COMPASS[1] experiment, that performed the actual measurement in the year 2008, is introduced in chapter 3. Since COMPASS has many fields of research

[1] **CO**mmon **M**uon and **P**roton **A**pparatus for **S**tructure and **S**pectroscopy

combined into a single experimental setup, it is rather unique, and some of the physics topics of COMPASS are discussed in section 1.1.

At first a crosscheck of two partial wave analysis programs, *rootPWA* and *compassPWA*, used by the COMPASS collaboration, was performed. The reason for this crosscheck are the major changes undergone by *rootPWA*, developed at TUM. The crosscheck consists of two steps. At first the event selection, in which the measured data set is cleaned by removing different sorts of background. This is presented in chapter 4 in full detail. Once the correct subsample of data has been selected the actual PWA can be carried out. The comparison of the performance of both frameworks is given in chapter 5. In particular the goodness of the fits, in the sense how well they describe the measured data, are also studied in this chapter.

Beyond the crosscheck, improvements on the event selection and their influence on the results of the PWA are studied in chapter 6. Because for the above analysis, only a subset of the complete 2008 data was used to find the optimal event selection, it was then applied to the full statistics, and the results of this partial wave analysis are presented in chapter 7.

1.1 Physics Topics of COMPASS

As mentioned above, COMPASS has several fields of research combined in a single experimental setup. These topics can roughly be categorized by the type of particle beam that is used to perform the measurements.

The hadron program is concerned with the topic of hadron spectroscopy and macroscopic properties of hadrons, i.e. magnetic moments. In particular the topic of this thesis, low meson spectroscopy, falls into the category of the hadron program. Because this is presented in full detail throughout the thesis, it is not discussed in this section any further. Beyond this, the hadron beam program studies the Primakoff production mechanism. In such a process the beam pion is excited via a photon and an additional bremsstrahlung gamma is present in the final state. From this the pion polarizibility can be extracted and compared with results obtained from chiral pertubation theory χPT [13].

The muon program is devoted entirely to the internal structure of the hadrons. One of the topics is the measurement of the nucleon spin contributions from its constituents. Because the contributions of the quarks is small, the gluon components are of special interest. From the cross-section helicity asymmetry of the photon-gluon fusion (PGF), $\gamma^* g \to q\bar{q}$, the gluon polarization $\Delta G/G$ was measured at COMPASS [7].

Another topic of the muon program, is the more detailed specification of the quark structure of the nucleon. In principle one gains insight into the structure by deep inelastic scattering (DIS). The Parton Model describes QCD processes happening in this region of kinematics. Quantities which are determined from such measurements are the parton momentum distributions $q(x)$, where x is the Bjorken variable. Beyond this, taking into account the transverse spin distributions $\Delta_T q(x)$, they must be added to the momentum distributions $q(x)$ and the helicity distributions $\Delta q(x)$. At COMPASS these transverse spin distributions were measured from the single-spin asymmetries in cross-sections for semi-inclusive DIS (SIDIS) of muons on a transversely polarised target [8].

Chapter 2

Theory

The theoretical background that motivates the analysis is presented in this chapter. This will then lead to the analysis techniques that have to be applied in order to gain insight into the hadronic spectrum.

In the beginning the Constituent Quark Model is introduced, generating a model spectrum that is able to classify the majority of hadrons astonishingly well. However, certain combinations of quantum numbers classifying the individual states are forbidden in this model. As the fundamental theory for strong interactions is Quantum Chromo Dynamics (QCD), additional degrees of freedom are attributed to the states by the gluons. In order to avoid disentangling the gluon components of the states, one focuses on the states that are not allowed in the quark model.

Then the production mechanism of such states and the theoretical approach on how to extract this information from a measurement is presented. In reality however, the work has to be carried out in reverse order. The energy dependent angular distribution of the final state particles allows the reconstruction of originally produced state and its quantum numbers. This can be achieved with a Partial Wave Analysis (PWA) which is discussed at the end of this chapter.

2.1 The Constituent Quark Model

The Constituent Quark Model [21] was brought to life by the large number of states that rapidly filled the hadron spectrum and needed to be classified. In this model, bound states consisting of a quark-antiquark pair are referred to as mesons, while three-quark systems generate the baryon spectrum. Since no statements for the interactions between the quarks are made, the full information is distributed to the constituent quarks themselves. Symmetry principles generating the ground state quantum numbers help classifying the spectrum. The great success of the model was the prediction of states that were later successfully discovered. Despite its simplicity, the model is able to handle the large number of hadronic states astonishingly well. Since the analysis presented in this thesis is concerned only with the low mass meson part of the full hadron spectrum, this region is presented in more detail.

The simplest stage of the model is constructed by only considering two quarks, up and down, described by the $\mathrm{SU}(2)_{\mathrm{isospin}}$ group. Both the up and down quark form an isospin I doublet (u, d), and are identified by their z-projection I_z (u: $I_z = +1/2$; d: $I_z = -1/2$). Together with the antiquark doublet $(-\bar{d}, \bar{u})$, similar to the normal spin coupling, this generates a triplet ($I = 1$) and a singlet state ($I = 0$). The triplet consists of the three pions π^+, π^- and π^0. Apart from small corrections due to e.m. interactions, these three pions should carry the same mass within this model, since they belong to the same triplet. Measurements reveal a mass difference between the charged pions and the neutral pion which can only be accounted for by additional weak explicit breaking of the $\mathrm{SU}(2)_{\mathrm{isospin}}$ group.

Historically it was necessary to introduce a third quark, the so-called strange quark, to explain the slow decays of a number of particles [19]. The symmetry group is then extended to the $\mathrm{SU}(3)_{\mathrm{flavour}}$ group, which induces additional meson states that are grouped into a flavour octet and a singlet. These three quark flavours construct the so-called light meson spectrum, and simply this part of the full spectrum is regarded in this thesis. Then only the isospin I, its z-component I_z and the strangeness S are needed for the classification so far. For the special case of a states with only net ud quark flavour, the strangeness and higher quark flavour quantum numbers are zero and therefore I and I_z fully describe the flavour content of the created state. The justification for the use of this special case is given in section 2.3.

Including the spin $1/2$ of the quarks, the formed bound states can carry a total intrinsic spin S of either 0 or 1 by addition of spins. Altogether, without orbital excitations ($L = 0$), the $\mathrm{SU}(3)_{\mathrm{flavour}}$ group and spin coupling generates two nonets, one for pseudoscalar mesons and a second nonet for the vector mesons[1]. This is depicted

[1] The terminology of the naming scheme considering the spin of the meson arises from the representations of the $\mathrm{SU}(2)_{\mathrm{spin}}$. Spin 0 particles are described by the scalar or pseudoscalar representation, while pseudo has the meaning of an opposite signed phase under the parity transformation. The vector and pseudo-vector representation are used for particles of spin 1. Because the mesons carry an intrinsic parity phase of -1, only the pseudo-scalar and vector representation give the correct transformation properties. Note that orbital excitations can produce higher total spins J and positive

in figure 2.1.

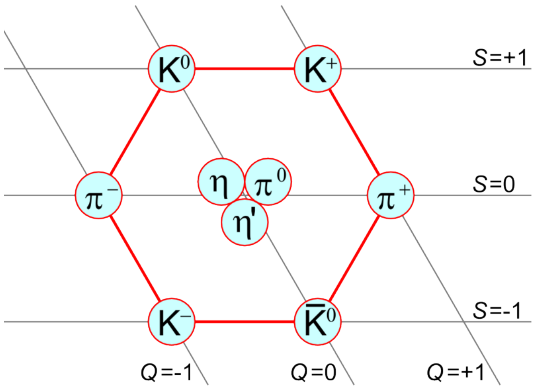

(a) Spin 0 meson nonet

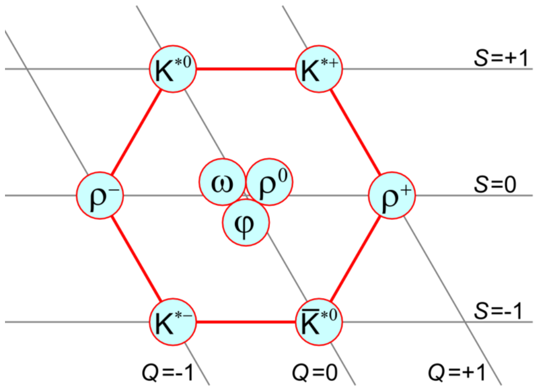

(b) Spin 1 meson nonet

Figure 2.1: Meson nonets generated from the $\mathrm{SU}(3)_{\text{flavour}}$ group together with intrinsic spin coupling [3].

Mass differences of these states arise from the different quark contents and the spin-spin interaction, which is equivalent to the hyperfine-splitting in atomic physics. Note that the spin-spin interaction generates large mass splittings of about 600 MeV between the π and ρ states.

Similar to the atomic energy spectrum a meson can have radial and orbital excitations, given by the principal quantum number n and the orbital angular momentum L. The construction of the total spin $J = L \oplus S$ of the state is done by addition of angular momenta. The combination of these quantum numbers characterize the excitation of a given quark content, denoted by ${}^{2S+1}_{n}L_J$. The additional mass differences between these excitations arise from the radial excitations and the fine-splitting[2]. Figure 2.2 shows the qualitative classification of the low-mass meson spectrum generated from the $\mathrm{SU}(3)_{\text{flavour}}$ group.

Alternatively for the description for these states the parity $\mathcal{P}$ and the charge conjugation parity $\mathcal{C}$ can be used. However only flavour-neutral states are eigenstates of the charge conjugation operator, and their eigenvalue C can be measured individually. This can be extended to the $\mathcal{G}$-parity operator, for which all mesons of the ud-quark sector are eigenstates. It is defined as a combination of charge conjugation and a π rotation around the y-axis of isospin space $\mathcal{G} = \mathcal{C}e^{(i\pi I_y)}$, and yields the same eigenvalues for all states in a given multiplet. Even though the specification of the $\mathcal{C}$-parity phase is now redundant, it is common to assign the remaining particles of a multiplet the same phase as its flavour neutral partner.

Above it was mentioned that the $\mathcal{P}$ and $\mathcal{C}$ operators can be used for an alternative

parity phases. This is explained below in more detail.

[2]Just as in atomic physics the fine-splitting arises from the interactions of the magnetic moments generated from the orbital angular momentum and the spin.

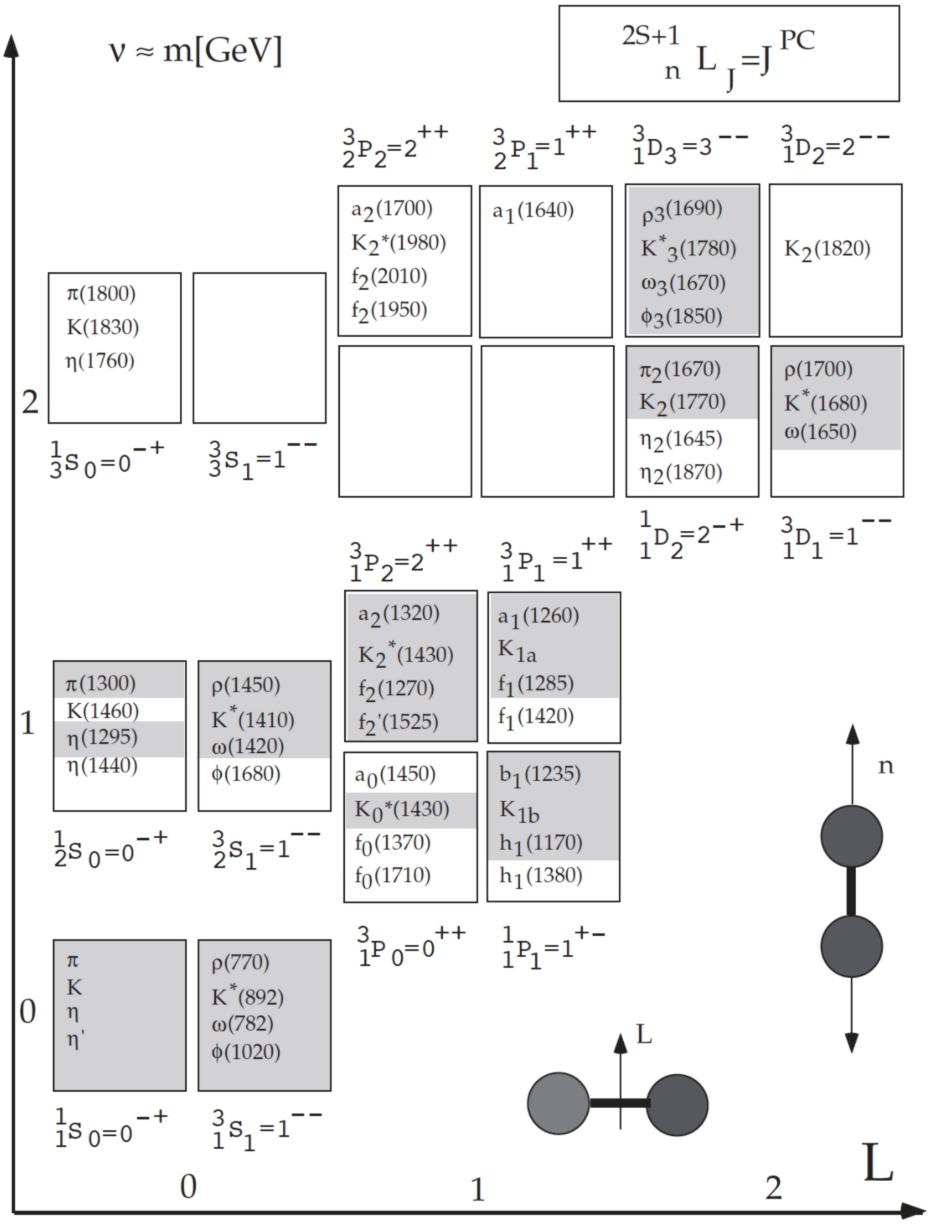

Figure 2.2: The low mass meson spectrum from the naive quark model point of view. The state excitation is fully described by the principal quantum number n, total spin J, angular momentum L and intrinsic spin S. The horizontal axis denotes the L, while the vertical axis with $\nu = n + L - 1$ gives an approximate mass scale. This is based on the similar mass contributions of the orbital and radial excitations and treats them on an equals footing. Each box represents a flavour nonet, while the assignments of the shaded particles are clear and definite [12].

$q\bar{q}$ content	${}^{2S+1}L_J =$ J^{PC}	^{1}(L even)$_J$ $0^{-+}, 2^{-+} \cdots$	^{1}(L odd)$_J$ $1^{+-}, 3^{+-} \cdots$	^{3}(L even)$_J$ $1^{--}, 2^{--}, 3^{--} \cdots$	^{3}(L odd)$_J$ $0^{++}, 1^{++}, 2^{++} \cdots$
$u\bar{d}$, $d\bar{d} - u\bar{u}$, $d\bar{u}$		π	b	ρ	a
$d\bar{d} + u\bar{u}$, $s\bar{s}$		η, η'	h, h'	ω, ϕ	f, f'
$c\bar{c}$		η_c	h_c	ψ	χ_c
$b\bar{b}$		η_b	h_b	Υ	χ_b

Table 2.1: Classification of mesons with no total strangeness, charm or bottomness [24]

classification scheme. This means that they are dependent of the operators L, S. Below an overview of the phases created from $\mathcal{P}$, $\mathcal{C}$ and $\mathcal{G}$ for non-strange mesons and their relations to L, S and I are shown.

- $P = (-1)^{L+1}$
- $C = (-1)^{L+S}$
- $G = C(-1)^I = (-1)^{I+L+S}$ where I is the isospin

The $\mathcal{P}$-parity phase consists of the angular momentum part $(-1)^L$ due to the transformation properties of the spherical harmonics. Additionally a quark-antiquark pair carries an intrinsic parity of $P_{q\bar{q}} = -1$, which is a direct consequence of the Dirac equation [27]. Altogether we end up with $P = (-1)^{L+1}$, which was stated above. The derivation of the charge conjugation parity relation is similar. By first exchanging $q \leftrightarrow \bar{q}$ a minus sign arises from interchanging fermions. Then interchanging position and spin, factors of $(-1)^L$ and $(-1)^{S+1}$ are gained, respectively. The combined operation gives the stated result. In analogous form the $\mathcal{G}$ parity phase is determined [26].

In principle the z component of the total spin, whose eigenvalue is denoted by M_J, is the last degree of freedom that identifies the state. However unless a magnetic field is applied these states are energetically degenerate. Because the total angular distribution of the final state particles depends on the spin projection M_J of the created states, this quantum number is important for the partial wave analysis procedure. Section 2.4 explains this in more detail. Table 2.1 shows the naming scheme of the light mesons, as developed so far.

To sum up, for the special case of only net ud-quark flavour the states are entirely defined by $I^G J^{PC} M_J$. Because the I_z is now in a one-to-one relation with the electric charge, the latter is more commonly used. However, in case the small mass shifts within a multiplet no longer can be resolved, i.e. for states of higher mass, this information is omitted and the multiplet is treated collectively. It is worth noting that certain J^{PC} combinations are forbidden within the quark model as for example the 0^{--}, 0^{+-} or 1^{-+}.

2.2 Quantum Chromodynamics and Spin Exotic States

The meson spectrum was purely built up by the quark model, however the well established fundamental theory for strong interactions is Quantum Chromodynamics (QCD). The spectrum from the QCD point of view in comparison to the simplified quark model is now of interest. The special property of QCD are its force mediators, the gluons, that carry color charge themselves. This is achieved by generating gluons from the $SU(3)_{\text{color}}$ group, in which the non-abelian character of the group provides the gluon self interactions. Consequently there are two crucial effects arising from this property.

- confinement (absence of free quarks)
- asymptotic freedom

The second property makes the perturbative expansion of QCD possible, but only in the regime of high momentum transfers, hence irrelevant for the study of bound states. The first property complicates this study since one cannot decompose the state into its constituents, as compared to the atom. Theoretical calculations can be made by lattice QCD, in which the theory is formulated on a grid in space and time [29]. However computation power limits the size of this lattice and therefore the approach is still at a rudimentary stage. Also despite the ability to make predictions of some properties of the states, for instance masses, the deeper structure of the strong binding force is hidden beneath this numerical procedure. There are several effective theories taking the gluon potential into account, i.e. the flux tube model or bag models [22, 23]. The common denominator of all these models are the gluons that can be a constituent of the meson by its self interaction and hence contribute to the quantum numbers of the state. Moreover all J^{PC} combinations are allowed by QCD.

In general a mesonic state has the following color-singlet Fock expansion.

$$|\text{meson}\rangle = c_1 \cdot |q\bar{q}\rangle + c_2 \cdot |q\bar{q}g\rangle + c_3 \cdot |gg\rangle + c_4|qq\bar{q}\bar{q}\rangle + \cdots$$

Here $|q\bar{q}\rangle$ represents the normal quark-antiquark contribution known from the quark model. $|q\bar{q}g\rangle$ is the simplest hybrid term, which additionally has a gluon contributing to the quantum numbers of the observed state. Another portion of the state can be purely made of gluons $|gg\rangle$, in its simplest form consisting of two gluons that generate the quantum numbers of the state. Tetraquarks $|qq\bar{q}\bar{q}\rangle$ consist of four valance quarks. In principle the mixing of these different terms for a meson state could be disentangled by analysing the full decay scheme. However instead of measuring the absolute values of the probability constants c_i one can simplify the goal by measuring the c_i to be unequal to zero with $i > 1$. This can be achieved by looking at states with J^{PC} combinations that are forbidden by the quark model, i.e. 1^{-+}, making the natural quark model component $c_1 = 0$. Therefore an observation of such a spin-exotic state provides direct evidence for states beyond the simple quark model, and can be explained within QCD via gluon contributions.

2.3 Diffractive Dissociation

For the creation of these J^{PC} exotic states, there are two types of production mechanisms. On the one hand, in formation processes, typically e^+e^- or $p\bar{p}$ annihilations, the created states are entirely defined by the initial state, since there is no recoil particle. Thus mesons with exotic quantum numbers can in general not be created primarily. However, they become accessible through the decay products of the primary produced states [28].

On the other hand, in production processes the quantum numbers of the created state are shared with the recoil particle and only constrained by conservation laws. In particular states with exotic quantum numbers are directly accessible. Further classification can be made into diffractive and central production processes, which can both be studied at COMPASS.

In this thesis only the diffractive dissociation production process

$$\pi^- A \to X A' \to H_1 \cdots H_N A'$$

is studied. Here A denotes the target particle, X the produced state, and H_i the final state hadrons that appear from the resonance decay. A' represents the recoiling target particle which has not been excited, but just carries the momentum transferred in the reaction.

Because the total cross section is a superposition of amplitudes from various production mechanisms, all of these contributions have to be regarded in principle. On the one hand, scattering on the target or its constituents, in this case nucleons or quarks and gluons, occurs collectively and individually contribute to the total cross section. Because the cross sections of these different processes feature diverse dependencies on the momentum transfer t of the reaction, usually certain t-regimes exist, in which a specific process is dominant. More precisely, for low momentum transfers, incoherent scattering on the target is virtually the only process contributing to the total cross section. Moving to higher t, the contributions of scattering on the constituents carry more and more weight. Therefore, as incoherent scattering on the target is desired here, the momentum transfer must be constrained from above accordingly. Once restricted to a certain t-range, only the dominant process is regarded in good approximation. In this case, the diffractive dissociation production process is similar to black disc diffraction in optics.

On the other hand there are multiple mechanisms, from an exchange particle point of view, contributing to the total cross section. However, from Regge theory [15] and validating measurements the dominant production mechanism at high center of mass energies $\sqrt{s}$ is t-channel pomeron exchange. Due to the high beam energies of 190 GeV at COMPASS, the major cross section contributions arise from pomeron exchange and in an additional good approximation only this mechanism is regarded. This reaction is depicted in figure 2.3a and its characteristics are described in more detail below.

The exchange particle, the pomeron, is a Regge trajectory that may be visualized as a gluon string that only carries angular momentum and otherwise the quantum

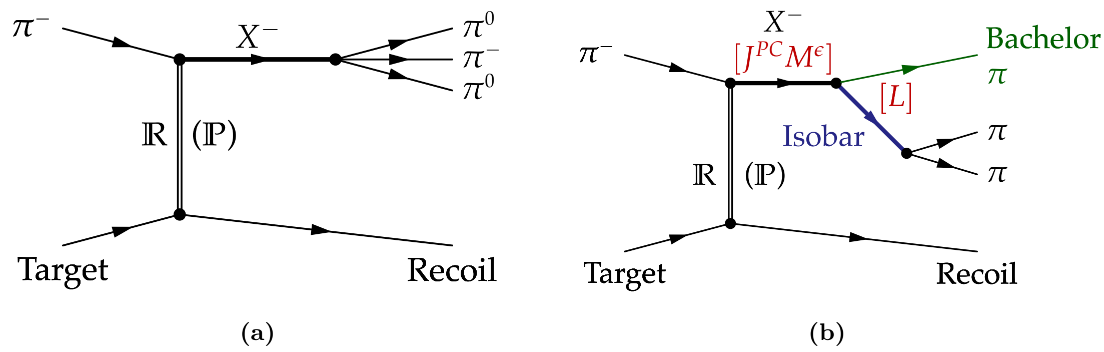

Figure 2.3: (a): The dominant diffractive dissociation production process at high c.m. energies. **(b):** The diffractive dissociation process in combination with the isobar model. Since the $\pi^-\pi^0\pi^0$ decay channel is analysed, the isobar can either be charged or neutral, decaying into $\pi^-\pi^0$ or $\pi^0\pi^0$, with the bachelor pion being the remaining π^0 or π^-. To stay general the final state pions were left undetermined (courtesy of Boris Grube).

numbers of the vacuum[3]. Therefore all quantum numbers of the resonance except J^P are identical to the incoming beam pion. For this explicit case the accessible meson spectrum is $1^- J^{P+}$

Note that the above assumption of no net flavour being introduced to the produced state is obviously satisfied, as long as the target stays intact. Even if recoil is not measured, only a small background of this kind will be present, because the dominant pomeron exchange does not introduce any flavour.

2.4 Partial Wave Analysis

In principle the invariant mass spectrum of the final state displays the distribution of the created states. But here problems arise, as the most intense states overwhelm the small contributions of other states. In addition, the interference and overlap of states makes the extraction of the individual contributions impossible in this way. However, the method of partial waves in combination with the isobar model is able make such an evaluation.

The isobar decay model regards the full decay as multiple successive two particle decays, as shown in figure 2.3b. The theoretical inability to fully describe decays with 3 or more final state particles, makes the isobar model an inevitable component. However the Dalitz plots in chapter 7 verify that such isobar decays exist in nature and enforces the use of the model. In particular the term isobar is used for non-final state particles appearing in the decay. In case a final state particle originates from a two particle decay, while its decay partner is an isobar, the former is also known as a bachelor particle.

The partial wave analysis procedure extracts the individual contributions of states

[3]The vacuum carries the $\mathcal{C}$ parity phase of $C = 1$ and a $\mathcal{G}$ parity phase of $G = 1$.

of the total invariant mass spectrum from the measured angular and energy dependent intensity of the final state particles. This is usually done in a two step procedure.

At first the mass-independent fit is performed. The data is divided into final state invariant mass bins, neglecting the invariant mass dependence within each bin. For each bin a separate fit is executed with the advantage of not making any assumptions on the mass dependence of the created state. Furthermore for a continuous development of fit results over the bins, the ansatz is confirmed. Because no assumptions on the mass dependence of the created state are made, the disadvantage is the inability to extract the quantities like the mass and width of X.

Therefore a second fit that carries a mass dependence for the state, e.g. in form of relativistic Breit-Wigner functions, is performed. This model is fitted to the results of the mass-independent fit for a subset of the most intense waves. Because this step was omitted in the analysis of this thesis, the details of this procedure will not be described here.

For the mass-independent fit, the basic approach is to create a theoretical energy dependent angular distribution of the final state particles as a coherent sum of partial waves. Each partial wave describes a unique decay path defined by the quantum numbers of X and the intermediate isobar, as shown in figure 2.3b. This model is then fitted to the measured data, resulting in the production amplitudes that give information on the intensities of the individual waves and their phases.

The model of the mass-independent fitting procedure is summarized by equation 2.1.

$$\sigma(\tau; m_X) = \sum_{\epsilon=\pm1} \sum_{r=1}^{N_r} \left| \sum_{i}^{\text{waves}} T_{ir}^{\epsilon}(m_X) \psi_i^{\epsilon}(m_X, \tau) \Big/ \sqrt{\int |\psi_i^{\epsilon}(\tau')|^2 \, d\tau'} \right|^2 \tag{2.1}$$

The appearing variables have the following meanings and are described below in more detail.

- ϵ, i: quantum numbers of the partial wave
- N_r: rank of the fit
- $T_{ir}^{\epsilon}(m_X)$: production amplitude (complex number); fit parameter
- $\psi_i^{\epsilon}(\tau)$: decay amplitude (complex functions)
- τ: phase space variables

Each partial wave of a given mass bin, is composed of a production amplitude T_{ir}^{ϵ} and a decay amplitude ψ_i^{ϵ}, while the former is a fit parameter and the latter carries the model dependency and is calculable. In order to factorize the decay and production amplitudes, it was assumed that the states were actually existent and have no memory of their creation.

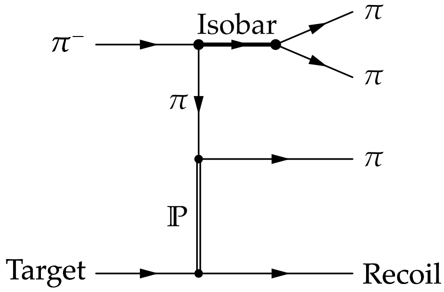

Figure 2.4: Feynman-like diagram of Deck effect (courtesy of Boris Grube).

Because only the final state is measured, there are interferences with other production mechanisms in which no intermediate state X was created. One such parasitic process is shown in figure 2.4, and is known as the Deck effect [16]. Of course for a complete study, the background produced by these production mechanism to the diffractive dissociation process has to be examined, but is not considered in this thesis. Hence, the model expressed by equation 2.1 only includes the contribution expressed by figure 2.3b. Note that the production amplitudes also contain the coupling constants of decay vertices.

As explained above the decay amplitudes make use of isobar decay model, in which the full decay is expressed in multiple successive two particle decays. Two body decays are completely defined by 3 variables, the parent mass and two angles describing the direction of emission of the decay products. For the case of a three pion final state, there are 6 phase space variables: the mother state mass m_X, two angles for its decay in the Gottfried Jackson frame[4] θ_{GJ}, ϕ_{GJ}, the isobar mass m_I and two angles for its decay in the Helicity frame[5] θ_H, ϕ_H. Because of the binning in the 3π-invariant mass, m_X is fixed and the number of phase space variables is reduced to the remaining 5 variables $\tau = \{\theta_{GJ}, \phi_{GJ}, m_I, \theta_H, \phi_H\}$.

Adhering to the case of the three pion final state, the full decay amplitude is factorized by the isobar model into $\psi_i^\epsilon(\tau) = \psi_i^\epsilon(m_X, \theta_{GJ}, \phi_{GJ}) \cdot \psi_i^\epsilon(m_I, \theta_H, \phi_H)$. In general each two body decay amplitude has a dynamical and orbital component. The orbital part is more or less given by the spherical harmonics which are well understood and fixed quantities. The dynamical part incorporates the information of the binding force creating the bound isobar state and is usually approximated with relativistic Breit Wigner functions. One example for an exception, that is also present in the analysis, is the $f_0(600)$ or σ state which is a very broad and loose defined structure. The parametrization of the isobars carries the largest uncertainty to the description of the data. Altogether, the spacial energy distribution of the final state given by these decay amplitudes depends on the quantum numbers of the state, here denoted by ϵ and i.

Figure 2.3b already shows the full set of quantum numbers for a specific partial wave, denoted by $J^{PC}M^\epsilon\text{Isobar}_1[L]\text{Isobar}_2$. As these quantum numbers are all discrete, they are all, with the exception of the reflectivity ϵ, combined into the quantum number i. Note that here the quantum number M is not identical to the total spin z-projection M_J, but arises from a basis transformation together with the new quantum number ϵ, known as the reflectivity.

[4]The GJ frame is defined in the rest frame of the intermediate state X, with the z-axis parallel to the beam particle and the y-axis perpendicular to the production plane.

[5]The helicity frame is constructed by rotating the z-axis of the parent frame into the direction of the momentum of the isobar and then boosting along this direction so that the isobar is at rest.

$$|J^P\, M\epsilon\rangle = \theta(M)\big[|J^P\, M\epsilon\rangle - \epsilon P(-1)^{J-M}|J^P\,\text{-}M\epsilon\rangle\big]$$

$$\theta(M) = \begin{cases} 1/\sqrt{2} & M > 0 \\ 1/2 & M = 0 \\ 0 & M < 0 \end{cases}$$

While the normal z-projection of the total spin J can acquire the following values $J \geq M_J \geq -J$, the new z-projection is constrained to $J \geq M \geq 0$. The remaining degree of freedom is restored by the reflectivity $\epsilon = \{+, -\}$. Note that for $M = 0$ only a positive reflectivity is defined.

The motivation for this basis transformation is twofold. The reflectivity operator is defined to generate a reflection through the production plane, which is spanned by the incoming beam particle and the outgoing resonance X. Therefore it is equivalent to the parity operator followed by a rotation of π around the production plane normal vector. Parity conservation now forbids the mixing of different values of ϵ, which makes the sum over this quantum number non-coherent [10]. This reduces the number of fit parameters by a factor of 2, which not only makes the fit faster but also more stable.

Additionally the reflectivity quantum number was defined to coincide with the naturality of the exchanged particle [9]. The naturality $+1$ of the pomeron restricts partial waves to carry mainly positive reflectivity, while the negative reflectivity waves should be strongly suppressed. Therefore waves with negative reflectivity could in principle be omitted, again reducing the number of partical waves. Nevertheless, some waves with $\epsilon = -1$ are included in fits to examine their suppression.

The quantum number L describes the angular momentum between the isobar and the bachelor pion, which should not be confused with the angular momentum of X, as they are in general not the same.

Another incoherent summation comes from the rank of the fit, denoted by N_r. As one can see from equation 2.1 only the production amplitudes depend on this variable. By setting $N_r = 2$ the target proton spin flip and non-flip situations are treated incoherently.

In equation 2.1, the phase space MC integral of the decay amplitudes is merely a technicality, normalizing the production amplitudes T^{ϵ}_{ir} to ensure additional fitting stability.

Now that the theoretical model is available this has to be fitted to the data, the measured energy dependent angular distribution of final state particles. For this an extended maximum log likelihood method is used. The parametrization of the total likelihood for a specific invariant mass bin m_X is shown in equation 2.2.

$$\mathcal{L}(m_X) = \underbrace{\left[\frac{\bar{N}^N}{N!}e^{-\bar{N}}\right]}_{\text{Poisson}} \prod_{n=1}^{N} \underbrace{\left(\frac{\sigma(\tau_n; m_X)}{\int d\tau' \sigma(\tau'; m_X)\text{Acc}(\tau'; m_X)}\right)}_{\substack{\text{Normalized acceptance corrected} \\ \text{likelihood for event } n}} \tag{2.2}$$

Statistical fluctuations of the number of events N in the invariant mass bin m_X are accounted for with the Poisson distribution normalization factor, where $\bar{N}$ denotes the expected number of events.

$$\bar{N} = \int d\tau' \sigma(\tau'; m_X) \mathrm{Acc}(\tau'; m_X) \tag{2.3}$$

The latter factor in equation 2.2 is the product of likelihoods, in which equation 2.1 gives the individual likelihood for an event n with phase space variables τ_n. Each such likelihood is normalized by the phase space MC so that the obtained production amplitudes correspond to the number of events. Also at this point the acceptance of the measured data is taken into account.

Using equation 2.3, the total likelihood can be simplified to

$$\tilde{\mathcal{L}}(m_X) = e^{-\bar{N}} \prod_{n=1}^{N} \sigma(\tau_n; m_X). \tag{2.4}$$

Since the factor $\frac{1}{N!}$ is constant, it is irrelevant to the maximization and can be dropped.

Because finding the maximum over this large product is unpractical, a logarithm of the total likelihood is taken at which point the product turns into a sum. This is possible because the logarithm is a strictly increasing function and the total likelihood $\mathcal{L}(m_X)$ in equation 2.1 is positive. Applying the logarithm on 2.4 and inserting equation 2.1, one arrives at 2.5.

$$\ln \tilde{\mathcal{L}}(m_X) = \sum_{n=1}^{N} \ln \sum_{\epsilon,r,i,j} T^{\epsilon}_{ir}(m_X) T^{\epsilon *}_{jr}(m_X) \psi^{\epsilon}_{i}(\tau_n) \psi^{\epsilon *}_{j}(\tau_n) - \int d\tau' \sigma(\tau'; m_X) \mathrm{Acc}(\tau'; m_X) \tag{2.5}$$

Once the fit was successful a set of production amplitudes are now at hand. By reformulating equation 2.1 into equation 2.6, in which the spin density matrix ρ^{ϵ}_{ij} appears, the physical quantities can easily be extracted.

$$\rho^{\epsilon}_{ij} = \sum_{r}^{N_r} T^{\epsilon}_{ir} T^{\epsilon *}_{jr} \qquad \sigma(\tau; m_X) = \sum_{\epsilon} \sum_{i,j} \rho^{\epsilon}_{ij}(m_X) \psi^{\epsilon}_{i}(\tau) \psi^{\epsilon *}_{j}(\tau) \tag{2.6}$$

The diagonal elements ρ_{ii} are real values that represent the intensities for each wave, while the off-diagonal elements $\rho_{ij,i\neq j}$ are complex numbers that stand for the interference terms from which phases are gained. Since a resonance typically exhibits a phase motion of π, it is a smoking gun evidence if such a shift is observed. However only relative phase shifts between two individual waves are measured. Though especially waves with lower intensities the statistical errors become larger and obscure the resonance structure, and phase shifts can help clarify the observation.

There is a general complication with this procedure. In principle the waveset has to be infinite, since unitarity requires all possible decay patterns. However the feasibility forces the use of a finite set, since an infinite summation is impossible in practice. Additionally the statistics are limited and so must be the wave sets, to keep the errors at an acceptable level.

Finally a weighted Monte Carlo procedure can be used to compare the fitted result with the real data. Here the phase space MC events that were already generated for the normalization of the decay amplitudes are weighted according to the results of the fit and can then be compared to the real data. Note that a missing acceptance correction can worsen the overall fit results, because the fit is forced on these “unnatural” distributions. Hence fit results have to be regarded with some caution in case the acceptance correction is absent.

Chapter 3

The COMPASS Experiment

This chapter deals with the experimental task of measuring the energy dependent spatial distribution of the decay products arising from the diffractively produced states at COMPASS. Measurements in general would include the determination of all decay- and production vertices as well as the identification and measurement of 3 momentum for all particles appearing in the reaction. On the basis of this the apparatus will be introduced, with special emphasis on the detectors that are critical for the reconstruction of the data used in this analysis.

The $\pi^-\pi^0\pi^0$ channel involves the detection of neutral particles, which cannot be tracked. In order to reconstruct their direction of flight, vertex information has to be included. All of this will be addressed in section 3.2, where the detector setup is presented.

The remainder of the chapter will be spent to provide a short overview of the triggering as well as data acquisition and processing at COMPASS. However, before going into COMPASS-specific details, a brief presentation of CERN[1] accelerator complex and how the beam actually reaches the COMPASS hall is given.

[1]provisional name was **C**onseil **E**uropéen pour la **R**echerche **N**ucléaire and changed to the official name European Organization for Nuclear Research

3.1 COMPASS at CERN

3.1.1 The CERN Accelerator Complex

The COMPASS experiment is located near Geneva, Switzerland in the CERN North Area (NA). An overview of all the accelerators and experiments at CERN is shown in figure 3.1. The array of accelerators enable a variety of experiments to simultaneously obtain different beam energies. The specific particle species which can be handled by the various accelerators can be taken from figure 3.1.

For COMPASS, protons are first accelerated by a linear accelerator (LINAC2) to an kinetic energy of 50 MeV and injected into the Proton Synchrotron Booster, that increases their kinetic energy to 1.4 GeV. They are then fed into the Proton Synchrotron (PS) that will reach energies of approximately 30 GeV. Afterwards the Super Proton Synchrotron (SPS) accelerates the protons upto 400 GeV. At this point a fraction of the protons are extracted for the COMPASS experiment. However, the most prominent recipient of the SPS protons is the Large Hadron Collider (LHC) working at proton energies of about 3.5 TeV.

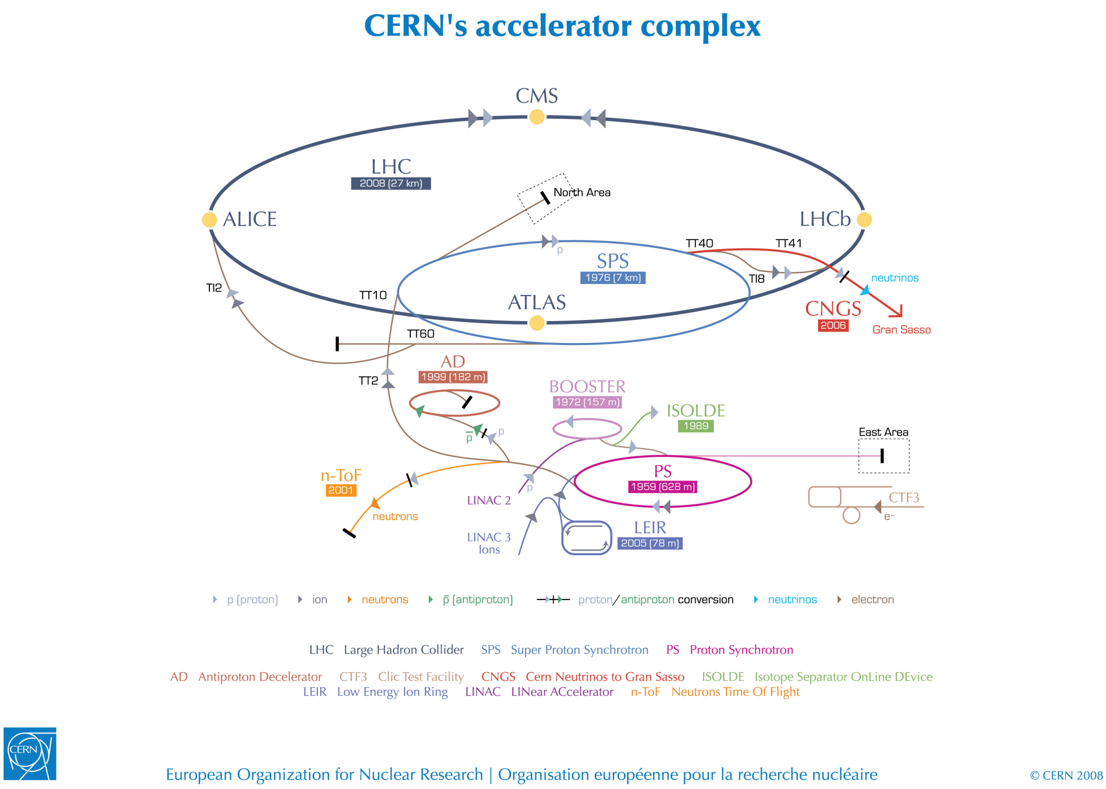

Figure 3.1: The CERN accelerator complex [4]

3.1.2 Beams and the M2 Beamline

As already pointed out in chapter 1, many different measurements are performed at COMPASS, all concerning the composition of hadrons. Two different type of beams are used.

Figure 3.2: The M2 Beamline. For hadron beams the hadron absorber as well as the BMS is removed [5].

The M2 beamline connects the COMPASS experiment to the SPS, which can be seen in figure 3.2. At first the SPS proton beam impinges on the production target (T6), which is similar to the cylinder of a revolver. Each slot of the cylinder contains a beryllium target of different length. A 500 mm long target is used at the nominal running conditions. Thinner beryllium targets can be selected to attain a lower secondary particle flux, that is useful for detector tests. Approximately 10^{13} protons are delivered to the production target per spill cycle with a duration of 9.7 s compared to the entire cycle of 45 s. Inside the target the protons create hadronic showers, producing a variety of particles. The secondary beam consisting mainly of pions, kaons and protons/antiprotons, because their lifetime is long enough to reach the COMPASS hall.

Note that, for the hadron beams no momentum measurements are performed, because the only available beam momentum station (BMS) has a too large interaction length, which would cause unwanted hadron showers. Therefore the beam momentum is uncertain to about 3 %.

As the beams are in general not pure, summarized in table 3.1, it is useful to provide particle identification (PID) for the beam particles. In 2008 this was realized for the first time in COMPASS with two CEDAR[2] detectors. The Cherenkov radiation emitted by the traversing particles is focused by a mirror system onto a ring of photomultiplier tubes. By adjusting the gas pressure inside the detector the angle of emission can be regulated. Then a specified range of beam velocities is mapped onto the PMT ring. Because some of the velocities of different beam particles only carry small deviations, a diaphragm is used to additionally narrow the interval of beam velocities. This detector allows real time beam PID making it a possible trigger component. Of course, exclusively a single particle type can be positively identified.

The muon beam is created by pion decays along the decay tunnel of the M2 beam line and is naturally polarized because of the parity violation of the weak decay. By inserting

[2] **Ch**E**renkov** **D**ifferential counter with **A**chromatic **R**ing Focus

Beam parameters	Muon beam	Hadron beam
Beam particle mix (+)	μ^+ only	71.5% p, 25.5% π^+, 3.0% K^+
Beam particle mix (−)	μ^-, e^-	95.0% π^-, 4.5% K^-, 0.5% $\bar{p}$
Beam momentum	$\sim 160\,{}^{\mathrm{GeV}}/_{c}$	$\sim 190\,{}^{\mathrm{GeV}}/_{c}$
Beam flux per SPS cycle	$2 \cdot 10^8$	$\leq 10^8$
Spot size at target ($\sigma_x \times \sigma_y$)	$8 \times 8\,\mathrm{mm}^2$	$3 \times 3\,\mathrm{mm}^2$
Beam polarisation	$80 - 90\,\%$	unpolarized

Table 3.1: Parameters for the beams used at COMPASS. The muon beam is created from pion decays with a nominal momentum of $172\,\mathrm{GeV}/c$.

a hadron absorber at the end of the decay tunnel the beam is purified. Because the muon beam is a tertiary beam, its momentum spread can be as large as $5\,\%$. Therefore the momentum for each muon is measured by the BMS, located roughly $100\,\mathrm{m}$ upstream of the COMPASS target. The BMS consists of three hodoscopes before and after three consecutive dipole magnets. The high beam intensities require more than two hodoscopes to reduce detection ambiguities.

For calibration and test purposes tertiary electron beams upto $40\,\mathrm{GeV}$ can be produced. The nominal parameters for the beams used at COMPASS can be taken from table 3.1.

3.2 The Detector Setup

Due to the high beam momentum of $190\,\mathrm{GeV}/c$ the final state particles are boosted strongly in forward direction. By using a two stage spectrometer layout, consisting of a large- and small angle magnetic spectrometer (LAS and SAS), COMPASS achieves a very good phase space coverage. Since the first group of detectors are closer to the target and therefore have a smaller lever arm, only particles at larger angles are detected. All absorbing detectors with large radiation lengths, i.e calorimeters, have an opening in the center, letting particles at lower angles pass to the second spectrometer stage located further downstream. Both stages consist of a magnet and a full set of detectors sensitive to different types of particles (see figure 3.6). Details will be described in the sections below. The complete overview of the 2008 setup of the COMPASS experiment is shown in figure 3.3, since the data from this period are analysed in this thesis [17, 14] .

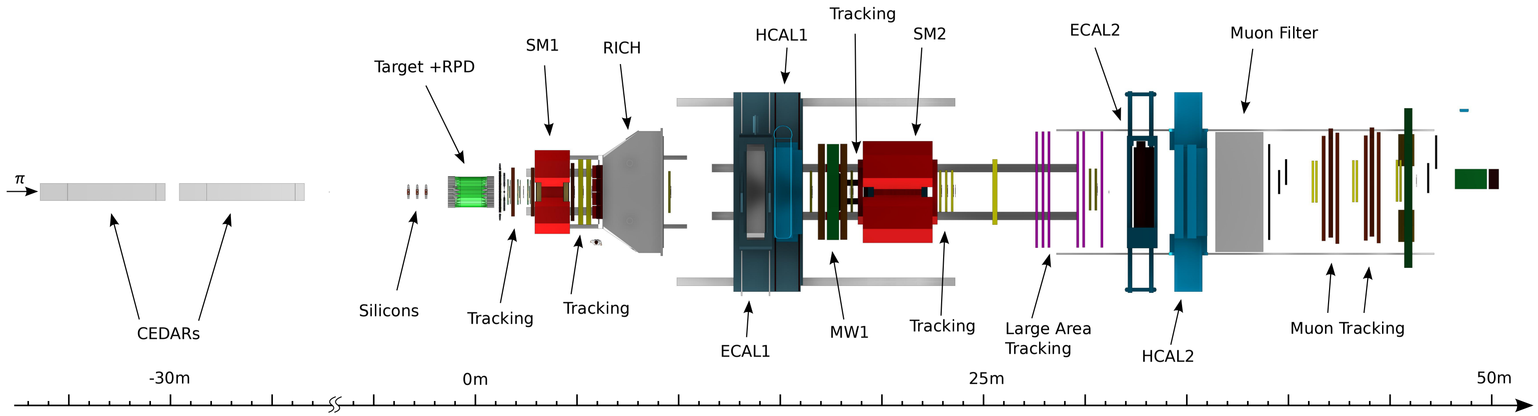

Figure 3.3: Top view of the COMPASS spectrometer for measurements with hadron beams, performed in 2008. The length scale is approximate. Note that not all detectors have been labeled here (courtesy of Prometeusz Jasinski).

3.2.1 Target region

A set of silicon detectors are positioned upstream of the target, which measure the incoming beam inclination with respect to the lab system. The double-sided silicon micro-strip detectors provide a position resolution of about 10 μm, and are ideal for measuring small deflections [17]. Because the strip readouts of the n- and p-side of the detector are perpendicular, a single wafer already obtains two-dimensional position information, keeping the material budget at a minimum. The exposure to high luminosities makes these detectors prone to radiation damage. By cooling to 200 K, this degradation is minimized and extends the lifetime of the sensors [18].

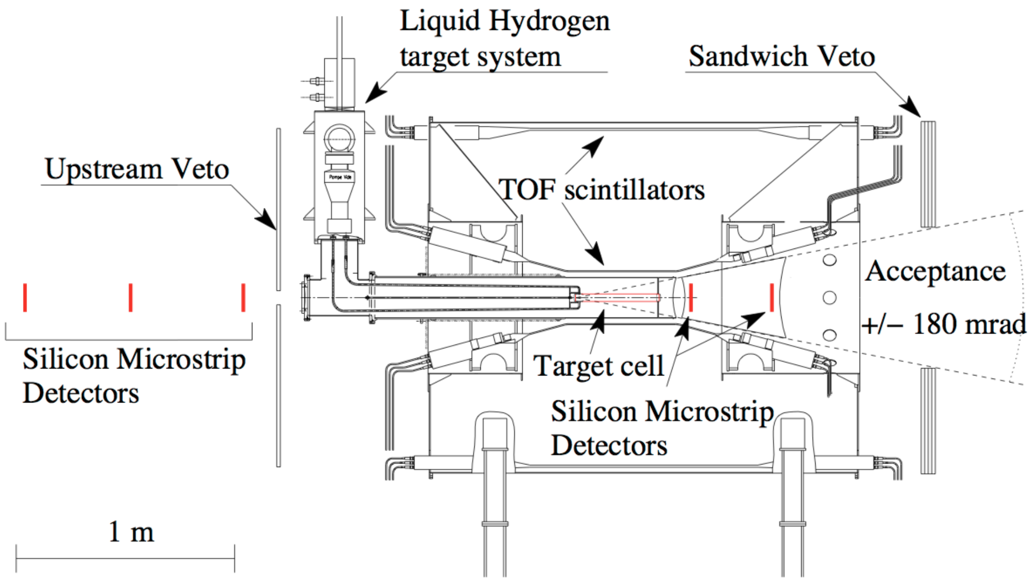

Figure 3.4: Side view of target region of the 2008 setup with the Recoil Proton Detector (RPD) [6]. Note that TOF scintillators make up the RPD.

The target region setup of 2008 is depicted in figure 3.4. Because of the large boost in the forward direction the angle of emittance can be as low as 0.1 mrad, which is equivalent to a spacial separation of about 10 μm, 10 cm away from the production vertex. Therefore another set of silicon detectors, providing the best position resolutions at COMPASS, are positioned immediately after the target, ensuring a good vertex reconstruction. In general, vertices are reconstructed once two or more tracks come close enough to each other, while their point of closest approach represents the vertex. Due to a single charged pion in the $\pi^-\pi^0\pi^0$ final state, the vertex can be reconstructed only by the deflection of the single outgoing track w.r.t. the incoming beam particle. Consequently the vertex resolution is less precise as compared to the $\pi^-\pi^-\pi^+$ final state.

In 2008 a 40 cm long liquid hydrogen target has been used. The dimensions of the target were designed to keep the multiple scatterings of the final-state particles at an acceptable level.

Additional targets for diffractive scattering are thin foils of Pb, W and Ni. The thickness was chosen to have an equivalent interaction length in z direction as the hydrogen target.

For spectroscopy an exclusive[3] measurement is crucial to allow the extraction of the quantum numbers from the kinematic distribution of the final state. For instance as non-exclusive background, also the recoiling proton can be diffractively exited to a Δ resonance. For this reason the target was surrounded by the Recoil Proton Detector (RPD), identifying the recoil protons and providing a fully exclusive measurement.

3.2.2 RPD

The Recoil Proton Detector consists of two rings of scintillator slabs, covering the full azimuthal angle. The inner ring lies at a radius of 120 mm from the beam axis and consists of 12 500 mm long slabs of 5 mm thickness. The outer ring at a radius of 775 mm is built up of 24 scintillators each 10 mm thick and 1080 mm long. A sideview of the detector is shown in figure 3.4, the front view in figure 3.5.

The RPD identifies recoil protons and measures their momentum. Each scintillator slab yields position and time informations for the traversing particle. The resolution of the azimuthal angle and the radial coordinate is given by the spacial dimensions of the scintillator slabs. As the slabs have a two-side readout, the z-position is calculated by the time difference of the two signals. Due to the absence of the magnetic field in the target region the flight path for the particle is straight an is reconstructed from the two space points in the two scintillator barrels. The time-of-flight (TOF) information is used for the calculation of the velocity.

Figure 3.5: Photograph of the target vessel housing the Recoil Proton Detector, which is made of two scintillator barrels.

Energy loss measurements yield the momentum, which, together with the velocity, identifies the traversing particle. The informations of the recoiling protons can be used to reduce the non-exclusive background by checking momentum conservation. However, as the TOF and energy loss measurements are less precise than the position measurements of the RPD, it is uncertain whether the resolution of the magnitude of the momentum is applicable for the momentum conservation check. This aspect is discussed in more detail in chapter 6.

[3] In an exclusive measurement all final-state particles have been identified and their momentum has been determined.

Additionally, because of the used scintillator material, the signals from this detector are fast, and are used for triggering. The RPD trigger fires, once a coincidence of a signal from an element of the inner ring and a signal from one out of three possible scintillator slabs of the outer ring is detected.

The requirement of signals in both barrels, can only be satisfied by protons above a minimum energy, which are able to penetrate the inner scintillator ring and generate a signal in the outer barrel. Therefore proton momenta of below 250 MeV/c are non-existent. This induces a cut in the momentum transfer spectrum of t' =0.05 GeV^2/c^2.

3.2.3 The Spectrometer

This subsection describes the detector setup and layout of the spectrometer, highlighting the parts with specific importance for the $\pi^-\pi^0\pi^0$ final state. The general particle detection scheme is shown in figure 3.6.

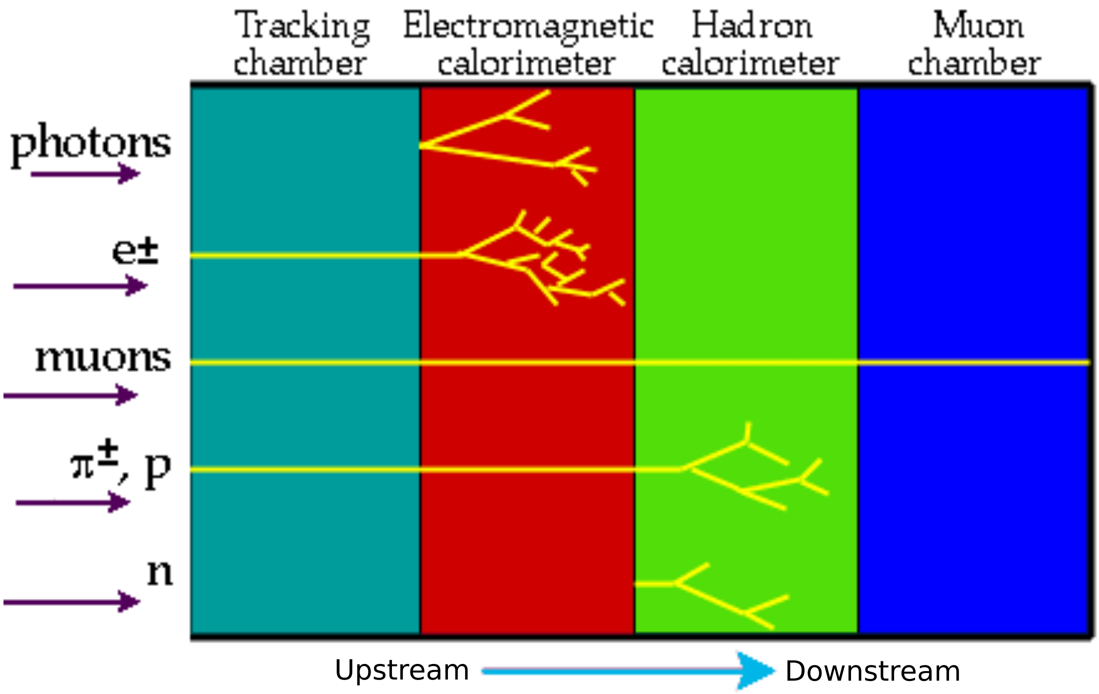

Figure 3.6: The interaction of various particles with different detector types, which illustrates the natural positioning of the detectors [1]

The final state as measured by the spectrometer is defined by the lifetime of the final-state particles. Because the hadronic interaction range is in the order of 1 fm, the $\pi^-\pi^0\pi^0$ system is created on such a scale and the spectrometer only resolves a single decay vertex which coincides with the production vertex. The electromagnetic decay of the neutral pions, ensures the immediate decay into gamma pairs ($c\tau$ = 25 nm).

Only the charged pions, which decay weakly ($c\tau = 7.8\,\mathrm{m}$, do not decay within the spectrometer. Hence the final state is actually $\pi^-4\gamma$ with a single vertex.

After the target the first tracking stage is located, measuring the momentum of the charged particles. The momentum measurement is achieved by tracking the particles before and after a magnet. The curvature of the trajectory in the magnetic filed is directly related to the momentum. A variety[4] of different ionisation and scintillating detectors is responsible for the tracking up- and downstream of the magnet.

Since the first stage of the spectrometer only detects particles at larger angles or lower momenta the first spectrometer magnet (SM1) generates a field integral of only $1.0\,\mathrm{Tm}$, that corresponds to a deflection of $0.3\,\mathrm{rad}$ for particles with a momentum of $1\,\mathrm{GeV}/c$. The deflection of particles at higher energies at this stage is negligible and hence their momentum is determined in the second stage with a more powerful magnet. Downstream of the SM1 the RICH[5] is positioned to identify charged particles. Together with the momentum information, the identification is achieved by the measurement of the emission angle of the Cherenkov radiation, which depends on the velocity of the particle.

Then the first electromagnetic calorimeter (ECAL1) is reached. Photons and electrons will shower here, depositing all of their energy, while the other charged particles will only leave behind partial traces. As the electromagnetic calorimeters are of utter importance for the reconstruction of the $\pi^-\pi^0\pi^0$ final state, they are described in more detail in section 3.2.4. Behind the ECAL1 the first hadronic calorimeter (HCAL1) measures the energy and position of all the hadrons at large angles. Both calorimeters have a center window, letting particles at smaller angles pass to the second stage of the spectrometer. While most of the e, γ and hadrons are stopped completely in the calorimeters, muons penetrate both calorimeters with ease.

Finally the first muon wall (MW1) closes up the first stage. It consists of two stations of tracking detectors with a $60\,\mathrm{cm}$ thick iron wall placed in between, absorbing the remainder of hadrons that have not been completely stopped inside the HCAL1. Once again the muons will not get absorbed in this wall, hence the are identified by leaving a trace in the second detector as well.

The second spectrometer stage measures particles at smaller angles passing through the central holes of the calorimeters and muon wall of the LAS. Charged particles are tracked before and after the $4.4\,\mathrm{Tm}$ strong second spectrometer magnet (SM2). Further downstream the second electromagnetic calorimeter (ECAL2) is positioned in such a way that it covers the region that is illuminated through the window of ECAL1. This detector is decisive for the analysis presented in this thesis, as $85\,\%$ of photons from the π^0 decays are detected by ECAL2. Behind the ECAL2, the second hadronic calorimeter (HCAL2) and another muon wall (MW2) are located, completing the second stage of the spectrometer.

[4] Most tracking detectors are gas ionization detectors, i.e. Micromegas, **G**as **E**lectron **M**ultipliers, drift chambers, multi wire proportional chambers. But also scintillating fibers are used.

[5] **R**ing **I**maging **CH**erenkov detector

The detectors responsible for triggering will be described in section 3.3.

3.2.4 ECAL's

The electromagnetic calorimeters measure the energy and hit position of photons and electrons. For this lead glass (PbO) blocks are used which are on the one hand transparent for low energetic photons and on the other hand are opaque to high energetic photons. Photographs of the different types of calorimeter modules used at COMPASS are shown in figure 3.7.

(a) Photograph of the different modules used in ECAL1 and ECAL2. The top module shows the radiation hard modules of solid lead glass used in the intermediate region of ECAL2. The bottom is the standard lead glass module which can be found in both calorimeters. In the middle the shashlik module can be seen which is exclusively used in the central region of ECAL2 [2].

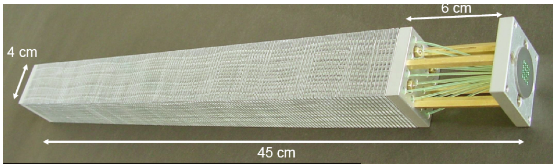

(b) Photograph of the shashlik module. It consists of many alternating layers of steel and scintillation material, while the light of 16 consecutive regions is bundled by optical fibers, which can be seen in the figure. These modules have the best radiation hardness and provide a better signal response.

Figure 3.7

As the high energy gamma ray (or electron) impacts on the calorimeter, it develops an electromagnetic shower in the lead glass. The electrons and positrons from the shower emit Cherenkov light on their way through the glass, because of the high refraction index of PbO. The amount of Cherenkov light is proportional to the energy deposited in each module and is guided to the back of the block which is viewed by a photo multiplier tube (PMT). The PMT converts the emitted light intensity of the module into an amplified electric signal. Note that in general an electromagnetic shower of a single particle spreads over several cells.

The modules shown in figure 3.7a are all of the same granularity. Because ECAL1 is not illuminated as intensely as ECAL2, especially towards the outside, larger blocks were used in these regions. Consequently the resolution of the hit position decreases in these areas. The geometries and the module distribution of the two electromagnetic calorimeters of the 2008 COMPASS setup can be taken from figure 3.8.

For calibration and maintenance, each calorimeter is mounted on a motorized support frame which can be moved by about 2.5 m in the plane orthogonal to the beam. The base calibration for each calorimeter cell is achieved by an electron beam of well defined energy. Due to response changes of the PMTs over time, an additional laser monitoring system is used. The predefined signal of the laser is distributed uniformly by optical fibres to each calorimeter block.

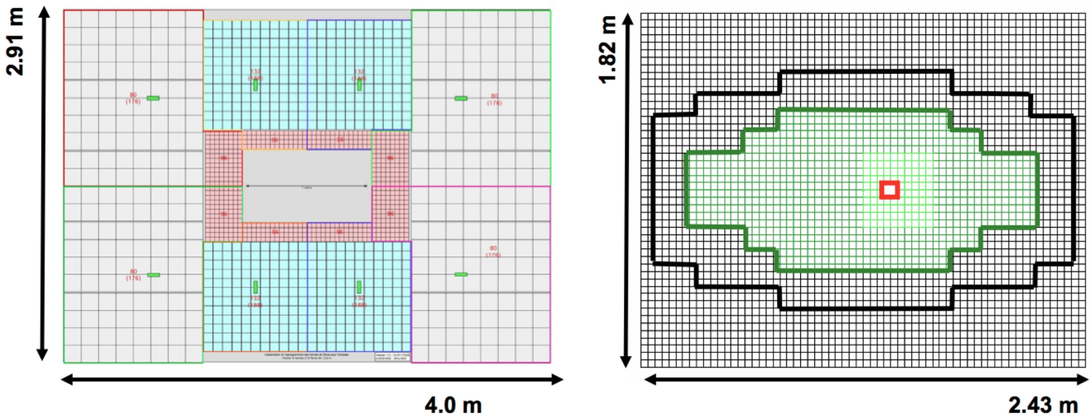

Figure 3.8: Geometrical dimensions of the ECAL1 (left) and ECAL2 (right). ECAL1 uses three different sizes of lead glass blocks, because the intensity decreases with increasing distance from the beam axis. The outer regions on the left and right are filled with 143 mm × 143 mm blocks. On top and bottom of the middle region elements of 75 mm × 75 mm are installed. The central region around the window is equipped with the smallest blocks of 38.2 mm × 38.2 mm dimension. While the regions of the ECAL1 vary in block size, the ECAL2 has constant block sizes but uses more radiation hard blocks closer to the center. The region enclosed by the black line is equipped with radiation hard lead glass blocks. Shaded in green are the shashlik elements that were described in the beginning of this section. On the outside the same 38.2 mm × 38.2 mm cells as in the central region of ECAL1 are used. Enclosed in red is the beam hole with a radius of 20 cm

As already mentioned a single electromagnetic shower creates signals in several neighbouring modules. The signals are fitted by an empirical shower model, which extracts the energy and time informations for the specific cell. Then one obtains a 2 dimensional energy/time distribution which can be fitted by cluster reconstruction algorithm. At this point the overlapping showers can be disentangled. Finally each electromagnetic shower results in a calorimeter cluster with position, energy and time information and their corresponding errors. The time information relative to the other detectors is useful to suppress background (i.e. from noise or pile-up).

Because both gammas and electrons generate showers in the calorimeter it is not obvious which particle hit the calorimeter by merely looking at the shower. However, as electrons carry charge they are tracked upstream of the calorimeter. Hence a reconstructed calorimeter cluster corresponds to a photon if no charged-particle tracks are pointing to it.

3.3 The Data Flow at COMPASS

Triggering is crucial for high luminosity experiments such as COMPASS, since many different reactions occur, however, usually just one specific type is of interest. Moreover the majority of beam particles will not interact and these events have to be rejected. The physics trigger in the 2008 hadron period was the DT0, which consists of a recoil signal in the RPD combined with the signals of the beam trigger and veto detectors.

The beam trigger detector is located upstream of the target and measures beam particle traversing its active area. The beam killer system is part of the veto system and is a coincidence of two scintillating disks, the first in front of the ECAL2 beam hole and the second at the end of experiment. Another part of the veto detector system is the sandwich detector, which vetoes events where a charged particle is outside of the spectrometer acceptance. This can be seen in figure 3.4. Also the upstream veto, which requires particles to pass the target material, is seen in this figure. Scintillating detectors are optimally suited for triggering as small time resolutions is essential.

A small fraction of triggers belongs to non physical triggers that are useful for detector studies etc.

Good events, as defined by the trigger, are digitized by the detector front ends and assembled by event building computers which bundle the data of all detectors. The reconstruction from raw detector signals to a physical event is performed by the CORAL[6] software, which first converts the signals to spacial coordinates, energies, times, etc. Then charged particle tracks, vertices, and calorimeter clusters are reconstructed. Finally this information will be stored mDST[7] files, which are then used for physics analysis.

The Physics Analysis Software Tool (PHAST) is the interface to the reconstructed events, which are available to the analyst, containing information such as particles, tracks, calorimeter clusters, vertices, etc. Each event is processed by PHAST and exclusive events with the appropriate signature are selected. This procedure is described in more detail in chapter 4.

Last but not least the acceptance of the experiment can be corrected for by MC simulations. Here events are generated and propagated through the detector setup by COMGEANT, creating showers in the detectors. Afterwards CORAL simulates the respective detector signals. Then the identical reconstruction chain to the real data, CORAL in combination with PHAST, is used. The crucial difference with respect to the real data is that here the true values (MC truth) are simultaneously passed through the reconstruction chain, which allows to calculate the acceptance corrections.

[6] **CO**MPASS **R**econstruction and **A**na**L**ysis

[7] **m**icro **D**ata **S**ummary **T**ree

Chapter 4

The Basic Event Selection

In this chapter the basic event selection for the $\pi^-\pi^0\pi^0$ channel is presented, and is used for the crosscheck of the two partial wave analysis frameworks ROOTPWA and COMPASSPWA. Since this channel has already been analyzed using the ladder framework, the idea is to use this as a reference [25]. In order to eliminate the possibility of different PWA results caused by different event inputs to the two programs, the event selection presented in this chapter is purely based on the selection criteria of [25].

Nevertheless flaws of this selection will be pointed out throughout this chapter, and possible extensions to this event selections are provided and analysed in chapter 6 in full detail.

This chapter starts with a brief overview explaining the general selection approach for this channel. Furthermore the complete specifications of the data and program versions that have been used are given. Then the actual selection is presented.

4.1 Overview

From section 3.2.3 it was pointed out that the $\pi^-\pi^0\pi^0$ channel is actually registered as $\pi^-4\gamma$. However for the partial wave analysis, the Lorentz vectors of the three outgoing pions and the beam pion are mandatory. It is the task of the event selection to gather this information from as many events as possible. In contrast to this, background events that would falsify the PWA results need to be kept at a minimum. Since there is no clear line between signal and noise a compromise has to be reached.

The usual data selection procedure is a two step filtering system. By prefiltering the plain reconstructed data one tries to reduce the amount of data as much as possible without removing events which are needed for the analysis. This results in lower processing times when readjusting cuts afterwards, studying the channel beyond the standard event selection or even combining multiple channels in a single preselection. This preselection was specifically designed to incorporate extensions, which are presented in chapter 6.

In the second stage all further filters are applied, selecting the events with the specific conditions that is searched for. Kinematic constraints such as 4 momentum conservation at the production/decay vertex are applied to reduce the signal to noise ratio of the final selected events. From now on this common vertex will also be referred to as the primary vertex [1]

Before going into the selection details, the specifications of the raw data and versions of used software pieces will be stated. All data used in this thesis are from the period (W37) of 2008 with the second iteration of data reconstruction code (slot2). Since software frameworks continuously evolve, the specific software versions that were used to reproduce the result of [25] are displayed in Table 4.1.

year of data taking	2008
fraction of data used	10 %
data production type	slot2
PHAST version	7.104
RPD Helper svn revision	147
system information	lxplus 4 (32 bit)

Table 4.1: All relevant informations and specifications of the data used in this analysis

4.2 The Event Preselection

An overview of the preselection cuts that will be described in this section is shown in table 4.2. Apart from the inclusion of events containing higher gamma counts, the

[1] A vertex that was reconstructed by a beam particle is known as a primary vertex and therefore equivalent to the production vertex.

preselection was designed to cut on variables that are discrete, such as trigger, number of primary vertices, etc.

Applied cut	# of events (this)	# of events (as in [25])	Remainder
all events	$6.98800 \cdot 10^8$	$6.98800 \cdot 10^8$	100 %
DT0 trigger	$5.07415 \cdot 10^8$	$5.07415 \cdot 10^8$	72.6 %
1 primary vertex	$4.02453 \cdot 10^8$	$4.02453 \cdot 10^8$	57.6 %
1 outgoing track	$2.25624 \cdot 10^8$	$2.25624 \cdot 10^8$	32.3 %
$-100\,\mathrm{cm} < \mathrm{pv}_z < 0\,\mathrm{cm}$	$2.10176 \cdot 10^8$	NA	30.1 %
chargesum cut	$2.04313 \cdot 10^8$	NA	29.2 %
$4 \leq$ # neutral clusters	$4.99793 \cdot 10^7$	NA	7.2 %

Table 4.2: Summary of event preselection.

DTO Cut:

The first applied cut selects the primary trigger of the period, the DT0 trigger, which cuts on events carrying potential relevant physical information. As mentioned in chapter 3, this trigger constrains the proton momentum to larger than $250\,\mathrm{MeV}/c$ and momentum transfer to $0.07\,\mathrm{GeV}^2/c^2$ and above.

Primary Vertex + 1 Outgoing Track:

As explained in 3.2.3 the final state of interest is $\pi^- 4\gamma$ with a single common vertex. Therefore only events with exactly one primary vertex are selected. Up to now all channels are included in the data but ultimately only the $\pi^-\pi^0\pi^0$ channel is of interest. Hence a selection to exactly one outgoing track, which corresponds to a charged particle, was performed.

Crude Target Cut:

The primary vertex z position distribution can be seen in figure 4.1, which already gives first insights to physics. Of cause the target, located at around -70 cm to -30 cm, should give the biggest amount of production vertices. Additionally before and after the target region different peaks are visible. The peaks at -11 cm and 23 cm correspond to the two silicon detectors. The remaining peaks arise from the support structure, containing the liquid hydrogen target. In the preselection, only a crude cut on the target region was performed. Here the z position of the primary vertex was chosen to be within $-100\,\mathrm{cm} < z < 0\,\mathrm{cm}$, while the radial position was left unconstrained.

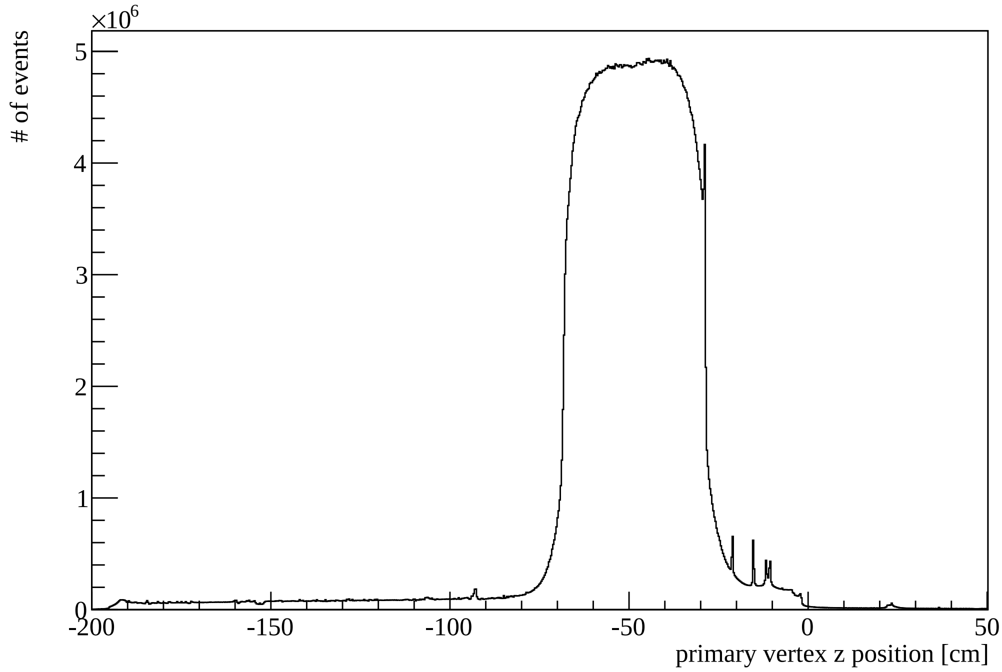

Figure 4.1: The z distribution of the reconstructed primary vertices before any cuts have been applied. The liquid hydrogen target ranges from about -70 cm to -30 cm.

Charge Conservation Cut:

Furthermore the charge conservation at the primary vertex can be tested. Since the incoming beam pions are negatively charged, the outgoing charged particle has to carry negatively charge as well. By looking at table 4.2, most of the selected events a reconstructed correctly in terms of charge conservation.

γ Count Cut:

Further improvement concerning the size of the data sample can be achieved by selecting only events with four or more neutral electro-magnetic calorimeter clusters (see 3.2.4). From now on the expressions neutral clusters and gamma are treated as equivalent. At this point the additional channels $\pi^-5\gamma, \pi^-6\gamma\cdots$ are also included in the selection. In case of one or more additional neutral clusters being present in events, the $\pi^-4\gamma$ event is pushed into the channels mentioned above. Additional statistics can be gained by recovering $\pi^-4\gamma$ final states from these events. This is one of the extensions of the basic selection and will be presented in chapter 6.

After having applied all these cuts only 7.2 % of the data remains.

4.3 The Basic Final Event Selection

The duty of fully extracting the reaction of interest and verifying the kinematics still remains and is worked out here. An overview of all the final selection cuts can be seen in Table 4.3. As already mentioned, this part of the selection is completely identical to [25].

Applied cut	# of events (this)	# of events (as in [25])
All preselected events	$4.99793 \cdot 10^7$	NA
real target cut	$4.17754 \cdot 10^7$	NA
$N_\gamma = 4$	$9.757433 \cdot 10^6$	$9.75743 \cdot 10^6$
$\lvert M_{\pi^0} - 134.98\,\mathrm{MeV}/c^2\rvert < 20\,\mathrm{MeV}/c^2$	$9.15084 \cdot 10^5$	$9.15084 \cdot 10^5$
multiplicity = 1	$8.99705 \cdot 10^5$	$8.99705 \cdot 10^5$
$E_{\pi^-} < 185.00\,\mathrm{GeV}$	$8.20096 \cdot 10^5$	$8.20096 \cdot 10^5$
$N_{\mathrm{proton}} = 1\,\&\,\lvert p_{\mathrm{proton}}\rvert > 250\,\mathrm{MeV}/c$	$5.85308 \cdot 10^5$	$5.85308 \cdot 10^5$
$\lvert\Delta\phi\rvert < 0.20\,\mathrm{rad}$	$3.95250 \cdot 10^5$	$3.95250 \cdot 10^5$
$\lvert M_{\pi^0} - 135.00\,\mathrm{MeV}/c^2\rvert < 16\,\mathrm{MeV}/c^2$	$3.25001 \cdot 10^5$	$3.25001 \cdot 10^5$
$\lvert E_{\mathrm{beam}} - 190.50\,\mathrm{GeV}\rvert < 6.00\,\mathrm{GeV}$	$2.41196 \cdot 10^5$	$2.41406 \cdot 10^5$
kaon veto: majority ≥ 6	$2.37972 \cdot 10^5$	$2.39511 \cdot 10^5$
$0.10\,(\mathrm{GeV}/c)^2 < t' < 1.00\,(\mathrm{GeV}/c)^2$	$1.93636 \cdot 10^5$	NA

Table 4.3: Summary of the final event selection. Note that the number of gamma cut ($N_\gamma = 4$) includes energy scaling and thresholding for the individual calorimeters

Target Cut:

To ensure that the intermediate state X was created inside the target, a cut on the primary vertex position was made. The z position was required to lie within $-68.4\,\mathrm{cm} < z < -28.4\,\mathrm{cm}$, and the x-y positions where selected according to $\sqrt{x^2 + y^2} < 1.75\,\mathrm{cm}$.

In figure 4.2a the x-y primary vertex positions are shown. First of all it is reassuring for the vertexing to see the impression of the containment vessel of the liquid target which lies close to the black circle that illustrates the applied cut. Actually the bottom right of the circle cuts into the containment vessel, so the radius of the circle should be reduced. Furthermore the exact structure of the beam, which is a little bit deformed from a circle at the bottom right, can be extracted. Also the fill level of the liquid hydrogen in the containment can nicely be seen.

The z-position distribution is depicted in figure 4.2b. The filled yellow region represents the cut that has been made. The number of events increasing from the beginning to the end of the target seems counter intuitive at first, but can be explained by multiple scattering of the outgoing charged pion. So the probability of rescattering is highest in

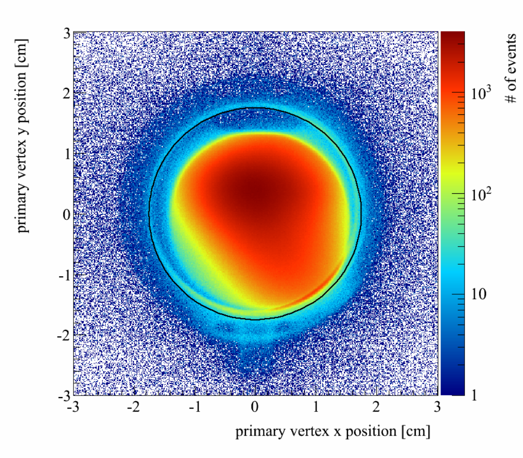

(a) The x-y distribution of the reconstructed primary vertices displayed in log scale. The black circle represents the boundary of the cut that was applied in the selection.

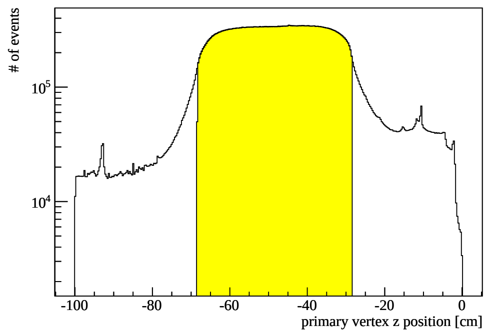

(b) Distribution of z positions of the reconstructed primary vertices. The black curve shows the distribution before the cut, while the region highlighted in yellow are the events afterwards.

Figure 4.2

the beginning of the target, as the particle has to traverse the most remaining liquid hydrogen, and decreases to the end. Once rescattering has taken place, this position is falsely interpreted as the production vertex.

γ Count Cut:

In the preselection the number of neutral calorimeter clusters per event was constraint to four and above, but because only the channel of exactly 4γ's is of interest here, this number is narrowed down to exactly four. But before the actual amount of gammas are selected a simple calorimeter energy scaling has been carried out to ensure the location of the π^0 peak at the value of the PDG[2] mass. Here each neutral cluster was multiplied by the following global energy scales. ECAL1: $m_{\pi^0}^{\mathrm{PDG}}/0.1414$; ECAL2: $m_{\pi^0}^{\mathrm{PDG}}/0.1318$. The future data productions will include a π^0 calibration in which each cell of the calorimeter is scaled independently by an iterative procedure.

Additionally to reduce background from calorimeter noise the energy thresholds of 0.250 GeV for ECAL1 and 1.0 GeV for ECAL2 have been applied. As these values just at the hardware thresholds of the calorimeters, higher thresholds optimized for the significance are used in extended selections given in chapter 6. After these corrections, the actual cut on the number of γ per event was applied. The effect of all these restrictions can be seen in figure 4.3. The reason this distribution has entries with 3 photons even though a cut on events above 3γ has been made in the preselection, is

[2]Particle Data Group

due to the applied energy thresholds.

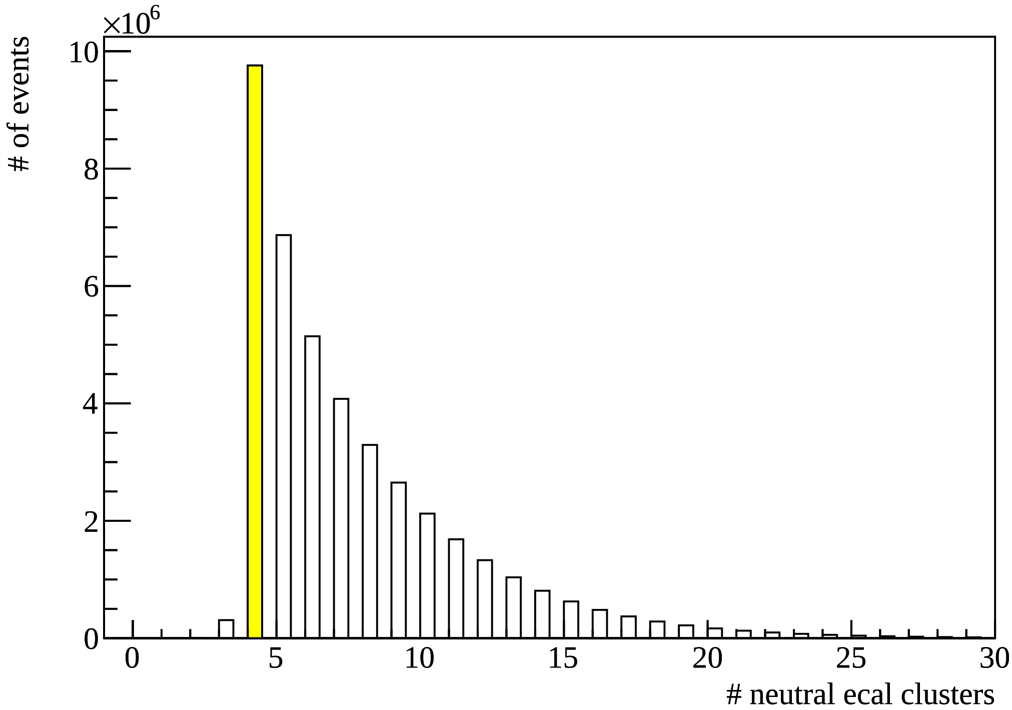

Figure 4.3: Distribution of reconstructed neutral clusters in the electric calorimeters per event. This plot was generated exactly before the cut has been applied, hence the yellow column represents selected 4γ events.

π^0 Mass Cut:

Up to now, only the energy and position of the neutral calorimeter clusters were used in the event selection, while ultimately the Lorentz vectors are of interest. Because photons travel on straight lines, their full reconstruction would be possible if the point of origin is known. Then the γ direction of flight is given by the origin vertex and the cluster position in the calorimeter, while its energy is also known from the calorimeter. Based on the fact that the photon cannot be traced back to its origin by detectors, CORAL cannot automatically reconstruct their Lorentz vectors. In this case the vertex is well defined and the construction of the Lorentz vectors is at hand.

Before moving on, some imported facts about the γ-selection have to be pointed out. In principle a filter is either natural or of "extrinsic" or "intrinsic" nature [20].

Using the $\pi^-\pi^0\pi^0$ decay as an example, the combinatorics is elaborated. Respectively two of the four photons originate from the same π^0 mother state and should therefore be grouped together. Altogether there are 3 possible combinations of grouping the 4γ into 2 $\gamma\gamma$-pairs. This is the intrinsic combinatorial factor. In case events with more than 4 γ's are regarded, an additional extrinsic combinatorial factor arises, by picking 4 γ from the total amount.

Therefore a neutral filter is completely insensitive to any combinatorics. An extrinsic filter is one that is incapable of distinguishing between the internal combinations of the total set of γ's. On the other hand an intrinsic filter is sensitive to these internal combinatorics. It is worth noting that the only intrinsic discrimination which can be made, is by the mass of the γ pairs. This is summarized by the following axiom.

Axiom 1. *All filters that can be applied are neutral or of extrinsic nature, with the exception of filters that constrain the mass of a subset of the total number of photons.*

The invariant mass information of the γ pair is retrieved by addition of the Lorentz vectors of the two photons. Since this channel has two π^0, a two dimensional mass cut is applied here. This 2D mass distribution can be seen in figure 4.4, in which three entries per event are made corresponding to the three combination of combining the 4γ into two $\gamma\gamma$ pairs. On the horizontal axis the mass of the first pair is plotted. Similarly the values of the vertical axis show the mass of the second pair. For the cut, a circular area of $20\,\mathrm{MeV/c^2}$ radius around the paired π^0 PDG mass was cut out of the two dimensional mass plot, which is equivalent to the following formula $\sqrt{(M(\pi_1^0) - M_{\mathrm{PDG}}^{\pi^0})^2 + (M(\pi_2^0) - M_{\mathrm{PDG}}^{\pi^0})^2} < 20\,\mathrm{MeV/c^2}$. Note that all three combinations of an event may survive this cut as long as this mass condition is satisfied for each individual combination. In the low mass region of figure 4.4 an accumulation of events is present which is related to the noise in the electromagnetic calorimeters. Also the two π^0 mass bands are nicely visible validating the existence of this channel.

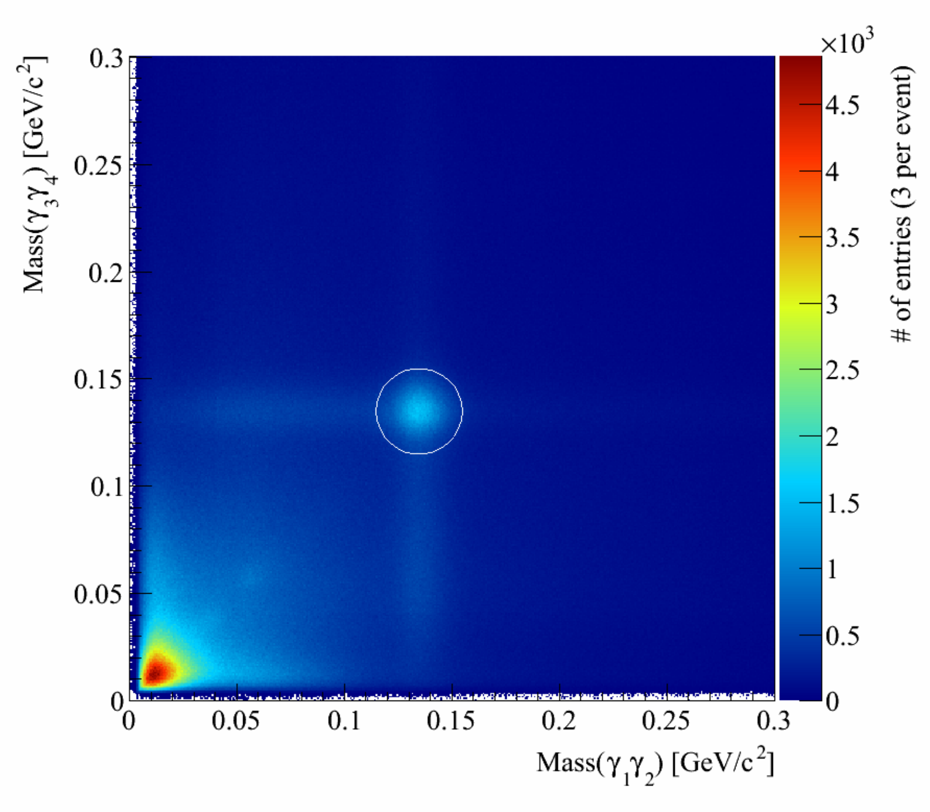

Figure 4.4: 2 π^0 mass plot containing all possible γ combinations (3 entries per event). The 4 reconstructed photons are combined to 2 pairs of two, while the x-axis resembles the mass of the first pair and the y-axis the mass of the second pair. The 4γ's were shuffled in order to produce a symmetric plot. The white circle indicates the cut that has been applied to select the double π^0 events.

Mulitplicity Cut:

Now that a criterium for the choice of the internal combinatorics exists, a multiplicity filter can be applied. In the selection, exactly a single combination per event was required to lie within this $20\,\mathrm{MeV}/c^2$ mass circle.

π^0 Mass Kinematic Fit:

The largest measurement error comes from the neutral cluster reconstruction caused by the resolutions of the calorimeters. This can be seen by the $20\,\mathrm{MeV}/c^2$ width of the π^0 peak, as compared to its actual width in the order of $10\,\mathrm{eV}/c^2$. This justifies the use of a π^0 mass kinematic fitter, which improves the resolution of the other distributions and finally the invariant mass spectrum. This being a χ^2 fit, with the constraint of π^0 mass to the PDG value, the errors the involved variables, that were measured, are required. Unfortunately no such information was available in the data. Because the largest impact on the mass comes from the variation of the photon energies, a simple fit which only adjusts these values was used. The errors were estimated empirically from a calibration beam.

The effect of the fitter on the exclusivity peak can be extracted from figure 4.5. The exclusivity of the event is guaranteed by restricting the energy of the outgoing system, including the kinetic energy of the recoiling proton, to the incoming beam particle energy. Since the ladder was not measured, it is set to the fixed default value of 190 GeV. However in reality the beam energy follows a Gaussian-like distribution around 191 GeV, hence the total energy of the outgoing system should also peak around this value and can be selected as the exclusivity. The beam energy is adjusted [11], using the assumption that the target protons are not excited. In this selection this calculated beam energy was used as the exclusivity.

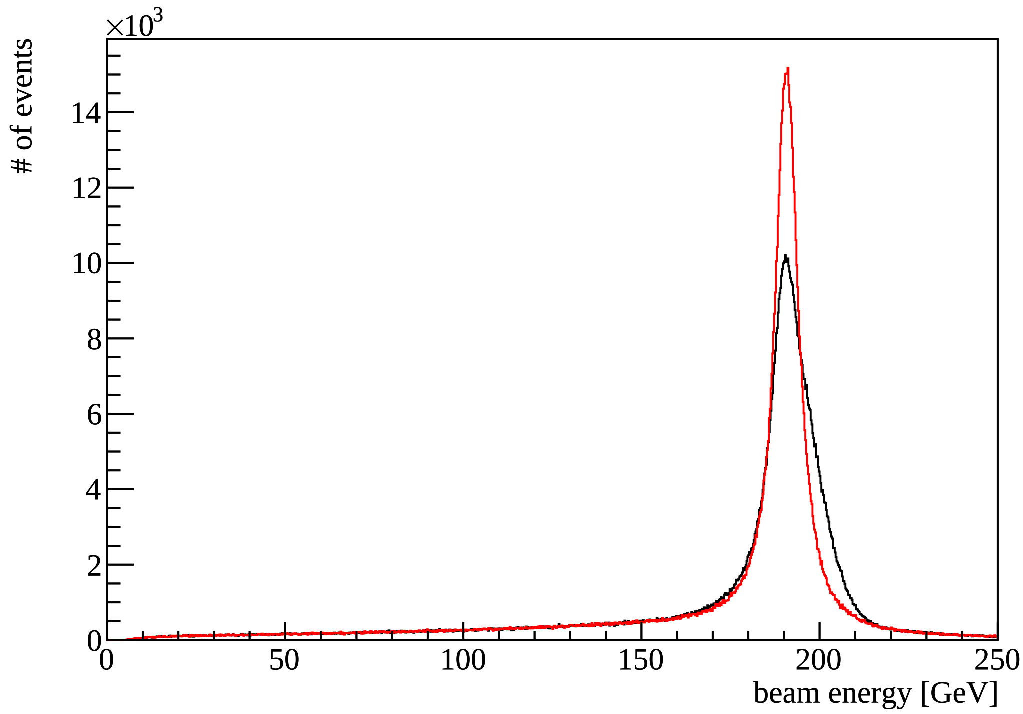

Figure 4.5: Effect of the used kinematic fitter on the exclusivity distribution. In black is the normal exclusivity peak after the multiplicity filter has been applied. The red curve shows the exclusivity peak which had the simple kinematic fitter applied afterwards.

Elastic Scattering Cut:

For the reaction of the beam inside the target many different processes compete, while one is only interested in a single type of reaction. These reactions have different kinematical dependencies, which are measurable quantities. Hence the exclusion of events with the improper kinematic properties are made to suppress the non-exclusive background.

Elastic scattering of the beam pions on the target material is one possible source for such background. The kinematic variable that unveils this, is the energy of the outgoing π^-, since this will not change significantly by the interaction. By looking at the figure 4.6 one can see this elastic scattering band, located at around 190 GeV. The vertical black line at 185 GeV indicates the cut that was made to dispose of these elastic scattering events above this energy of the outgoing charged pion.

This two dimensional plot was chosen to display the correlations with other filters. Naturally elastic scattering events do not have the possibility to generate the two neutral pions, therefore all the photons registered with such events are unphysical and mostly correspond to noise in the ECALs. This is confirmed in figure 4.6 by the accumulation of events in the low $2\pi^0$ energy region of the elastic scattering band. If the mass cut would not have been applied beforehand this accumulation would be drastically higher. This of course counts also visa versa, so most of the noise in the low mass region in figure 4.4 is caused by these elastic scattering events.

Another correlation is the exclusivity itself, which corresponds to the diagonal band in the diagram. As already mentioned these reconstructed π^0's are not related to this reaction, therefore generating entries in the exclusivity distribution which go beyond the nominal energy.

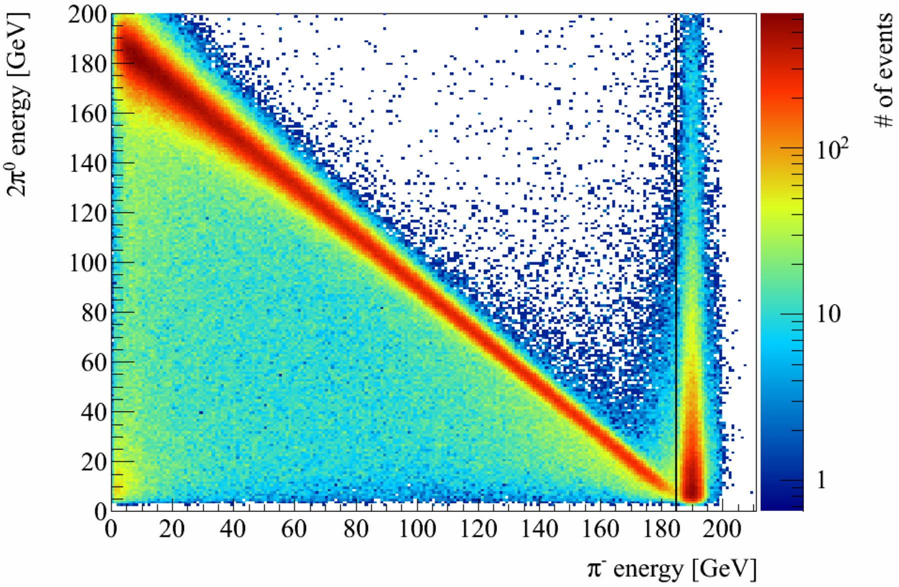

Figure 4.6: Elastic scattering histogram. The vertical band at 190 GeV corresponds to elastic scattered events, while the black line at 185 GeV displays the applied cut.

RPD Cleaning Cut:

Before using the informations of the RPD for momentum conservation checks, they have to be inspected for correct reconstruction. Because the selected events are all triggered by the DT0 which includes a positive signal in the recoil detector, at least one proton track should be reconstructed. However sometimes more than two proton tracks are reconstructed in the RPD or this reconstruction fails. Therefore to avoid additional complexity only events where exactly a single proton was reconstructed are kept. The double ring structure of the RPD limits the sensitivity in the low proton momentum range. This effect is clearly visible in figure 4.7. Below 250 MeV/c the continuous spectrum is interrupted and momenta are appointed to some minimal value of about 200 MeV/c. If the proton reconstruction failed completely their momentum is appointed to 0 MeV/c. Hence it is necessary to apply a cut on the proton momentum of 250 MeV/c and above.

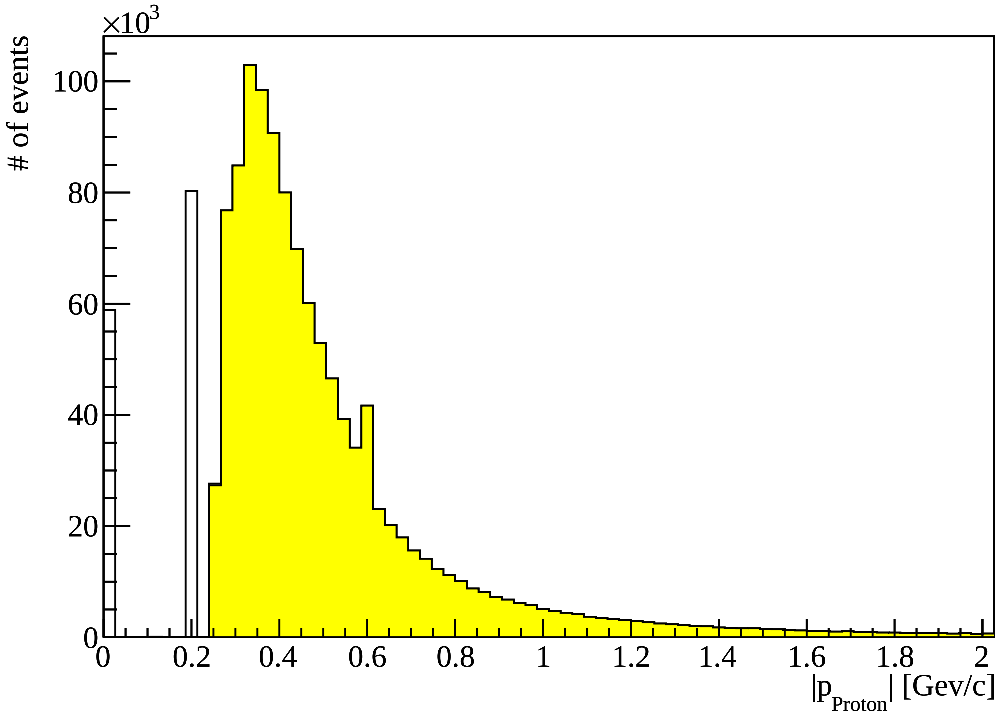

Figure 4.7: Absolute proton momentum distribution of the reconstructed protons from the RPD. Clearly the detector is only sensitive to protons above 250 MeV

$\Delta\phi$ Cut:

Now that recoil proton is reconstructed, the four momentum conservation at the reaction vertex can be checked. Since only three components are independent, the problem is reduced to three momentum conservation. Because the beam momentum is not known, the longitudinal momentum or energy conservation cannot be used. The transverse momenta, with respect to the beam direction, of the outgoing system $\pi^-\pi^0\pi^0$ and the recoil proton should be back to back. This is depicted in figure 4.8.

For the angular component, the difference of polar angles should be 180 °. In the results shown in figure 4.9, a corresponding factor of π was subtracted to center this peak around 0. Events with values of $-0.2\,\mathrm{rad} < \Delta\phi < 0.2\,\mathrm{rad}$ were selected. Note that here, the lab z-direction along the spectrometer was used instead of the beam direction, because the beam inclination w.r.t. the lab system is small. The correct implementation will be used in the extended event selection in chapter 6.

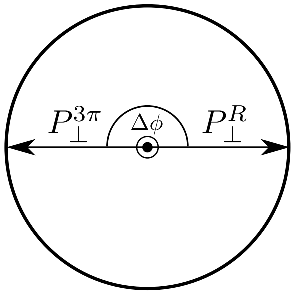

Figure 4.8: Transverse momenta of the outgoing 3π system and the recoil proton. The beam momentum points into the drawing plane.

In contrast to the position resolution, the energy of the proton is only fairly well measured. Therefore it is unclear if the magnitude of the transverse momentum can be checked as well, and was omitted in [25]. A possible implementation and its consequences are also presented in chapter 6.

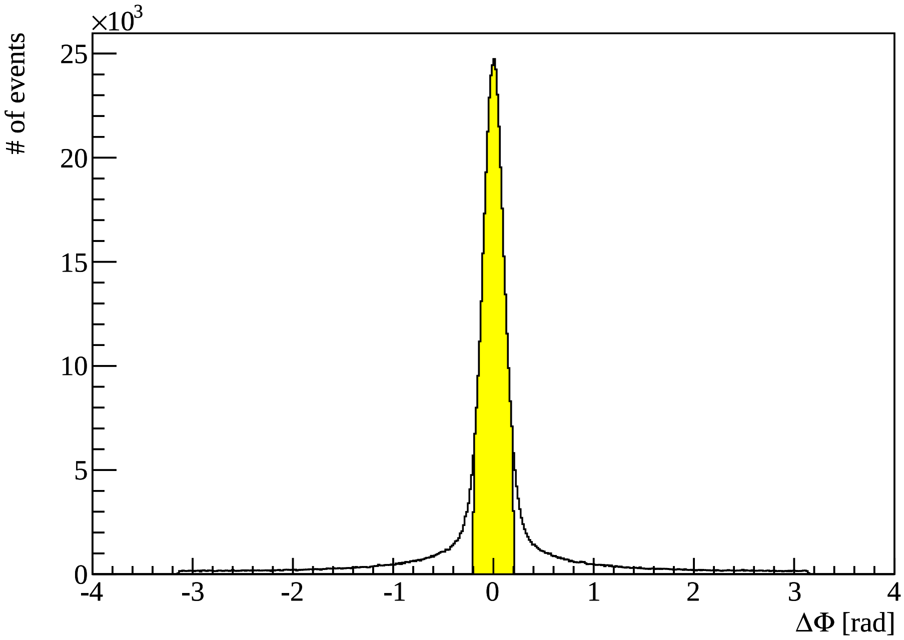

Figure 4.9: The $\Delta\phi$ distribution before the cut itself was applied. Note that a factor of π was subtracted from the $\Delta\phi$ values. The yellow region shows the area that was selected by the filter, which corresponds to $\pm 0.2\,\mathrm{rad}$.

Tighter π^0 Mass Cut:

Before making the cut on exclusive events, the neutral pion masses are selected more stringently. This is possible since the previous mass cut was applied roughly and the mass resolution of the π^0 peak improved slightly after the other filtering stages.

Exclusivity Cut:

Up to now the number of selected events is completely identical to [25], which can be seen from table 4.3. However now the cut on the exclusivity is made, with a calculated beam energy of 190.5 GeV $\pm$ 6.0 GeV. The execution of this cut is depicted in figure 4.10. Since this calculation is dependent on different mass values, the small discrepancy of events is caused by different applications of the formula. In principle from now on the correctness of a filter, compared to [25], is not possible anymore. Nevertheless one should carefully monitor the impact of cuts on this difference.

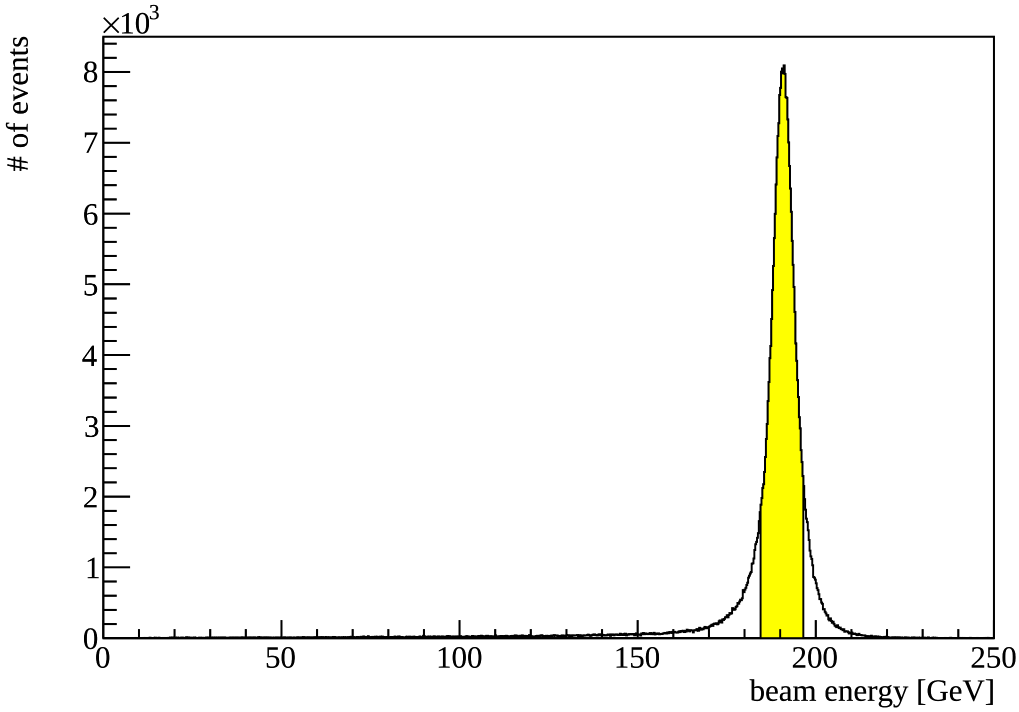

Figure 4.10: The calculated beam energy is plotted, which is also used as the validation of exclusivity for the reaction. Primarily the term exclusivity is used for this distribution. The highlighted region in yellow corresponds to the events that survived this cut.

Kaon Veto Cut:

As mentioned in chapter 3, the beam has a small admixture ($\approx 2\,\%$) of kaons that tamper the selection. Using the informations provided by the CEDAR Helper Class[3] the incoming beam particles are identified. It turns out that here a small discrepancy in the selection is present[4]. Because the effect on the selection is only minor, as seen from table 4.3, this was not re-evaluated.

Momentum Transfer Cut:

The last cut that was applied in the final selection is the four momentum transfer. Because a minimal longitudinal momentum transfer is kinematically mandatory to excite the beam pion into the higher mass state, a momentum transfer distribution balanced for this effect is chosen, $\mathrm{t}' = |\mathrm{t}| - \mathrm{t}_{\mathrm{min}}$. The minimal momentum transfer can be approximated [11] by the following formula.

$$t_{min} = \frac{(m_X^2 - m_{\mathrm{beam}}^2)^2}{4|\vec{p}_{\mathrm{beam}}|^2} \tag{4.1}$$

On the one hand the t' spectrum is cut off at about $0.07\,\mathrm{GeV}^2/c^2$ by the RPD. To avoid the rising edge of this distribution a cut on values below $0.1\,\mathrm{GeV}^2/c^2$ is introduced. This becomes evident from figure 4.11, in which the t' spectrum falls of rapidly below $0.1\,\mathrm{GeV}^2/c^2$.

On the other hand, a constraint limiting the momentum transfer from above had to be set, in order to guarantee the coherent scattering of the pion on the proton. This can be visualized similar to the scattering of electrons on protons. At higher momentum transfers the wavelength of the virtual exchange particle becomes small enough to resolve the substructure of the protons and will interact directly with the quarks and gluons. Therefore an upper bound of $1.0\,\mathrm{GeV}^2/c^2$ was applied. Altogether the momentum transfer is restricted to $0.1\,\mathrm{GeV}^2/\mathrm{c}^2 < \mathrm{t}' < 1.0\,\mathrm{GeV}^2/\mathrm{c}^2$.

[3] The CEDAR Helper Class is an additional software piece to the PHAST framework, which provides PID informations from the CEDAR detector.

[4] In [25] one of the CEDAR majorities to be equal or greater than 6. However there was a mistake in [25], rejecting only events with a majority equal to six.

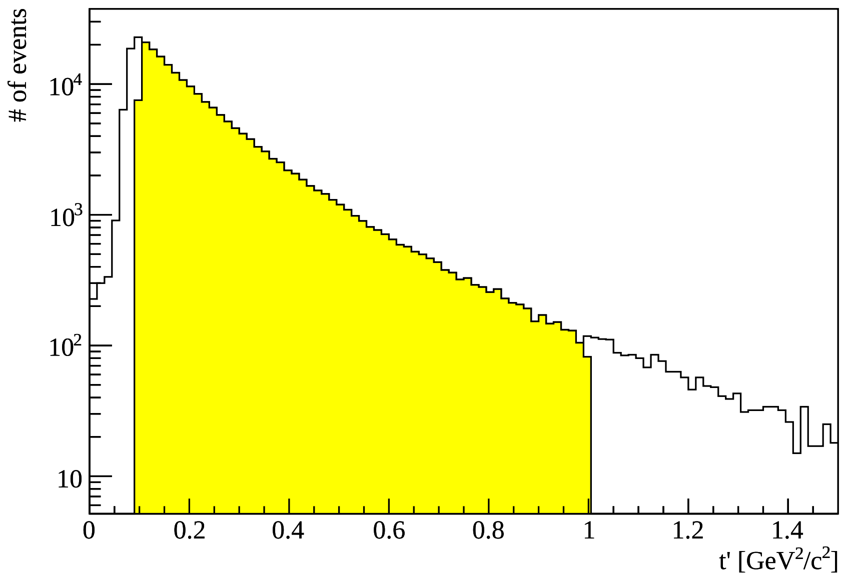

Figure 4.11: The t' spectrum is displayed in log scale to underline the exponential structure. The yellow region once again specifies the cut that was applied.

Final Invariant Masses:

Having completed the event selection the task of exploring and identifying the light meson spectrum, especially exotic states, remains. By looking at the invariant mass spectrum, as seen in figure 4.12, already the major states, the $a_1(1260)$, $a_2(1320)$ and the $\pi_2(1670)$, can be discovered. In principle additional states reside in this spectrum but are not visible to the naked eye because of the overwhelming intensity of the main resonances. In order to disentangle the individual contributions of all states to the total spectrum a partial wave analysis is applied.

In chapter 2 the PWA procedure was explained. From chapter 2 the individual partial waves of the PWA fit model require a complete specification of the decay in form of the quantum numbers of X and the isobar. By looking at the the invariant mass spectra of subsystems of the three pions on can extract possible isobar candidates. Figure 4.13a shows the charged isobar spectrum and reveals the $\rho_3(1690)$, next to the prominent $\rho(770)$ state.

The neutral isobar spectrum is displayed in figure 4.13b, in which three additional isobar states appear. The marked $f_0(600)$ or σ state is very broad and a loose defined resonance that its presence is not directly evident. In addition to this the existence of the $f_0(980)$ as marked in figure 4.13b can only be extracted with some effort from the figure itself. On the other hand the third marked state $f_2(1270)$ can be seen clearly. Exactly the isobars that have been marked in figure 4.13 generate the full isobar decay pattern used in the PWA presented in the next chapter of this thesis.

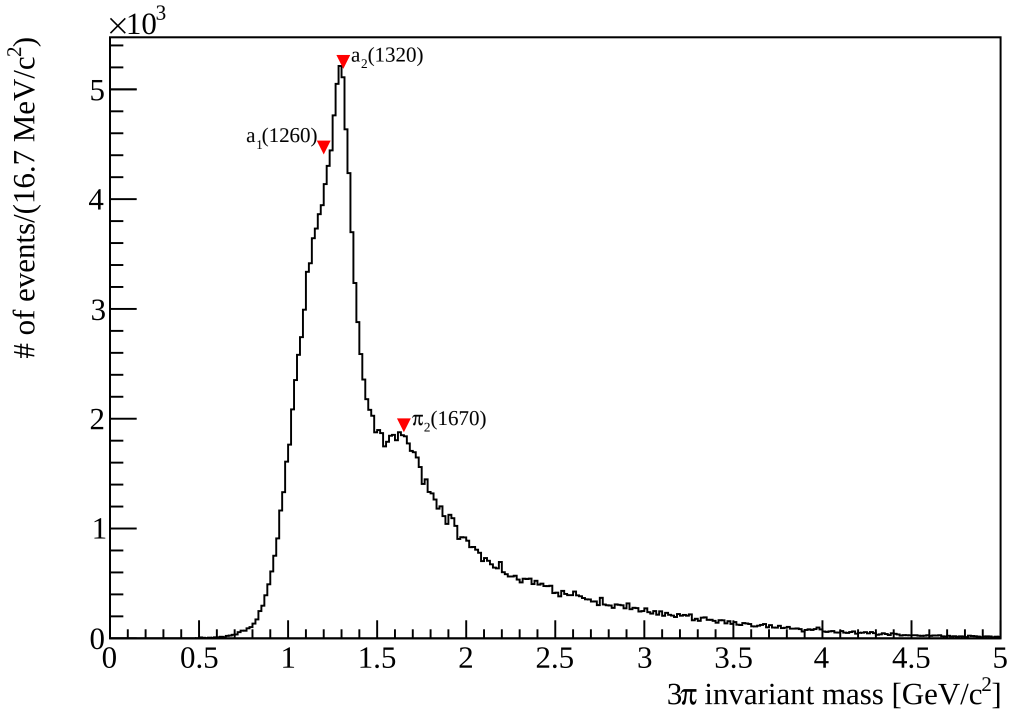

Figure 4.12: invariant mass plot of 3pi system

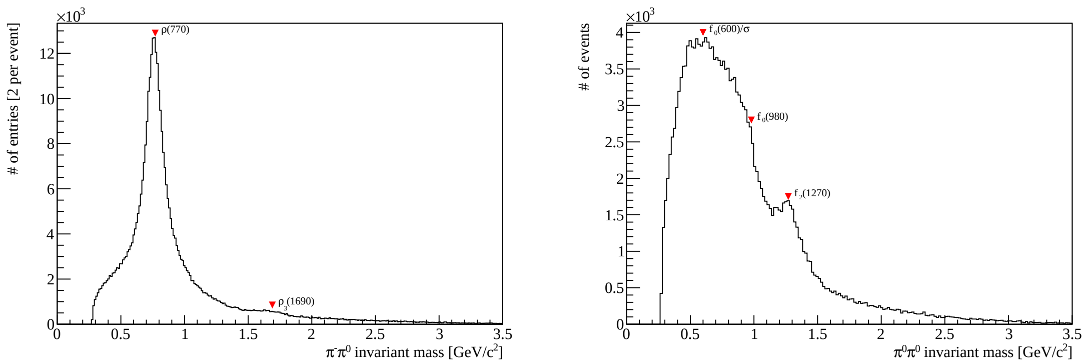

(a) Invariant mass spectrum of the $\pi^-\pi^0$ subsystem. Since two neutral pions are available in the full channel, the histogram has two entries per event.

(b) The invariant mass spectrum of the $\pi^0\pi^0$ subsystem.

Figure 4.13

Chapter 5

RootPWA - CompassPWA crosscheck

This chapter presents the results of the crosscheck of the partial-wave analysis programs rootPWA and compassPWA for the $\pi^-\pi^0\pi^0$ channel. As especially rootPWA has undergone major changes by implementing a new amplitude framework, this crosscheck tests its consistency.

In section 5.1 the course of action for the crosscheck is presented.

The actual results of the crosscheck of the two frameworks are shown in section 5.2, including comparisons of the intensities and phases.

Additionally some weighted Monte Carlo distributions have been created for the rootPWA results, showing the ability of the fit to describe the data. This comparison is shown in section 5.3.

The final conclusions are drawn at the end of the chapter with an outlook for some improvements.

5.1 Overview and Fit Options

In general, fit result differences can occur from the fit options, the model and the minimizer, while the latter two are the interesting quantities that need confirmation. Therefore if the fit options are kept identical, appearing disagreements would be caused by the model or the minimizer. Because an analysis was already performed by Frank Nerling [25] using the compassPWA framework, only a fit with the rootPWA framework had to be carried out with the same fit options.

The fit options, or in other words inputs of the fit, consist of the data set, the wave set, the phase space MC events, used for the calculation of the normalization integrals, and also starting values of the fit parameters for the steepest gradient minimizers. These inputs are discussed in more detail below.

The selection of the events, as presented in chapter 4, resulted in 193 636 selected events. Because a mass-independent fit is performed, the data has to be divided into invariant mass bins. As in [25] the analysis was performed in the mass range from $0.5\,\mathrm{GeV}/c^2$ to $2.5\,\mathrm{GeV}/c^2$, using 50 bins each $40\,\mathrm{MeV}/c^2$ wide. The constraint on the invariant mass range reduces the total number of fitted events to 172 333. For comparison, the number of fitted events in [25] is 173 373. The difference is caused by the 0.6 % disagreement in the event selection of chapter 4.

The used waveset is shown in table 5.1. It consists of 41 partial waves plus an isotropic incoherent "flat" wave that is included to absorb background. Some partial waves were included only for bins above a certain mass threshold. Hence these waves will have zero intensity below their threshold. In principle these thresholds should be removed, because the only physical boundary condition are three on-shell pions with a production threshold of about $400\,\mathrm{MeV}/c^2$, which is below the lower edge of the fitted invariant mass interval. However, for fit-stability reasons they are mandatory.

Both programs use the steepest gradient minimizing approach, which requires starting values for the fit parameters. Unfortunately this method does not guarantee to find the actual global minimum, independent from the used starting point, but merely some minimum which can also be local. The high dimensionality of the parameter manifold, in this case up to 157 dimensional, complicates the fitting procedure. The dependence on the starting parameters can be completely eliminated by using identical ones. However, because this information was not given in [25], the dependence on the start parameter values had to be studied.

To increase the probability of finding the global minimum, as many fits as possible with varying start parameter values should be carried out, while only the one with the maximum likelihood is selected. Already [25] shows the results of the highest log likelihood from a total of 10 fits. Even though the compassPWA framework uses a special minimizer, which was optimized specifically for partial wave fitting, the log likelihood space is poorly probed and it is uncertain, whether the global maximum is found. Therefore the number of fits for the rootPWA program, utilizing the generic minimizer MINUIT2, was increased to 100. For all plots shown in section 5.2, the red graphs represent the best of 600 result of the rootPWA framework, while the black

$J^{PC}M^{\epsilon}$	Isobar	L	S	Bachelor π	Threshold (GeV/c^2)
$0^{-+}0^{+}$	$\rho(770)$	1	1	π^0	-
$0^{-+}0^{+}$	$\sigma/f_0(600)$	0	0	π^-	-
$0^{-+}0^{+}$	$f_0(980)$	0	0	π^-	1.40
$1^{++}0^{+}$	$\rho(770)$	0	1	π^0	-
$1^{++}0^{+}$	$\rho(770)$	2	1	π^0	1.30
$1^{++}1^{+}$	$\rho(770)$	0	1	π^0	-
$1^{++}0^{+}$	$\sigma/f_0(600)$	1	0	π^-	0.86
$1^{++}0^{+}$	$f_2(1270)$	1	2	π^-	1.20
$1^{++}1^{+}$	$\rho(770)$	2	1	π^0	1.40
$1^{++}1^{+}$	$\sigma/f_0(600)$	1	0	π^-	1.40
$1^{++}1^{+}$	$f_2(1270)$	1	2	π^-	1.40
$1^{-+}1^{+}$	$\rho(770)$	1	1	π^0	-
$2^{++}1^{+}$	$\rho(770)$	2	1	π^0	-
$2^{++}1^{+}$	$f_2(1270)$	1	2	π^-	1.50
$2^{-+}0^{+}$	$\rho(770)$	1	1	π^0	0.80
$2^{-+}0^{+}$	$\rho(770)$	3	1	π^0	1.20
$2^{-+}0^{+}$	$\sigma/f_0(600)$	2	0	π^-	0.80
$2^{-+}0^{+}$	$f_2(1270)$	0	2	π^-	1.20
$2^{-+}0^{+}$	$f_2(1270)$	2	2	π^-	1.50
$2^{-+}1^{+}$	$\rho(770)$	1	1	π^0	0.80
$2^{-+}1^{+}$	$\rho(770)$	3	1	π^0	1.20
$2^{-+}1^{+}$	$\sigma/f_0(600)$	2	0	π^-	1.20
$2^{-+}1^{+}$	$f_2(1270)$	0	2	π^-	1.20
$2^{-+}1^{+}$	$f_2(1270)$	2	2	π^-	1.50
$3^{++}0^{+}$	$\rho(770)$	2	1	π^0	1.50
$3^{++}0^{+}$	$\rho_3(1270)$	0	3	π^0	1.50
$3^{++}0^{+}$	$f_2(1270)$	1	2	π^-	1.20
$3^{++}1^{+}$	$\rho(770)$	2	1	π^0	1.50
$3^{++}1^{+}$	$\rho_3(1270)$	0	3	π^0	1.50
$3^{++}1^{+}$	$f_2(1270)$	1	2	π^-	1.20
$4^{-+}0^{+}$	$\rho(770)$	3	1	π^0	1.20
$4^{-+}1^{+}$	$\rho(770)$	3	1	π^0	1.20
$4^{++}1^{+}$	$\rho(770)$	4	1	π^0	1.64
$4^{++}1^{+}$	$f_2(1270)$	3	2	π^-	1.60
$1^{++}1^{-}$	$\rho(770)$	0	1	π^0	-
$1^{-+}0^{-}$	$\rho(770)$	1	1	π^0	-
$1^{-+}1^{-}$	$\rho(770)$	1	1	π^0	-
$2^{++}0^{-}$	$\rho(770)$	2	1	π^0	-
$2^{++}0^{-}$	$f_2(1270)$	1	2	π^-	1.30
$2^{++}1^{-}$	$f_2(1270)$	1	2	π^-	1.30
$2^{-+}1^{-}$	$f_2(1270)$	0	2	π^-	1.20
FLAT	-	-	-	-	

Table 5.1: The used 42 waveset from [25].

graphs show the best of 10 result from [25] that used the compassPWA program.

To get a quantitative estimate for this starting parameter dependence on the fit results, the 600 fits were used to construct an approximate “error” band. For each mass bin the maximum and minimum values of the fits were used to set the limits of the error interval. Of course the distribution of the events in these intervals is not continuous. Thus the start parameter dependence bands serve only to illustrate the magnitude of the variation of the fit results. Appendix A presents a more detailed analysis of this dependency. The cyan shaded areas in the histograms throughout section 5.2 indicate this starting parameter dependence.

In rootPWA, the normalization integrals were calculated using 20 000 MC phase space events. As in [25] no acceptance correction was performed. Of course the comparison of the results is not affected by this, however, the physical results obtained by these fits should be regarded with caution. The svn revision 633 of the rootPWA framework (trunk) has been used to perform the fits in this analysis. An overview of the specifications of the fits is shown in table 5.2.

Number of final selected events	193 636
Invariant mass range	0.5-2.5 GeV/c^2
Number of bins	50
Bin width	40 MeV/c^2
Number of MC phase space events	$2 \cdot 10^4$
Number of fitted events	172 333
Number of waves	42
Fit type	Best of 100
rootPWA svn revision	633(trunk)

Table 5.2: Summary of the rootPWA fit specifications.

5.2 PWA results

Already the 3π invariant mass spectrum after the event selection, as shown in figure 4.12, reveals the most dominantly produced states, the $a_1(1260)$, $a_2(1320)$ and the $\pi_2(1670)$. Therefore as a start, the comparison is made for the strongest waves incorporating these states, which are well defined and established resonances. The overlay of the intensities for the $1^-2^{++}1^+\rho(770)[21]\pi^0$ wave for the two different fits is depicted in figure 5.1.

At a first glance the agreement of the results from the two programs is good. However, a closer look at the difference histogram reveals errors that cannot be explained by the 0.6 % difference of events in the data set. Especially in the region of the $a_2(1320)$ state, the differences are approximately 3 %, aside of the extreme case at 1440 MeV/c^2, which shows a relative error of about 20 %. But the dependence on the starting parameters can account for most of these deviations, as most of the differences lie within or close to the cyan band. As mentioned in section 5.1, the different fit results are not distributed

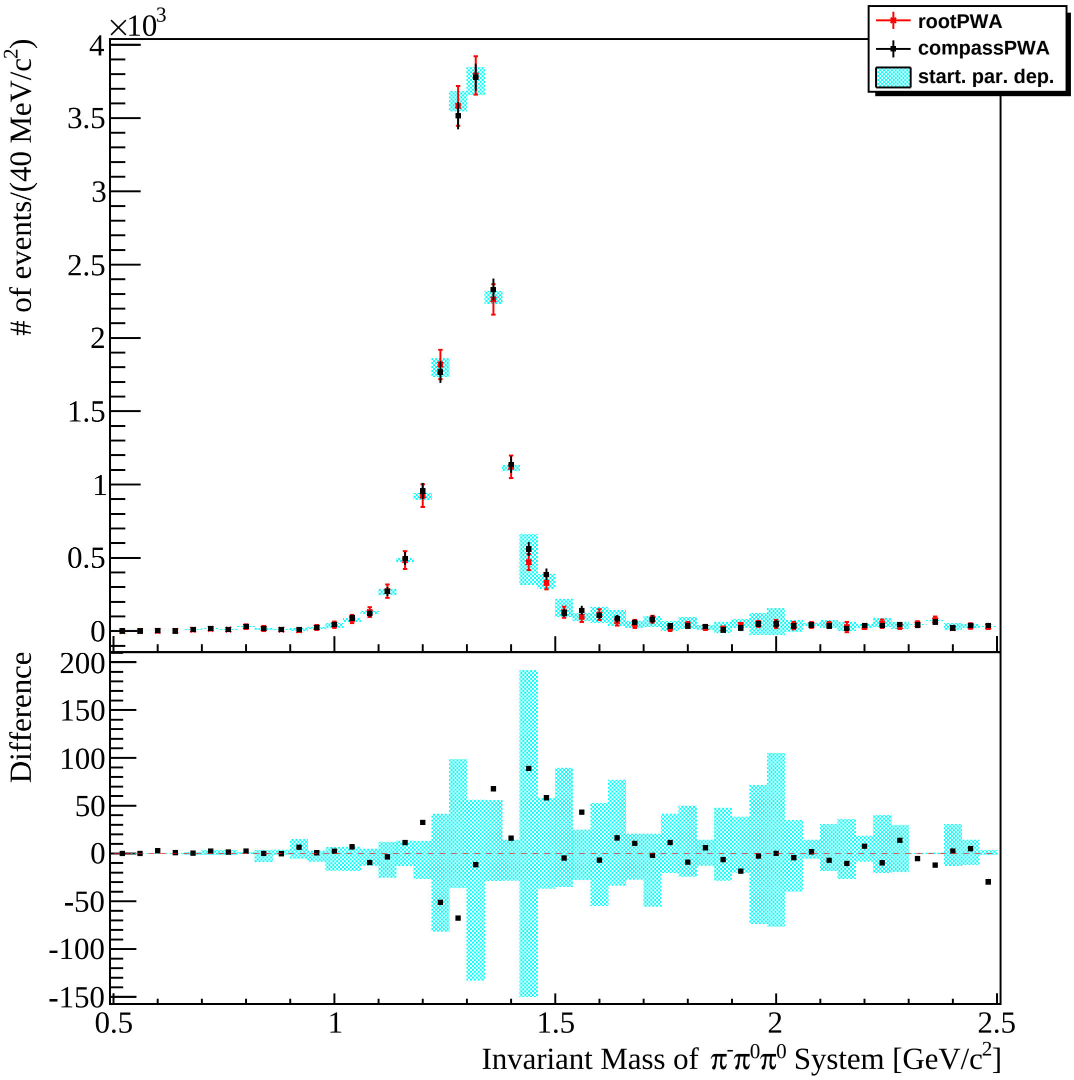

Figure 5.1: Top: Comparison of the extracted $1^{-}2^{++}1^{+}\rho(770)[21]\pi^{0}$ component of the total invariant mass spectrum. The x-axis displays the invariant mass of the $\pi^{-}\pi^{0}\pi^{0}$ system, which was divided into the 50 mass bins of 40 MeV/c^2 width. Each data point originates from a separate fit and was calculated independently of the others. The intensity corresponds to the number of events. The peak at 1.3 GeV/c^2 is the $a_2(1320)$ resonance. The red points show the rootPWA fit result with the highest log likelihood out of 600 separate fits. Similarly the black points show the best of 10 compassPWA results. The cyan band visualizes the start parameter dependence, which is spanned by the highest and lowest fit result out of the 600 rootPWA fit results.
Bottom: Difference of the black graph with respect to the red graph (zero line). Now the fit result differences become apparent and can be compared to the dependence on the starting parameters.

equally within the band, but cluster at certain intensities. Also because only 600 fits were used to span these bands, their magnitude is approximate.

In the low- and high-mass tails of the distribution the relative deviations are in general the highest, due to the low statistics in these mass bins. Still the dependence on the start parameter values can account for the appearing disagreements. Also note that the start parameter dependence is larger in the higher invariant mass range of about $1.3\,\mathrm{GeV}/c^2$ and above. This can be explained by the thresholds of waves, which are left out of the fits for mass bins below, hence the number of fit parameters increases as the invariant mass gets larger. Therefore, a higher dependence in start parameter values is to be expected. Still there are some fit results, for instance at $2360\,\mathrm{MeV}/c^2$, in which the cyan band lies closely around the best fit value of rootPWA and does not expand into the direction of the compassPWA result. In these cases the start parameter dependence cannot account for the difference, but due to the low statistics in these bins, fluctuations play a larger role. Additional reasons for the discrepancy are the minimizer, the fit model and the phase space MC used for the normalization integrals.

Another problem are the systematically larger statistical error bars for the rootPWA results. The cause of this discrepancy is currently under investigation and may either come from larger errors calculated by the fitter or an incorrect error propagation.

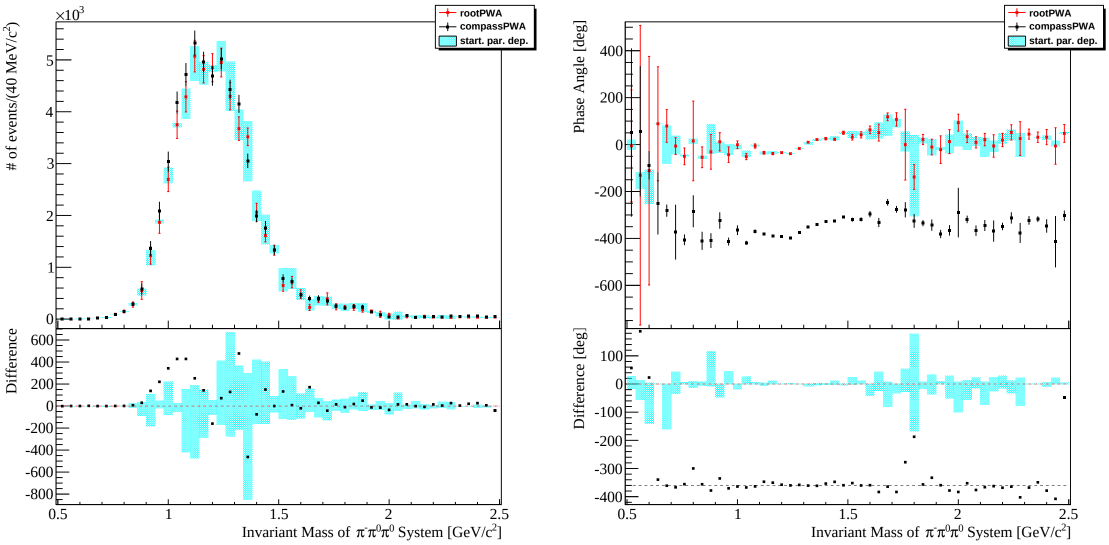

(a) Comparison of the intensity of $1^-1^{++}0^+\rho(770)[01]\pi^0$ wave with the $a_1(1260)$ resonance. Graph analog to figure 5.1

(b) Comparison of the phase between the $1^-1^{++}0^+\rho(770)[01]\pi^0$ and $1^-2^{++}1^+\rho(770)[21]\pi^0$ waves. Graph analog to 5.1.

Figure 5.2

Another intense wave is the $1^-1^{++}0^+\rho(770)[01]\pi^0$, that is depicted in figure 5.2a. Here the $a_1(1260)$ resonance is seen, which is also well defined. Similar observations are made regarding the conformity of the fit results. By comparing figure 5.2a with 5.1

a worsening of the agreement of the two individual fits can be observed. Here several mass bins in the mass region of 1-1.5 GeV/c^2 show relative differences of 10 %, which is approximately a factor of 3 higher than in figure 5.1. By the same statements made above most of these deviations can be explained by the start parameter dependence. Again in some mass bins, for instance 1050 MeV/c^2, the cyan bands indicate quite stable solutions of rootPWA. Hence in these regions the disagreement most likely has another source, but cannot directly be determined at this point.

Besides the intensities, graphs displaying the phase difference between two waves can be compared. In figure 5.2b the phase between the $1^-2^{++}1^+\rho(770)[21]\pi^0$ and $1^-1^{++}0^+\rho(770)[01]\pi^0$ waves of figures 5.2a and 5.1 is shown. The compassPWA results are shifted by -2π, arising from the 2π ambiguity of the polar angle in the complex plane. In this case the difference histogram on the bottom of 5.2b nicely shows that the development for both graphs are similar. Again the start parameter dependence can account for most of the differences between the rootPWA and compassPWA results. Especially for outliers at 1800 MeV/c^2 the dependence on the starting parameters is strong.

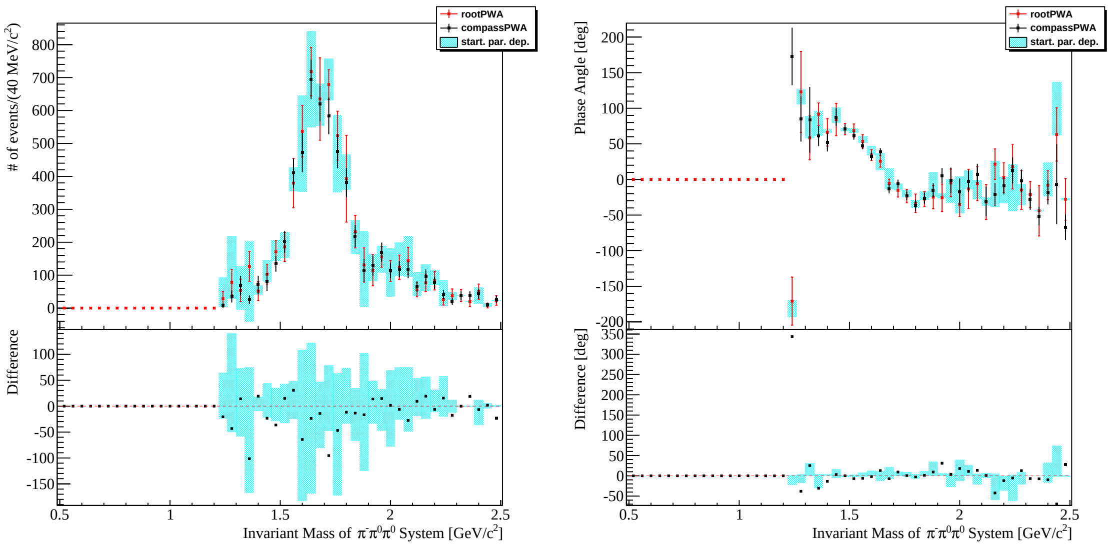

(a) Comparison of the intensity of the $1^-2^{-+}0^+f_2(1270)[02]\pi^-$ wave with the peak of the $\pi_2(1670)$ resonance. Graph analog to figure 5.1

(b) Comparison of the phase between the $1^-2^{-+}0^+f_2(1270)[02]\pi^-$ and $1^-1^{++}0^+\rho(770)[01]\pi^0$ wave. Graph analog to figure 5.1.

Figure 5.3

Apart from the $a_1(1260)$ and $a_2(1320)$, the overall invariant mass spectrum exhibits a third structure due to the $\pi_2(1670)$. One of the waves that has the quantum numbers of the π_2 is $1^-2^{-+}0^+f_2(1270)[02]\pi^-$, which is shown in figure 5.3a. The wave has a threshold at 1.2 GeV/c^2, so that the intensity is zero below this mass.

Figure 5.3b displays the phase between this wave and the $1^-1^{++}0^+\rho(770)[01]\pi^0$ wave, containing the $a_1(1260)$ resonance. A clear phase motion at the π_2 mass can be observed. For both the intensity and phase histogram in figure 5.3, most of the fit result disagreement can be explained by the dependence on the start parameters.

So far only well defined states have been used for the comparison, but the main purpose of studying this channel, is to find resonant structures in spin-exotic waves. Figure 5.4a shows the highest intensity wave with exotic quantum numbers. Despite a few outliers, the fit results of both programs are consistent within the start parameter dependence bands. Also the systematically larger statistical error bars in rootPWA can nicely be observed.

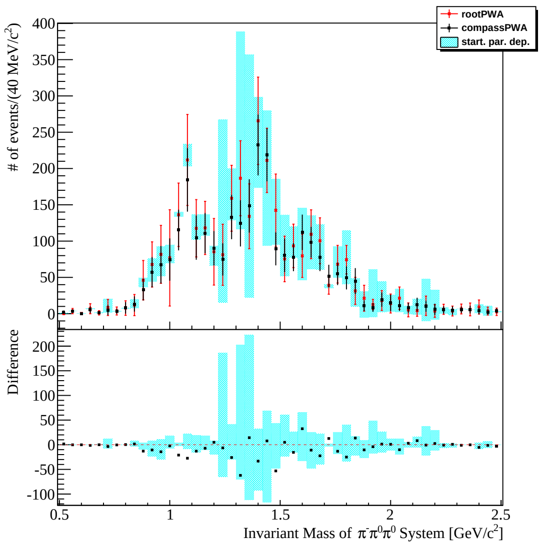

(a) Comparison of the intensity of the spin-exotic $1^-1^{-+}1^+\rho(770)[11]\pi^0$ wave. Graph analog to figure 5.1

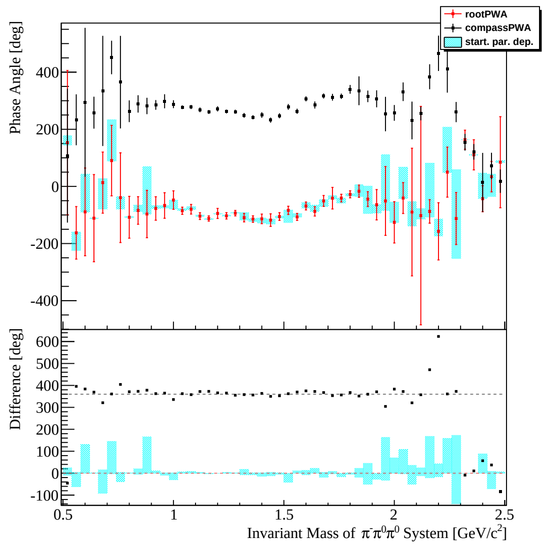

(b) Comparison of the phase between the $1^-1^{-+}1^+\rho(770)[11]\pi^0$ and the $1^-1^{++}0^+\rho(770)[01]\pi^0$ wave. Graph analog to figure 5.1.

Figure 5.4

Looking at figure 5.4b, a shift of 2π in the phase between the $1^-1^{-+}1^+\rho(770)[11]\pi^0$ and $1^-1^{++}0^+\rho(770)[01]\pi^0$ wave is again revealed. Nevertheless both fit results agree well within the 2π ambiguity, especially in the more well-defined region of the $a_1(1260)$ resonance. In particular points that show large variations, for instance at $2160\,\mathrm{MeV}/c^2$, also exhibit strong dependencies in the start parameters.

Last but not least the flat waves can be compared, which is shown in figure 5.5. Apart from some missing values in compassPWA result[1], both distributions are exactly zero, which is suspicious since a phase-space-like background is expected. For comparison

[1] Due to a data format conversion problem, some values of zero were assigned to artificial values in the order of 10^6 .

the flat wave of the charged channel ($\pi^-\pi^-\pi^+$) is depicted in figure 6.14c. The origin of this effect is currently being studied and may arise due to overfitting. So more studies concerning the fit model are required.

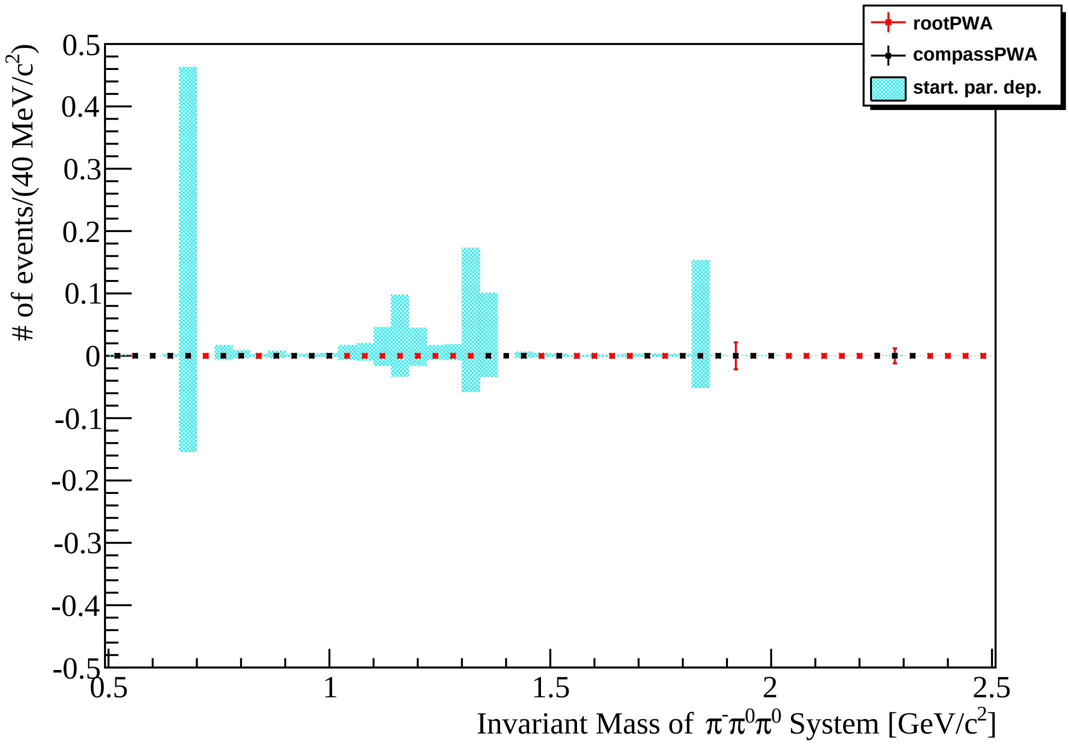

Figure 5.5: Comparison of the intensity of the flat wave.

5.3 Weighted Monte Carlo

So far it is still unknown how well the fitted model is actually able to describe the measured distribution, as the fitter only tries to find the best possible parameter set. The goodness of the fits is estimated by the weighted Monte Carlo (MC) method.

The phase space events, which have already been used to calculate the normalization integrals of the decay amplitudes, are weighted by the amplitudes calculated from the fit results. Because each mass bin was fitted separately, the comparison between the real data and the weighted MC is done bin-by-bin. Note that the fit results used to perform the weighted MC originate from the best fit which was used for comparison in the section above. Since no acceptance correction is applied, the kinematic distributions remain distorted by apparatus effects. This may generate artefacts in the fit, as it is trying to match the model to the distorted data. Depending on the number of fit parameters, the consequences can be artificial intensities and overall worse fit results.

Therefore the comparison shown here, has to be regarded with care. Nevertheless the success of the current fit can be checked localizing problematic areas.

Comparisons for all kinematic distributions of the data and the weighted MC are possible, but since the five phase space variables $\tau = \{\theta_{GJ}, \phi_{GJ}, m_I, \theta_H, \phi_H\}$ already contain the full information, their comparison is sufficient. Because the weighted MC histograms usually contain more statistics than the data, the former are normalized to the number of real data events in the mass bin, in order to make a direct comparison.

Due to the overwhelming number of plots, only a selected sub-sample will be displayed, that summarize the fit results. At first the angles of the GJ-frame are compared. Figure 5.6 shows $\cos(\theta_{\mathrm{GJ}})$ distributions for both the charged and neutral isobar decay pattern for a selected mass bin featuring the largest deviations.

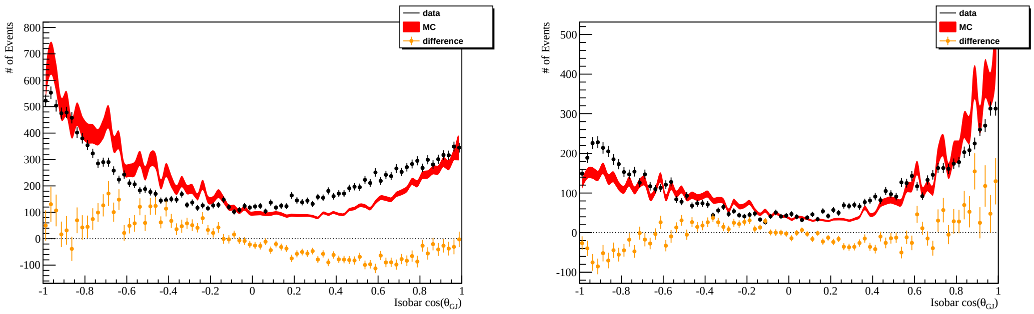

(a) **(b)**

Figure 5.6: $\cos(\theta_{GJ})$ distributions for the 3π mass bin $[1140, 1180]\mathrm{MeV}/c^2$. (a): Charged isobar decay topology. (b): Neutral isobar decay topology.

Obviously the fitter has difficulties matching the model to the data for the charged as well as the neutral isobar part. In particular, by looking at figure 5.6b one notices a rapid decrease of the data in the region of $\cos(\theta_{\mathrm{GJ}}) = -1$. Apparently the model is not capable of describing the measured distribution and the fit is forced to an average description causing the oscillation in the differences. As a matter of fact, it is known from acceptance corrections of other channels, that the acceptance in the $\cos(\theta_{\mathrm{GJ}})$ distribution drops towards the edges. Hence, similar acceptance dips are to be expected in the neutral channel. On the other hand, in the case the acceptance effects are negligible, missing waves in the model are responsible for the bad description of the data. Similar observations can be made for the charged isobar case depicted in figure 5.6a.

By displaying the differences between the weighted MC and the data versus the total invariant mass, a summary over the whole mass bin range can be given. These plots are extremely useful to spot basic fitting problems from the continuous developments of the differences. The mass overview plot for $\cos(\theta_{\mathrm{GJ}})$ is shown in figure 5.7.

If the fit model is able to describe the data, one would expect random distributions of differences around zero. Instead one notices regions of under- or overestimation, high-

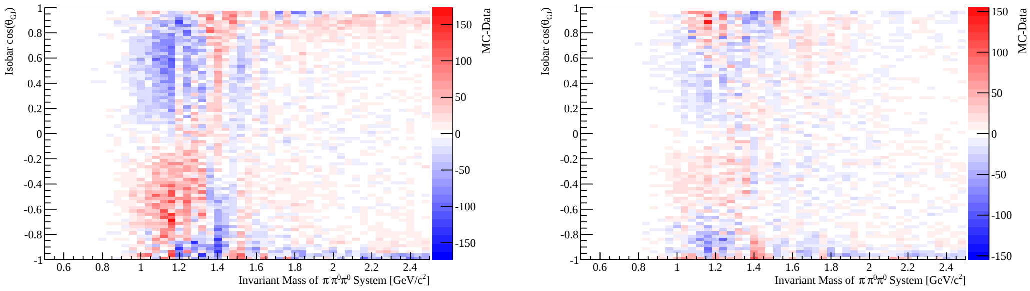

(a) **(b)**

Figure 5.7: $\cos(\theta_{\mathrm{GJ}})$ differences as a function of the 3π mass. (a): Charged isobar decay topology. (b): Neutral isobar decay topology.

lighting the problematic areas. At first sight, the disagreement in the $a_1(1260)/a_2(1320)$ region is particularly striking. However as these bins contain the largest amount of data, the absolute errors are expected to be larger. In order to make quantitative statements, the one-dimensional projections for the individual bins have to be regarded (see figure 5.6). The fit model has difficulties describing the data for nearly all mass bins in the regions of $\cos(\theta_{\mathrm{GJ}}) = \pm 1$, again suggesting to be a missing acceptance effect.

By looking at figure 5.7a one can see solutions of the fitter at an invariant mass of about $1.4\,\mathrm{GeV}/c^2$, which possess opposite discrepancies to the neighbouring mass bins. This jumping in solutions fortifies the statement, that the fitter is incapable to match the data.

Going to higher mass bins the discrepancies at $\cos(\theta_{\mathrm{GJ}}) = \pm 1$ can be observed in more detail. To illustrate this, figure 5.8 shows the $\cos(\theta_{\mathrm{GJ}})$ distribution for the invariant mass bin of $[1780, 1820]\mathrm{MeV}/c^2$.

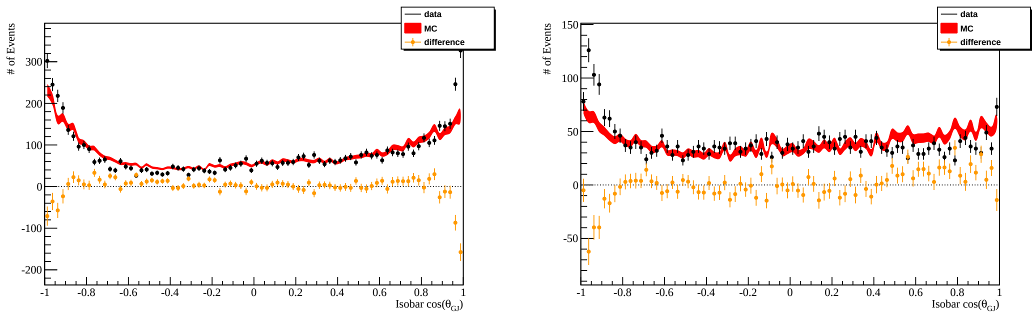

(a) **(b)**

Figure 5.8: $\cos(\theta_{GJ})$ distributions for the 3π mass bin $[1780, 1820]\mathrm{MeV}/c^2$. (a): Charged isobar decay topology. (b): Neutral isobar decay topology.

The second phase space variable in the GJ-frame is ϕ_{TY}. It is instructive to study the histogram summarizing the ϕ_{TY} distributions for all invariant mass bins, which is shown in figure 5.9.

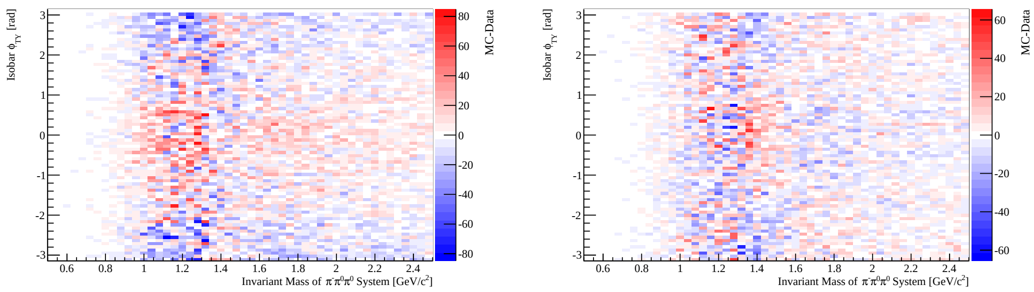

(a) **(b)**

Figure 5.9: ϕ_{TY} differences as a function of the 3π mass. (a): Charged isobar decay topology. (b): Neutral isobar decay topology.

Again, the invariant mass region of the $a_1(1260)/a_2(1320)$, exhibit the largest fit result differences. But, notice that the differences are lower by a factor of two as compared to the $\cos(\theta_{GJ})$ distributions in figure 5.7. At high invariant mass bins, both the neutral and charged isobar case exhibit bands of over- or under-estimation for $\phi_{\mathrm{TY}} = 0$ and $\phi_{\mathrm{TY}} = \pm\pi$. Once again the stable deviations, indicate that the fit model is not able to describe the data.

To verify the magnitudes of the discrepancies determined form the summary histogram, one has the resort to the one-dimensional projections. Figure 5.10 shows the ϕ_{TY} distributions at the 3π mass bin of $[1780, 1820]\,\mathrm{MeV}/c^2$, to analyse the ϕ_{TY} bands at higher invariant masses further.

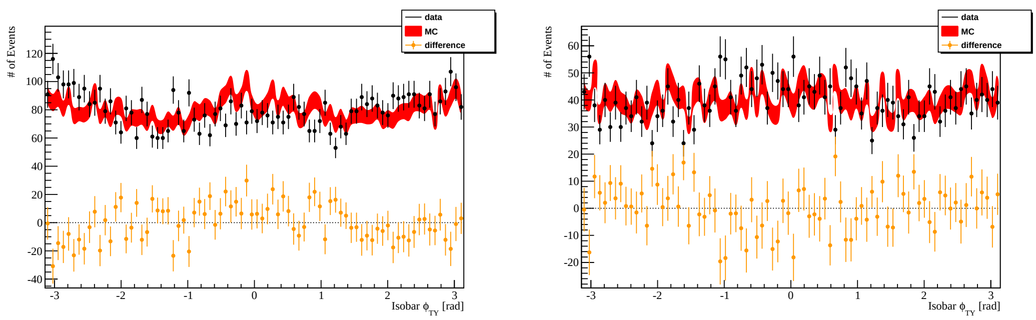

(a) **(b)**

Figure 5.10: ϕ_{TY} distributions for the 3π mass bin $[1780, 1820]\,\mathrm{MeV}/c^2$. (a): Charged isobar decay topology. (b): Neutral isobar decay topology.

Even though the overall agreement seems better, because the statistics in the higher mass bins decreases, the fit is still deviates from the data distribution.

As already mentioned, the number of phase space variables describing the kinematics of the decay is five, and comparisons between the 5-dimensional distributions should be made. Because it is difficult to visualize these distributions, one resorts to their one-dimensional projections. Of course these projections may hide possible correlations between the phase space variables. However, visualizing the correlation between two variables can be done easily. From the isobar model it is natural to investigate the correlation of the two angles from each of the two decay vertices.

The correlation of the two decay angles in the GJ-frame for the invariant mass bin of $[1140, 1180]\,\mathrm{MeV}/c^2$ is shown in figure 5.11.

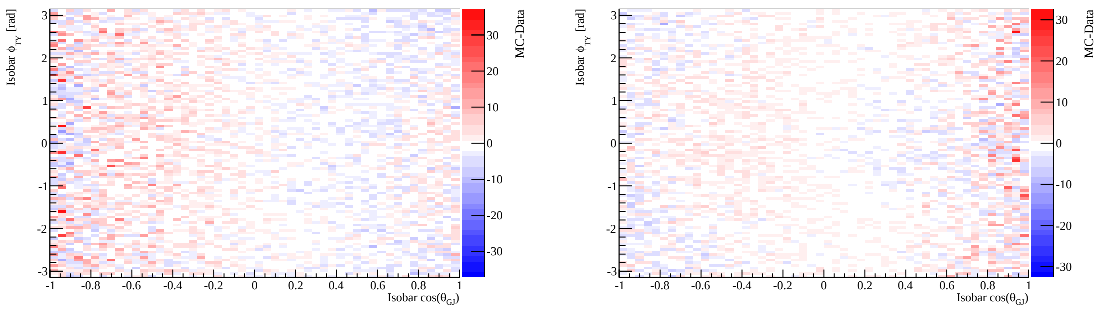

(a) **(b)**

Figure 5.11: $\cos(\theta_{\mathrm{GJ}})$ vs. ϕ_{TY} in the 3π mass bin $[1140, 1180]\,\mathrm{MeV}/c^2$. (a): Charged isobar decay topology. (b): Neutral isobar decay topology.

Of course the disagreement seen in the projections of the same mass bin must be present here as well. For the $\cos(\theta_{\mathrm{GJ}})$ distributions (figure 5.6) these discrepancies can nicely be relocated. For the charged mode the correlations spread continuously over the complete ϕ_{TY} range. On the other hand, the neutral mode shows several regions of correlation, for instance at $\cos(\theta_{\mathrm{GJ}}) = 0.5$, $\phi_{\mathrm{TY}} = 0$.

Because the angular dependence of the full decay is well defined part within the model, it is particularly interesting to look at the phase space variable that carries the main model uncertainty for the individual waves, the isobar mass distribution. As a summary, figure 5.12 shows the differences of the isobar mass distributions for all 3π mass bins.

For both the charged and neutral isobar distribution, the largest differences differences are again in the 3π mass range of 1.0-1.4 GeV/c^2. In particular, a band of larger discrepancy of the charged isobar in the $\rho(770)$ mass region is clearly visible, suggesting an incomplete $\rho(770)$ isobar mass description. In order to study the magnitude of the deviations, one has to refer to the one-dimensional projections, for instance at the invariant mass bin of $[1420, 1460]\,\mathrm{MeV}/c^2$, shown in figure 5.13.

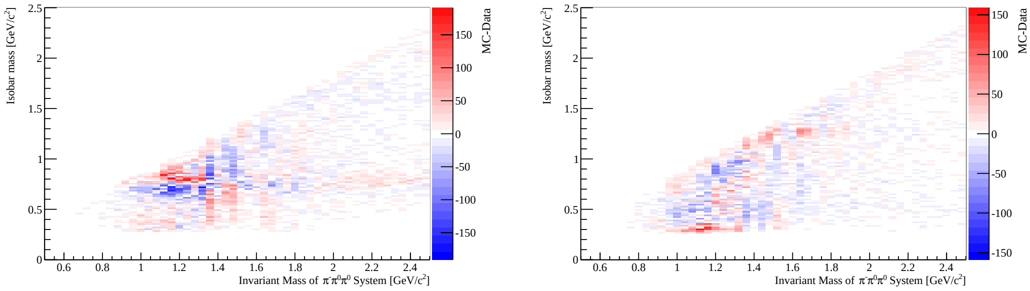

(a) **(b)**

Figure 5.12: Isobar mass differences as a function of the 3π mass. (a): Charged isobar decay topology. (b): Neutral isobar decay topology.

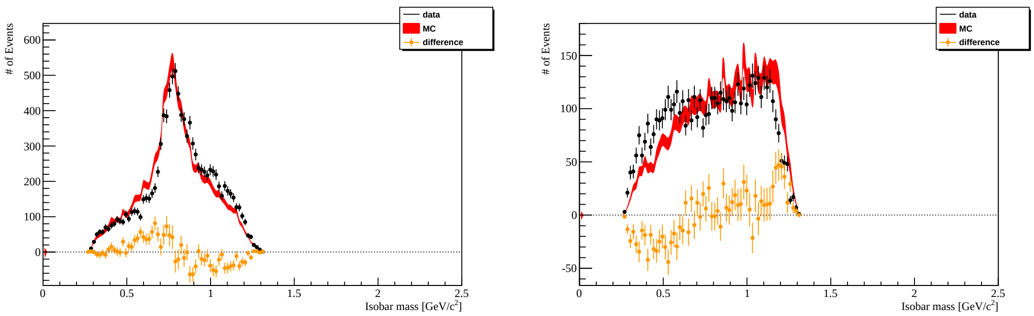

(a) **(b)**

Figure 5.13: Isobar mass distributions for the 3π mass bin $[1420, 1460]\,\mathrm{MeV}/c^2$. (a): Charged isobar decay topology. (b): Neutral isobar decay topology.

Figure 5.13a shows that the disagreement in the charged mode is caused by an asymmetry of the mass distribution. In the neutral isobar mass distribution, a large gap between the fit result and the data exists at an isobar invariant mass of 0.5 GeV/c^2. Most likely the cause for this deviation is the extremely delicate parametrization of the $\sigma/f_0(600)$ isobar.

The remaining two phase space variables (θ_{H}, ϕ_{H}) are the decay angles in the helicity frame, capturing the kinematics of the isobar decays. At first the fit qualities of the $\cos(\theta_{\mathrm{H}})$ distributions are studied. In order to estimate the most problematic fit regions, the histogram summarizing this variable over the complete 3π mass range is regarded.

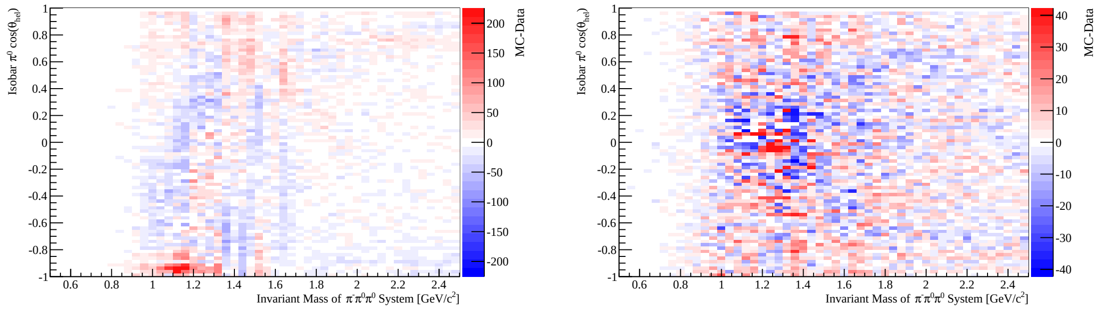

(a) **(b)**

Figure 5.14: $\cos(\theta_{\mathrm{H}})$ as a function for the 3π mass. (a): Charged isobar decay topology. (b): Neutral isobar decay topology.

The difference distribution of the neutral isobar topology looks particularly striking, but as the errors are a factor of four lower as in the previous histograms, the description is fairly good. The fitting disagreements in the charged isobar topology from 1.0 GeV/c^2 to 1.7 GeV/c^2, are dominated by the strong fit overshoot in the invariant mass region of 1.1 GeV/c^2 at $\cos(\theta_{\mathrm{H}}) = -1$. To analyse this discrepancy further, the one-dimensional projection for the invariant mass bin [1140, 1180] MeV/c^2 is shown in figure 5.15a.

Due to the inability of the fit to describe the decrease of the data at $\cos(\theta_{\mathrm{H}}) = -1$, an average solution is chosen that systematically generates disagreements in the remaining parts. In case the acceptance drops towards $\cos(\theta_{\mathrm{H}}) = -1$, the bad fit agreement could mostly be recovered. As mentioned above the deviation in the neutral channel should not be as drastic, which is confirmed by figure 5.15b. Here merely an oscillation of the fit result in the central region produces a disturbance.

For an overview of the last phase space variable, ϕ_{H}, figure 5.16 shows the respective distribution for all total invariant mass bins.

The most conspicuous difference appears in the charged mode at 3π masses of 1.2 GeV/c^2 or with opposite sign at 1.4 GeV/c^2. At higher masses the largest disagreements is in the regions of $\phi_{\mathrm{H}} = 0, \pm\pi$. For the neutral mode the disagreement is smaller in magnitude and looks far more homogeneous in the mass region of 1.0-1.5 GeV/c^2. Similar

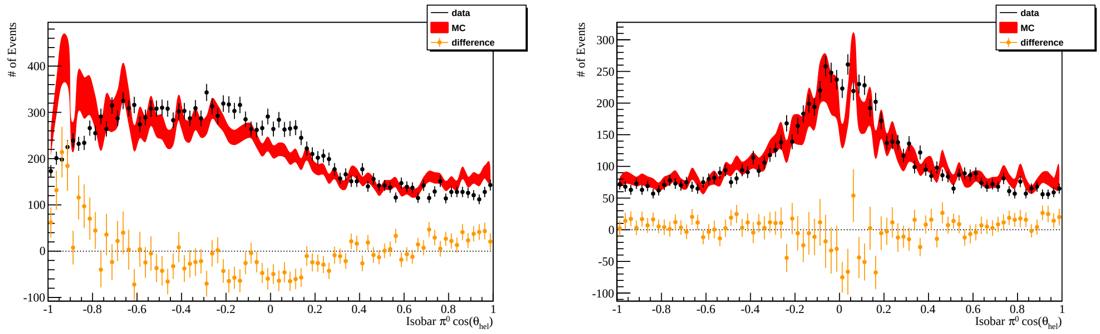

(a) **(b)**

Figure 5.15: $\cos(\theta_{\rm H})$ distribution for the 3π mass bin $[1140, 1180]\,\mathrm{MeV}/c^2$. (a): Charged isobar decay topology. (b): Neutral isobar decay topology.

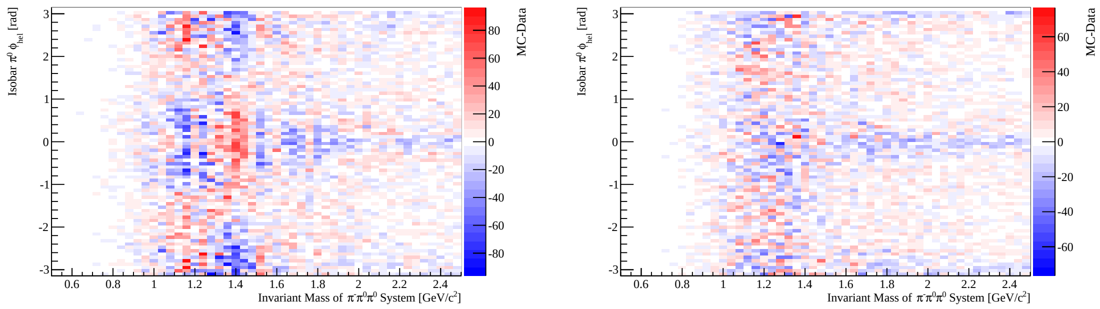

(a) **(b)**

Figure 5.16: $\phi_{\rm H}$ distributions as a function of the 3π mass. (a): Charged isobar decay topology. (b): Neutral isobar decay topology.

to the charged mode, the largest disagreements appear in the regions of $\phi_{\rm H} = 0, \pm\pi$ for higher 3π invariant masses.

Note that the differences are again lower by a factor of 2 than the ones in the previous distributions. Therefore the discrepancies are expected not to be as serious as for instance in figure 5.6a. Figure 5.17 investigates the disagreement at the 3π mass of $1.4\,\mathrm{GeV}/c^2$ further.

Once again the model has problems describing the $\phi_{\rm H}$ distribution of the data for the charged isobar topology. Even though the fit agreement is far better in the neutral isobar case, it is also not perfect.

Completing the comparison of the fit result with the measured data for all of the phase space variables, the correlations of the deviations in the two helicity frame decay angles can be studied. This is shown in figure 5.18 again for the selected mass bin $[1140, 1180]\,\mathrm{MeV}/c^2$.

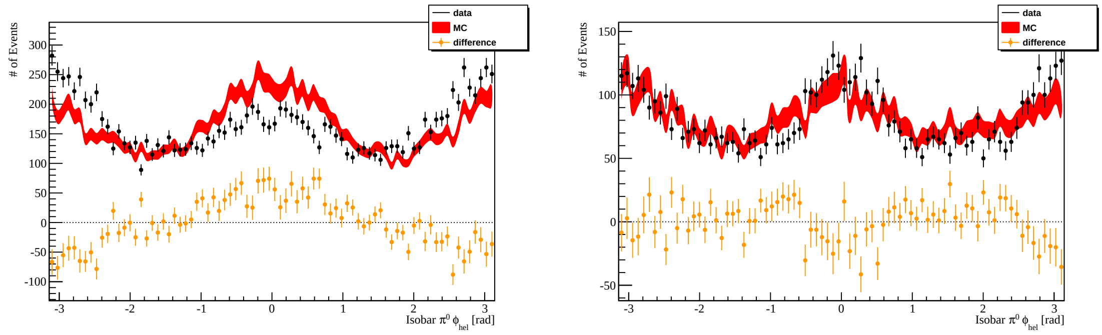

(a) **(b)**

Figure 5.17: $\phi_{\rm H}$ distribution for 3π mass bin $[1380, 1420]\,\mathrm{MeV}/c^2$. (a): Charged isobar decay topology. (b): Neutral isobar decay topology.

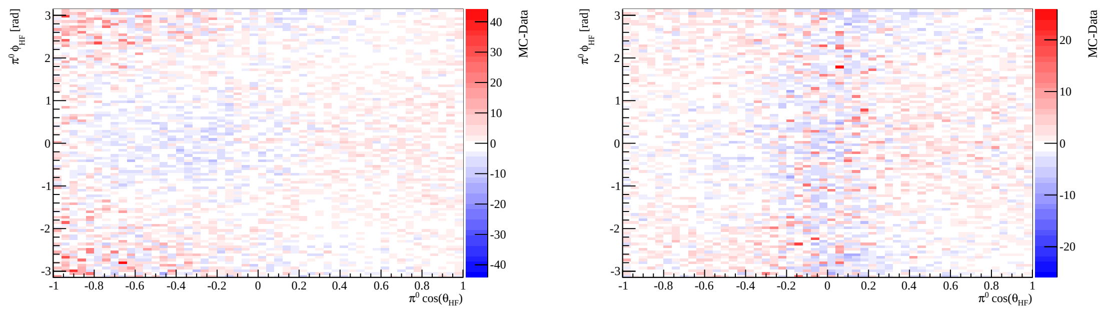

(a) **(b)**

Figure 5.18: $\cos(\theta_{\rm H})$ vs. $\phi_{\rm H}$ in the 3π mass bin $[1140, 1180]\,\mathrm{MeV}/c^2$. (a): Charged isobar decay topology. (b): Neutral isobar decay topology.

In contrast to the two GJ-frame angles, several regions of distinct correlation can be seen. While the areas of $\cos(\theta_{\rm H}) = -1$, $\phi_{\rm H} = \pm\pi$ and $\cos(\theta_{\rm H}) = 1$, $\phi_{\rm H} = 0$ show an overestimation of the fit result, the regions with opposite $\cos(\theta)$ sign exhibit an underestimation.

5.4 Summary & Conclusions

The comparison of the two PWA frameworks in the neutral channel shown in section 5.2 shows an overall fair agreement. Disregarding the small data set differences, the discrepancies due to the choice of the starting parameters are the most serious and can explain most of the observed deviations. To investigate this further, fits with identical starting values should be carried out. Then the remaining differences are related to different model implementations and minimizers. On the basis of the strong dependence on the start parameters, it is recommended to perform at least $\mathcal{O}(100)$ fits with various start values for general fits.

Also the missing background in the flat wave for both frameworks is suspicious. As the fit results are zero over the whole 3π mass range, the case of overfitting is the most probable cause. Of course also the missing acceptance correction can contribute to this, however, here one would expect to see at least some incoherent background in some mass bins.

The basic message for the weighted MC comparisons is that the fit results and data show a fair agreement, apart from some differences which are probably caused by the missing acceptance correction. However, before any deviations can be appointed to problems of the fit model, a full acceptance correction is required. Conversely, some of the observed disagreements can already provide informations to the expected problematic areas of the acceptance correction and fit model. The strongest discrepancies are in the central mass regions of the $a_1(1260)$ and $a_2(1320)$. Even though the overall agreement is better at higher massbins, the borders and central areas of angular distributions remain problematic regions. Additionally, when making two-dimensional projections, for instance plotting both decay angles, correlations are revealed. Especially the helicity frame shows significant correlations. As particularly these correlation histograms require high statistics, a fully acceptance corrected high statistics analysis will allow a conclusive interpretation of the deviations corresponding to the used fit model.

Chapter 6

PWA results from different event selections

In this chapter an extension to the basic event selection of chapter 4 is given. Already some of the flaws of the basic event selection, and additional statements for improvements were pointed out.

The implementations for these improvements are presented in section 6.1. By including events with 5 and 6 gammas more statistics is attained. On the contrary, this results in a higher combinatorial background and some adjustments for the suppression of the same are made.

Finally, the influence on the PWA is studied in section 6.2, in which a comparison of the PWA results to the basic selection is given. At this point the form of the intensity distributions for individual waves and the ratios of yields for the main resonances are compared.

A summary of the conclusions for the extended event selection is given at the end of this chapter.

6.1 The Event Selection Extensions

The event preselection in 4.2 was designed to incorporate the informations needed by the extension presented here. The reason for not using the newest reconstruction codes and software pieces currently available, but the same as in the basic selection, is to exclude their dependence on the PWA results, hence only the modifications in the event selection are responsible.

An event selection on the full statistics using the newest software versions and reconstruction code is presented in chapter 7. Here also the additional information provided by the new reconstruction code is used.

The overview of the complete extended final event selection is shown in Table 6.1. The differences and improvements are discussed below in more detail. Constraints which are identical to the basic event selection will not be mentioned any further, as they were already motivated and explained in full detail in chapter 4.

Applied cut	# of events (extended)
all preselected events	$4.99793 \cdot 10^7$
real target cut	$4.17754 \cdot 10^7$
$4 \leq N_\gamma \leq 6$	$1.09639 \cdot 10^7$
$E_{\pi^-} < 185.00\,\text{GeV}$	$1.14157 \cdot 10^7$
$\lvert M_{\pi^0} - 134.98\,\text{MeV}/c^2\rvert < 20\,\text{MeV}/c^2$	$2.60295 \cdot 10^6$
$N_{\text{proton}} = 1$ & $\lvert p_{\text{proton}}\rvert > 250\,\text{MeV}/c$	$1.76163 \cdot 10^6$
kaon veto: majority ≥ 6	$1.72263 \cdot 10^5$
$\lvert\Delta\phi\rvert < 0.20\,\text{rad}$	$8.18705 \cdot 10^5$
$0.10\,(\text{GeV}/c)^2 < t' < 1.00\,(\text{GeV}/c)^2$	$6.44822 \cdot 10^5$
$\lvert M_{\pi^0} - 134.98\,\text{MeV}/c^2\rvert < 16\,\text{MeV}/c^2$	$5.24131 \cdot 10^5$
$\lvert\Delta P_\perp - 16\,\text{MeV}/c\,\rvert < 110\,\text{MeV}/c$	$4.06470 \cdot 10^5$
$\lvert E_{\text{beam}} - 190.50\,\text{GeV}\rvert < 6.00\,\text{GeV}$	$2.81639 \cdot 10^5$
multiplicity $= 1$	$2.77405 \cdot 10^5$

Table 6.1: Summary of the full extended final event selection. Note that the number of gamma cut (N_γ) includes energy scaling and thresholding for the individual calorimeters

Key Note

Before the individual improvements are addressed, the concept of the 4+ γ selection[1] is discussed. Each event, containing an arbitrary amount of gammas, possesses a total combinatorial factor, consisting of the product of an intrinsic and extrinsic part. The latter is the number of combinations of choosing 4γ from the total count, which is 1, 5

[1] In a 4+ γ selection events with 4γ and higher gamma counts are regarded.

or 15, for events containing 4, 5 or 6γ's. Independent of the number of photons regarded in the event, the intrinsic combinatorial factor is three for selecting two neutral pions of the four gammas. Altogether one obtains total multiplicities of 3, 15 or 45 for events containing 4, 5 or 6γ's. This can be seen in figure 6.1a.

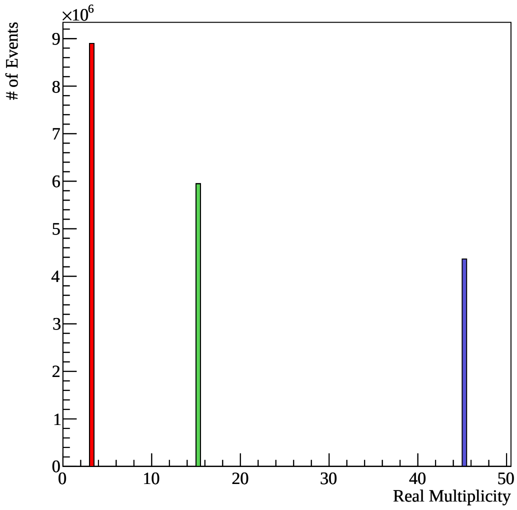

(a) Total combinatoric factor before any cuts have been applied. The blue, green and red part of the histogram correspond to the 4, 5 and 6 gamma case, respectively.

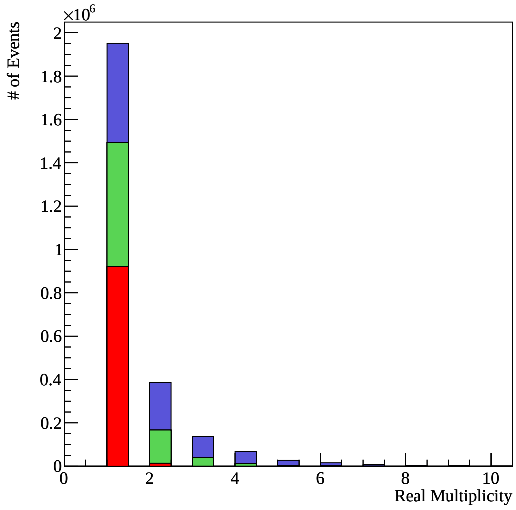

(b) Mulitplicity distribution of events after having applied the π^0 mass cut. For each event exactly on entry is made.

Figure 6.1

This separation of the combinatorics into the extrinsic and intrinsic part is a crucial for the further filtering approach. While the intrinsic filters are able to reduce both the intrinsic and extrinsic components of the multiplicity, the extrinsic filters are only able to decrease the extrinsic part of the multiplicity. However, this holds only in the case when no π^0 mass kinematic fitter was applied. As soon as the kinematic fitter was active, each real combination[2] now has a unique gamma composition. Then a separate treatment for the further filtering process is required. In other words, the application of the π^0 mass fitter upgrades all of the extrinsic filters to intrinsic ones.

4-6γ Extension

At first a comparison of the π^0 reconstruction efficiency for the new 4-6 gamma selection with respect to other gamma counts is made. The one-dimensional π^0 mass distributions for various gamma counts are shown in figure 6.2, and were constructed after all cuts except the multiplicity filter, as table 6.1 indicates. Note that for this new selections

[2]A combination is real, if it includes both the extrinsic and intrinsic part.

without the π^0 mass filter have been made.

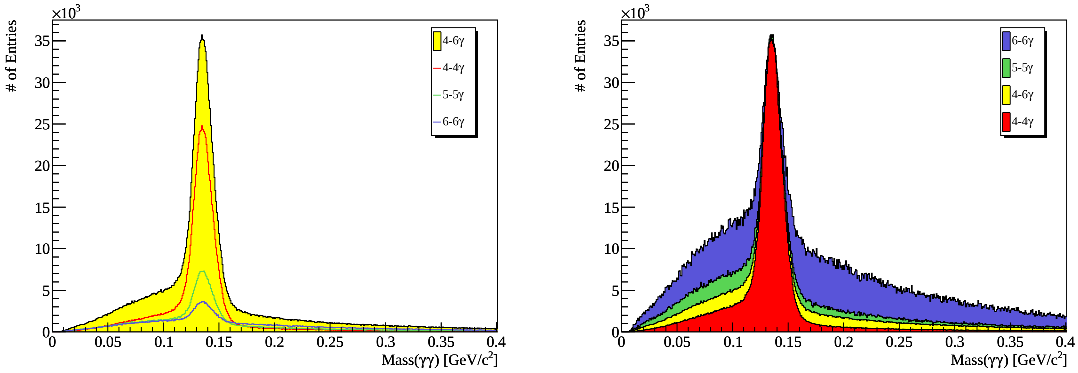

(a) (b)

Figure 6.2: (a): One-dimensional mass distributions for different gamma counts after all cuts except the multiplicity. Of course no restriction on the π^0 mass have been made. The red curve corresponds to 4γ events and exhibits the smallest background relative to the signal. In green, blue and yellow the 5γ, 6γ and 4-6γ selections are shown, respectively. For each combination consisting of two γ pairs, both the π^0 masses enter the histogram. Every event may possess more than one combination. **(b):** Same as in (a), however, here all curves have been scaled to the 4-6γ graph (yellow).

Because there is no cut on the multiplicity of the event, the different gamma count curves are subject to non-identical combinatorics and therefore a direct comparison of magnitudes is not possible. Figure 6.7b shows this multiplicity distribution. Notice that the π^0 mass kinematic fitter enabled the discrimination for the intrinsic combinatorics, as multiplicities of one are the main contribution. Nevertheless figure 6.2a shows that, even though the amount of reconstructed neutral pions decreases to higher gamma counts, their amount is still significant. Apart from the multiplicities, a more quantitative comparison of the signal to background ratios is shown in figure 6.2b, in which the π^0 mass distributions were scaled to the 4-6γ case.

New ECAL Thresholds

Another improvement that was made, is determination of new energy thresholds for the individual electromagnetic calorimeters, that suppress the mainly low energetic noise in the ECAL's. In the basic event selection the applied thresholds of 0.25 GeV and 1.0 GeV for ECAL1 and ECAL2, actually lie close to the hardware thresholds of the calorimeters, at which point almost no noise reduction was achieved. Instead the thresholds of 0.9 GeV and 2.1 GeV were used. Their determination is shown in Appendix B. The energy scaling factors for the two calorimeters are equivalent to the basic event selection.

Elastic Scattering - π^0 Mass Correlation

As already mentioned in chapter 4, the low π^0 mass region corresponds to noise, and is strongly correlated to the elastic scattering events. Because the elastic scattering filter is completely insensitive to any combinatorics (neutral-type), it was moved in front of the pion mass filter to show the effect on this low mass background. Comparing figure 6.3 with 4.4, the reduction of the low mass region and the signal-to-noise enhancement of the π^0 bands becomes apparent. The applied mass cut is identical to the basic event selection and constitutes to $20\,\mathrm{MeV}/c^2$ mass circle around the neutral pion mass value of $0.13498\,\mathrm{GeV}/c^2$.

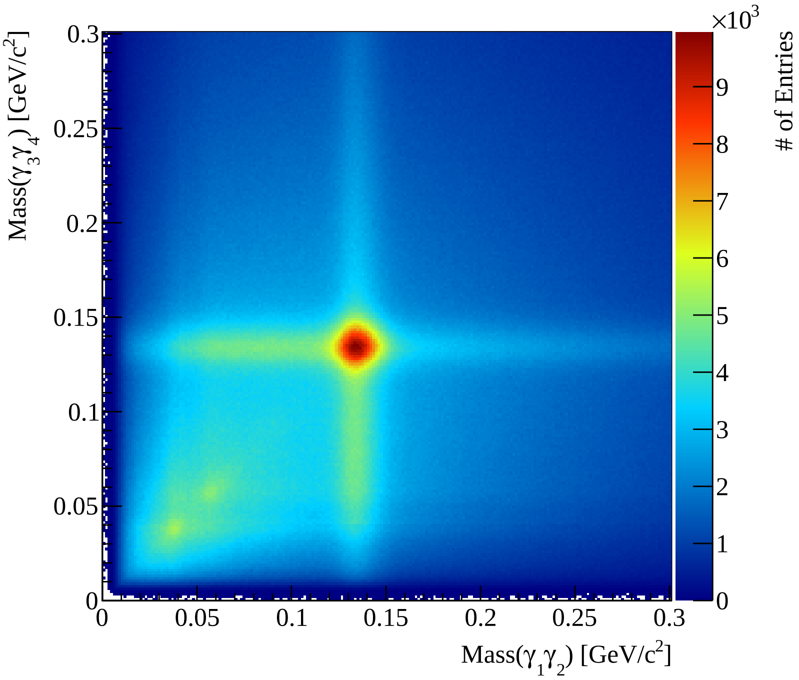

Figure 6.3: This figure shows the 2D mass distribution of 4 gammas grouped into two neutral pions. As also events with 5 and 6 γ are included here, at least 3 entries per event are made.

Now that first filter that is sensitive to combinatorics, even intrinsic, is applied, the distribution of the multiplicities should change accordingly. One expects an accumulation at low multiplicities and a rapid drop to higher multiplicities. Figure 6.1b shows the results.

As most of the 4 gamma events only contain a single $2\pi^0$ combination, these events mainly contributed to the multiplicity of 1. Events consisting of more gammas will have larger multiplicity tails and their maximum will also shift to higher values. However, in the case of 5 and 6 γ the maximal multiplicity is still at 1. Note that the multiplicities of 10 are existent, but are too few to show up in the unzoomed histogram.

Beam Correction for $\Delta\phi$ Cut

The next change that was made is the beam correction of the $\Delta\phi$ filter which was neglected in the basic selection. The $\Delta\phi$ distribution represents the angular part of transverse momentum conservation of the outgoing pion system and the recoiling proton with respect to the beam axis.

Because the beam inclination on the xy-plane is small, the z-axis of the lab frame was used to approximate the beam axis in the basic selection. In the extended selection this was accounted for by rotating the proton and outgoing pion system in the lab frame so that the z-axis is aligned with the beam direction. This is illustrated in figure 6.4. The effect of the beam correction can be extracted from figure 6.5. From the difference graph in red one can see that events get pulled towards zero of the distribution.

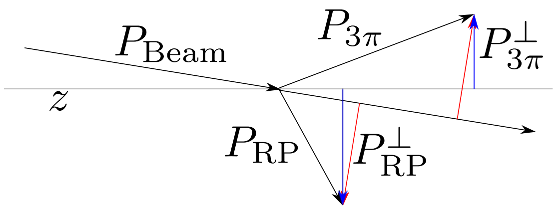

Figure 6.4: Visualization of the transversal momentum conservation and beam correction.

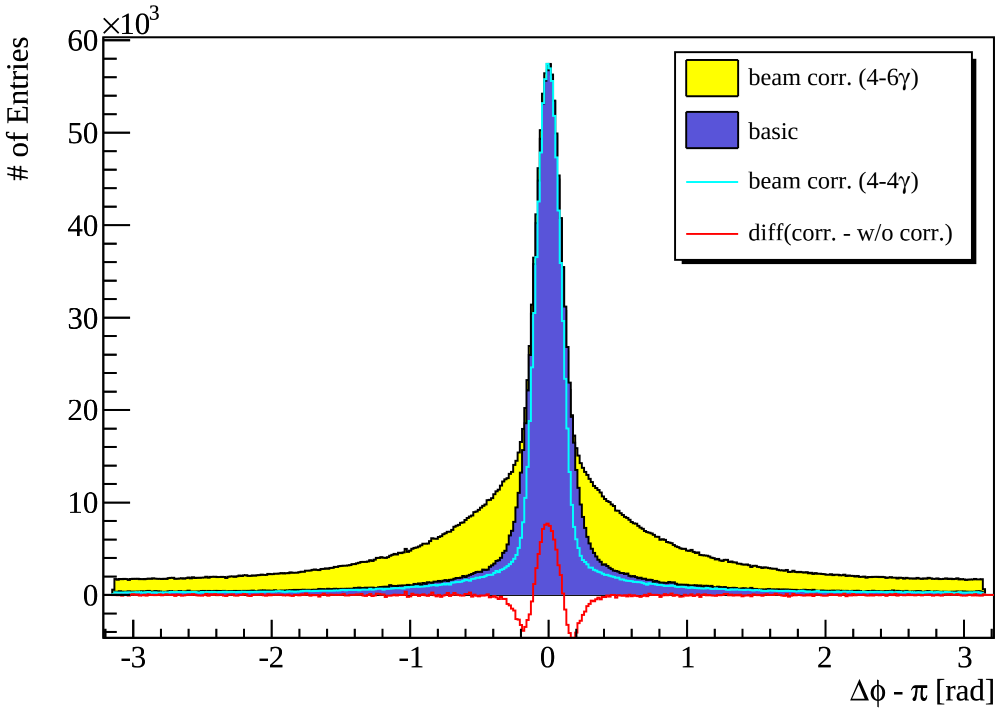

Figure 6.5: $\Delta\phi$ distributions for various extended event selections and the basic selection, before a cut on this distribution was made. Note that a factor of π was subtracted to center the peak at 0. The yellow distribution is the full extended selection with the beam correction, while the difference without the beam correction is shown in red. The blue and cyan distributions are from the basic event selection and the extend event selection with only 4γ's.

Additionally the distribution of the extended event selection decreases slower at ± 0.2 rad than the basic event selection. This arises purely from the higher gamma count, as the extended selection with only 4γ exhibits a similar structure as the basic selection. For this reason the selection interval was not changed and remains at ± 0.2 rad.

New $\Delta P_\perp$ Cut

The introduction of larger backgrounds, initiated the search for another constraint which is able to improve the signal to noise ratio. Since the noise introduced by the calorimeters is mainly low energetic, the momenta of reconstructed π^0 using these noise clusters are also low. As the transversal momentum conservation was only checked in the direction, the remaining magnitude comparison can provide exactly the necessary informations. The difference of the two magnitudes is shown in figure 6.6a.

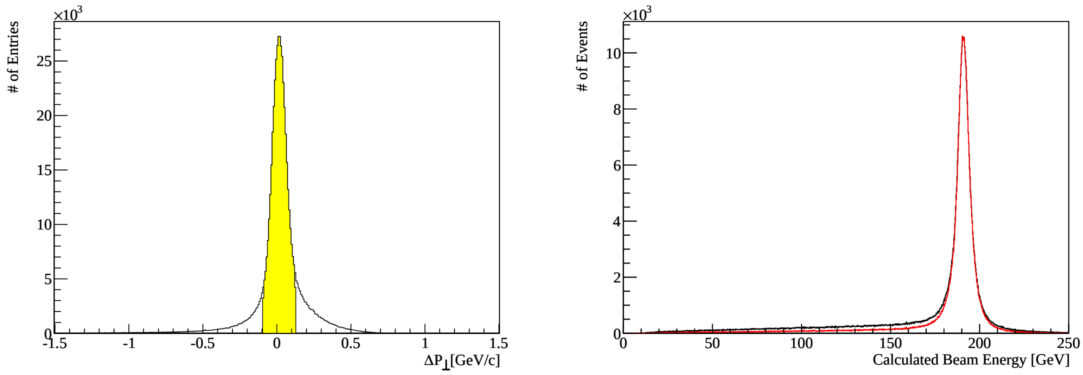

(a) Difference of transversal momentum magnitudes of the outgoing pion system and the recoiling proton. The yellow area corresponds to the cut that was applied in the selection.

(b) Exclusivity distribution before (black) and after (red) the transversal momentum magnitude filter has been applied. The red curve was scaled to the black, in order to highlight the effect on the improvement on the signal to noise ratio. From table 6.1 it is clear that all cuts have been applied except the exclusivity and the multiplicity.

Figure 6.6

Based on the short tails of the distribution, caused by the correlation with different filters which already removed most of the background, the improvement in the signal to noise ratio seems limited. Nevertheless the filter was applied and the exact cut parameters can be extracted from table 6.1. The small mean value offset is due to the slight underestimation of the recoiling proton momenta by the RPD. Since a neutral pion mass cut has already been applied the exclusivity distribution is now the decisive quantity for indications of the signal to noise ratio. The effect on the exclusivity distribution can be taken from figure 6.6b. On the basis of this comparison, a suppression of the background by a factor of two becomes apparent.

Performance Check via Exclusivity

At this point it is useful to make another comparison between the events of different gamma counts, because the exclusivity is the last major cut and possibility to view the signal to background ratio. Before a comparison of the signal to background relation for the different gamma counts was performed with the π^0 mas distribution. A direct comparison of the yields was not possible as the multiplicities for events of different gamma counts were non-equal. This was shown in figure 6.1b.

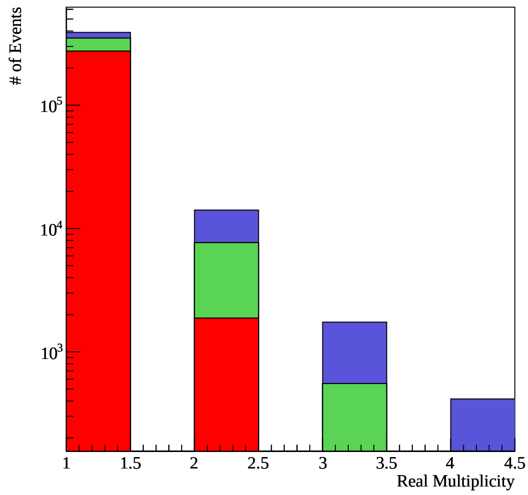

(a) Event multiplicities for the extended selection before the exclusivity cut. The blue, green and red part of the histogram correspond to the 4, 5 and 6 gamma case, respectively. Note the y-axis log scale.

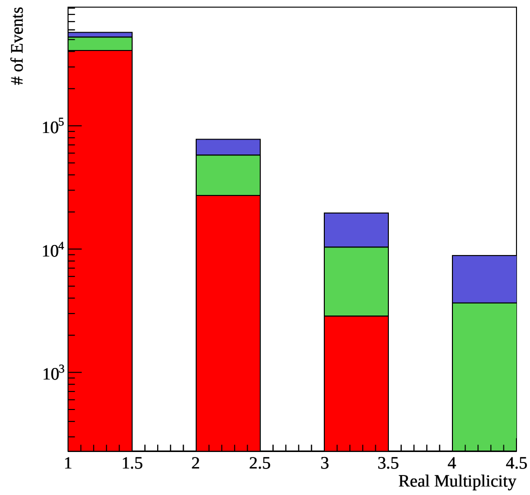

(b) Final event multiplicities for the extended selection without the π^0 mass cut. The blue, green and red part of the histogram correspond to the 4, 5 and 6 gamma case, respectively. Note the y-axis log scale.

Figure 6.7

Comparing this to the multiplicity distribution for the normal extended selection before the exclusivity cut as in table 6.1, which is depicted in figure 6.7a, one can see that for all gamma counts the main contribution is from a single combination. Therefore the exclusivities for the different gamma counts can with good approximation directly be compared. This is shown in figure 6.8.

Figure 6.8a illustrates that the signal intensities decreases for events containing more photons, while the background stays the same, overall reducing the signal to background ratio. Based on this finding, and of figure 6.2, the gamma count range for the full extended event selection was restricted to 4-6γ, as the signal yield for events with an even higher number of photons would mainly contribute to the total background. Scaling all these distributions to an equivalent maximum, shown in figure 6.8b, this signal to noise reduction is visualized explicitly.

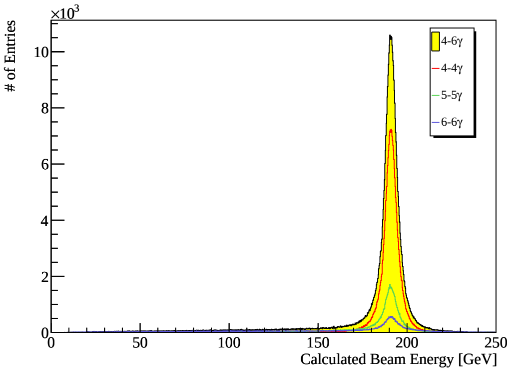

(a) Exclusivity peaks for different gamma counts. The 4γ case is shown in red, 5γ in green, 6γ in blue and 4-6γ in yellow.

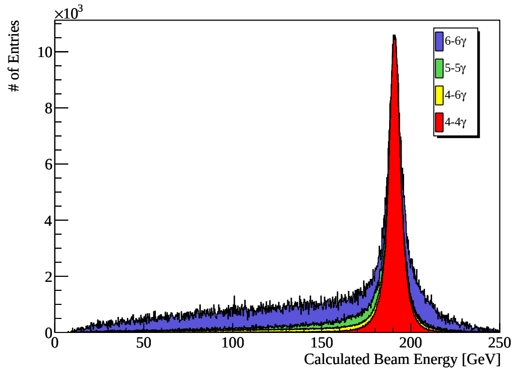

(b) Exclusivity peaks for different gamma counts, while all distributions have been scaled to the yellow curve which represents the 4-6 γ case, naturally being the strongest distribution. The coloring scheme is identical to (a).

Figure 6.8

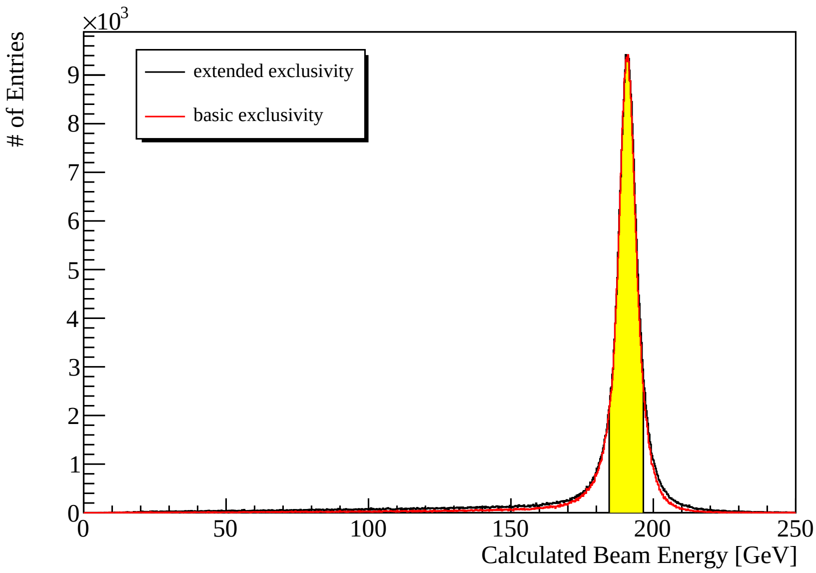

Figure 6.9: Exclusivity distribution before the exclusivity cut itself as in table 6.1. The yellow shaded part illustrates the cut that has been applied in the extended event selection.

Final Multiplicities

At last, a cut on the multiplicity is performed, discarding all events containing more than one combination of 4 photons into the $\pi^0\pi^0$ final state pions that passed all previous filters. Having applied all filters beforehand, one expects that the multiplicities are mostly one. Taking a look at figure 6.10a the expectation is verified. In conclusion, the plan of reducing the total number of combinations per event to a single one by using the extrinsic and intrinsic filters is perfectly realizable. To gain a picture on the relative values of multiplicities larger than two, a zoomed histogram is displayed in figure 6.10b.

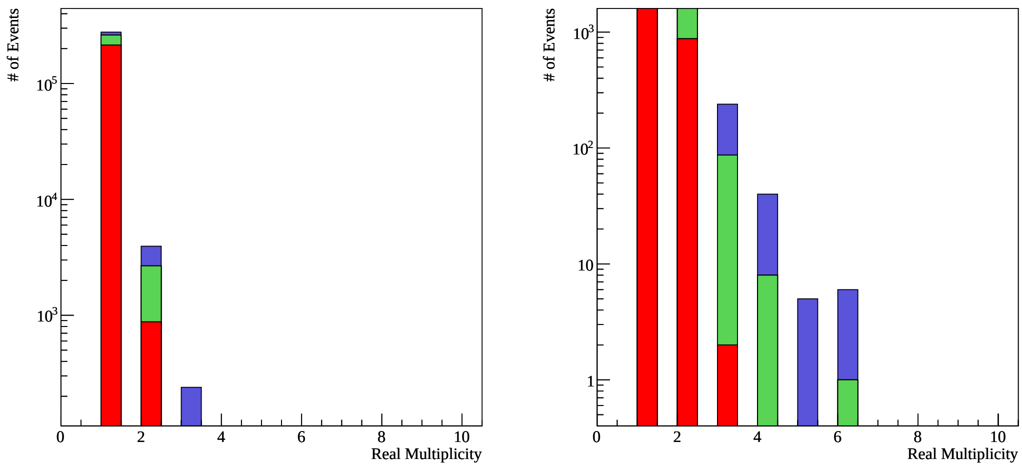

(a) (b)

Figure 6.10: Final multiplicities are shown, before the cut on the same has been made. While 6.10b is zoomed to reveal the distribution of higher multiplicities, 6.10a is the unzoomed case in log scale.

3π Invariant Mass

Altogether one obtains 277 405 final selected events, as compared to the basic selection which resulted in 193 636 events. Furthermore, figure 6.9 shows that the signal to background ratios are similar. Hence the extended selection yields an additional 43 % of events with an unchanged signal to background ratio.

Finally, the comparison of the total invariant mass spectra for the extended and basic event selection can be seen in figure 6.11.

From the top histogram the statistics gain becomes apparent. Also, both distributions exhibit similar shapes. The bottom histogram shows the ratio of the invariant mass distribution of the extended event selection and the basic event selection. Evidently, the extended event selection yields more low mass states and less high mass states as compared to the basic event selection. The constant slope of the ratio curve suggest a

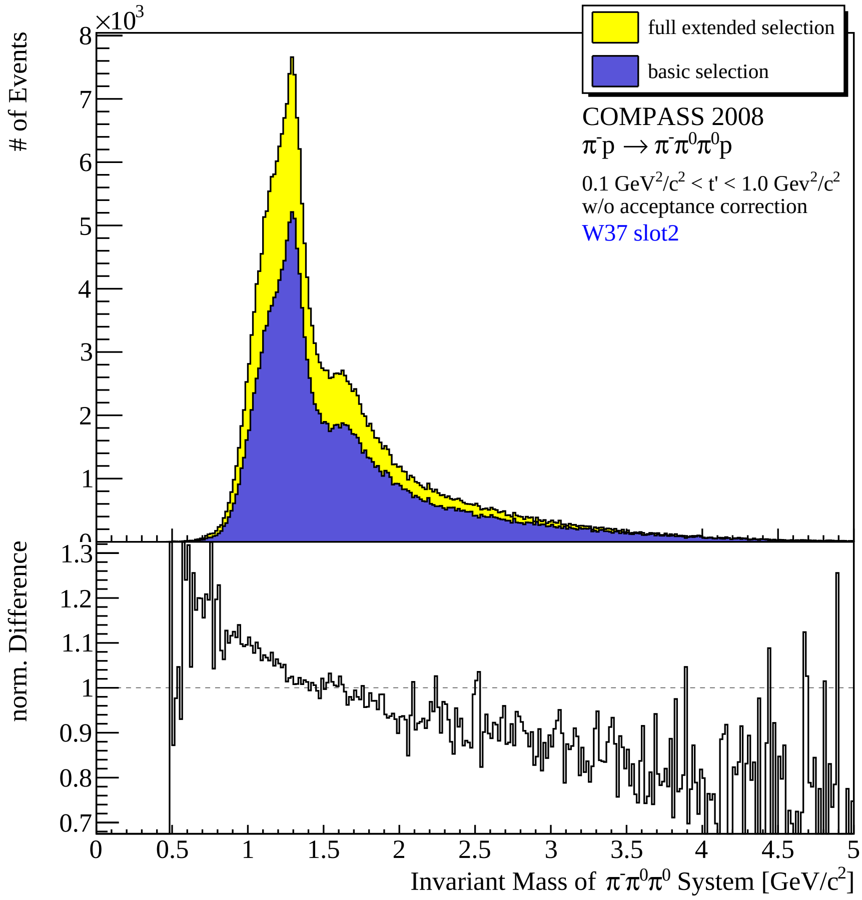

Figure 6.11: Top: 3π invariant mass distributions for the full extended event selection (yellow) and the basic event selection (blue).
Bottom: Ratio of the 3π invariant mass distribution of the extended selection and the basic event selection, which was normalized to the former by integrals.

systematic effect in the event selection changes. This is studied in more detail in the next section.

6.2 PWA results

After having selected the events as explained above a mass independent fit is carried out. To gain insight into the performance and changes of the extended to the basic selection, all other inputs of the PWA are kept identical. This means an equal mass range/binning and waveset, which can be taken from from table 5.1. Also the decay amplitude normalization integrals have been computed with the same phase space MC events as in the basic event selection. As the same starting parameters are chosen for the individual fits appearing in this section, the dependence on the fitting procedure is completely absent. Note that this means only a single fit has been carried out for each selection.

Due to the restriction in the invariant mass $[0.5, 2.5]\,\mathrm{GeV}/c^2$ the total number of fitted events is reduced to 271874.

In general one expects an enhancement of all intensities as the waveset is kept identical. This results also in smaller relative statistical errors. As the introduced background is slightly larger this will reflect itself in the obtained PWA results. As a first benchmark, a comparison of the 2^{++} wave containing the well defined state a_2 is an ideal metering point. This is depicted in figure 6.12a. Here at first sight, all expectations are met. The wave exhibits the same structure, while the intensity is increased by an amount related to the growth of the data set.

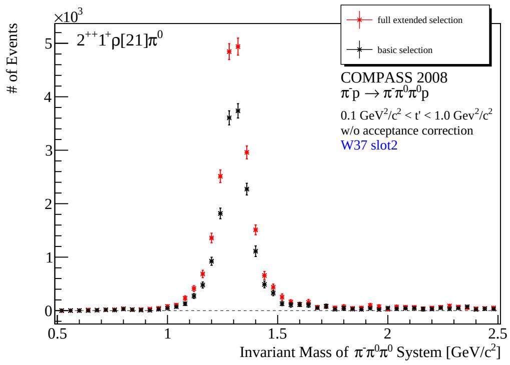

(a) Comparison of the intensity for the $1^-2^{++}1^+\rho(770)[21]\pi^0$ wave containing the $a_2(1320)$ resonance.

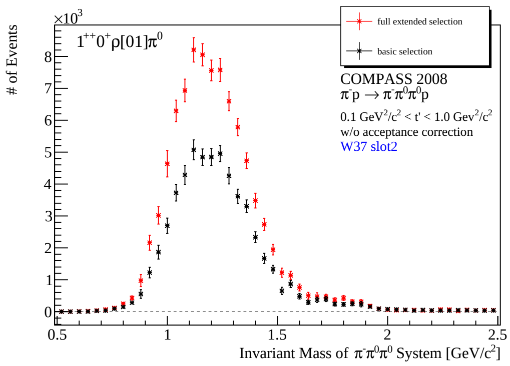

(b) Comparison of the intensity for the $1^-1^{++}0^+\rho(770)[01]\pi^0$ wave containing the $a_1(1260)$ resonance.

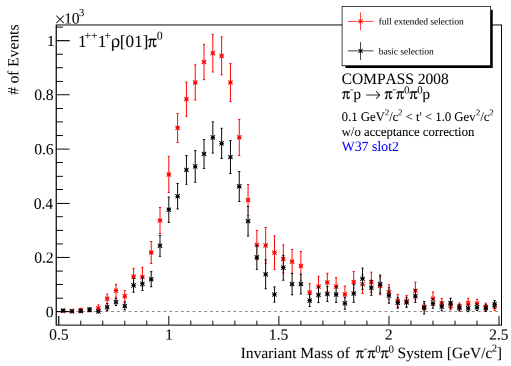

(c) Comparison of the intensity for the $1^-1^{++}1^+\rho(770)[01]\pi^0$ wave containing the $a_1(1260)$ resonance.

Figure 6.12

The second well defined state is the a_1, which should be present in 1^{++} waves. In figure 6.12b and 6.12c, the two 1^{++} waves with the largest intensity gain are displayed.

Similar to the 2^{++} wave an intensity gain can be observed, however, a more precise comparison immediately shows an inconsistency. The intensity gain of the 2^{++} and the 1^{++} waves are of different magnitude, which would implicate unequal production intensities ratios of the a_1 and a_2 states for the two selection. Since this is not plausible observation, a systematic effect of the extended event selection must be responsible. A study revealing the cause for this discrepancy is shown later in this section.

The third intensely produced state is the $\pi_2(1670)$ appearing in 2^{-+} waves, which are shown in figure 6.13a and 6.13b.

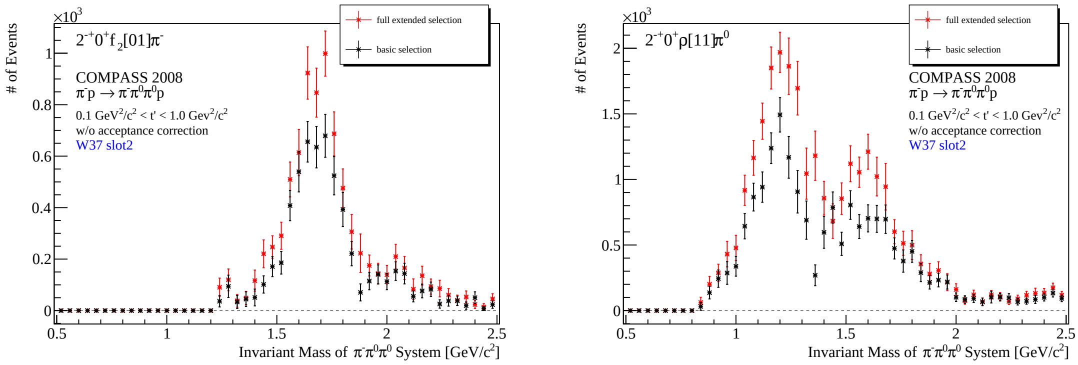

(a) Comparison of the intensity for the $1^-2^{-+}0^+f_2(1270)[02]\pi^-$ wave containing the $\pi_2(1670)$ resonance.

(b) Comparison of the intensity for the $1^-2^{-+}0^+\rho(770)[11]\pi^0$ wave containing the $\pi_2(1670)$ resonance.

Figure 6.13

Here the expected intensity gain of approximately 50 % can be seen. Because the development of the fits along the total invariant mass is not as smooth as in the 1^{++} and 2^{++} waves shown above, the ratios of the $\pi_2(1670)$ w.r.t. the $a_1(1260)$ and $a_2(1320)$ will not be studied in detail. The non-continuous fit results of the extended selected events in the $\pi_2(1670)$ region, is suspicious. Usually such jumps in the distributions are caused by the thresholding of waves, which are included at a certain certain mass, hence absorbing parts of the total intensity. However at the 3π mass of $1.7\,\mathrm{GeV}/c^2$ all of the thresholds are already nullified.

From the COMPASS physical point of view the most interesting waves are ones with spin-exotic quantum numbers, for instance with 1^{-+}, which is shown in figure 6.14a. Although the intensity oscillates in the 1.3-1.8 GeV/c^2 mass region, the overall observed increase of the intensity is consistent with the larger data set. Other less intense waves, that are not shown here, yield similar improvements as figure 6.14a.

The discrepancy of in the ratio of the $a_1(1260)$ and $a_2(1320)$ shall now be studied in more detail. Because the only input to the PWA that changed is the different data set, the task lies within finding the filters which varied from the basic selection and produce this disagreement. Therefore several intermediate event selection have been carried out, gradually approaching the basic selection from the full extended selection.

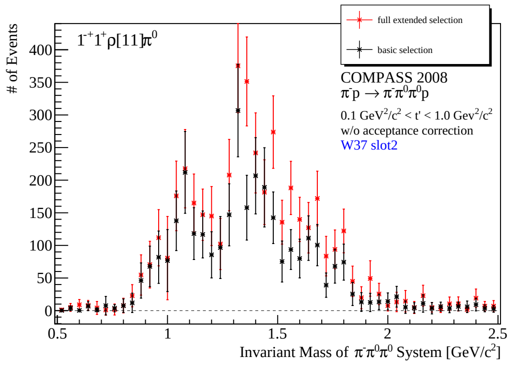

(a) The spin-exotic $1^{-}1^{-+}1^{+}\rho(770)[11]$ wave.

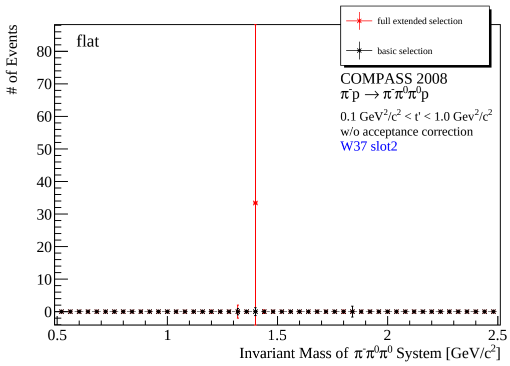

(b) Comparison of the flat wave for the full extended to the basic event selection.

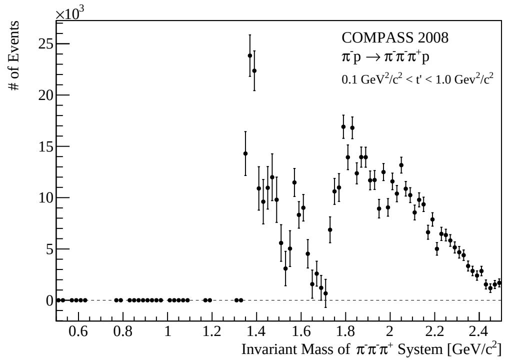

(c) Flat wave of charged $\pi^{-}\pi^{-}\pi^{+}$ final state of ongoing analysis by courtesy of Florian Haas.

Figure 6.14

In order to make a statement on the actual production intensities, the 1^{++} and 2^{++} spin totals are regarded, in which all waves of the given J^{PC} combination are coherently added. Because the 2^{++} wave is extremely well defined, the integral ranging from 1.1-1.5 GeV$/c^2$ is used as the normalization for the diverse event selections. The following graphs always show the 1^{++} spin totals for the full extended event selection in black and the basic event selection in red. The blue intermediate selections represent selections between the two reference selections. All graphs have been scaled accordingly to attain equal normalization integrals in the a_2 region as defined above.

Since the biggest variation originates from the inclusion of 5 and 6 gamma events, at first an intermediate selection which was constraint to only 4γ per event was generated. Figure 6.15 shows the results of the a_2 normalized 1^{++} spin totals.

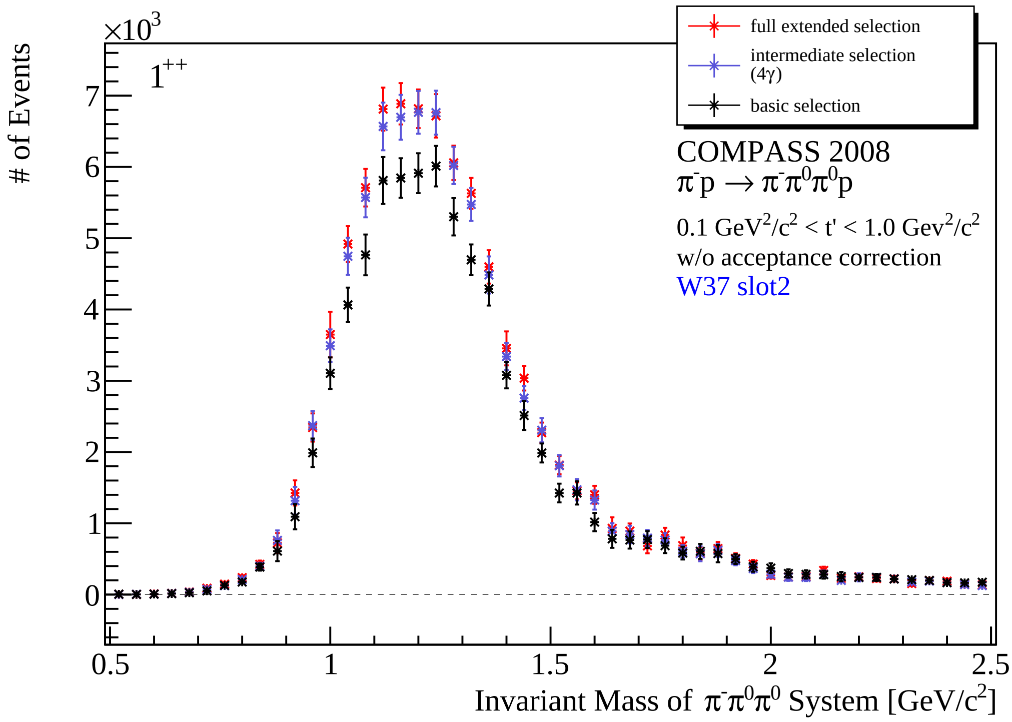

Figure 6.15: 1^{++} spin totals scaled by the normalizations calculated in the a_2 region of the 2^{++} spin total. The intermediate selection in blue only uses events containing 4γ instead of 4-6. Otherwise it is equivalent with the full extended event selection. The red and black graph correspond to the fit results using the full extended event selection and the basic event selection.

Most of the fit results in the a_1 region indicate a small decrease of intensity once events with only 4 photons are used. There are two possible explanations for this effect. First of all, the flat wave, shown in figure 6.14b, does not absorb any background. Therefore the background is somehow distributed to the remaining physical waves. Because combinatorial background for the 4-6 gamma events is higher and the 1^{++} waves are known to preferentially absorb background, this deviation could be explained.

Otherwise the events containing 5 or 6 photons increasingly originate from produced a_1 states, suggesting a correlation of the 1 or 2 "noise" gammas to the angular distribution of the produced states. For instance, the charged pion in the a_1 could preferentially create more showers in the calorimeters that are misidentified as a photon.

In order to make a detailed statement, a detailed study is required. In this case the simplest way to proceed, is to fix the flat wave problem, at which point this background would then get absorbed by the flat wave and former hypothesis is proven. For comparison the flat wave of the $\pi^-\pi^-\pi^+$ channel is depicted in figure 6.14c, in which even though the values do not develop continuously over the mass bins, a rudimentary phase-space-like distribution can be seen.

Because the influence of the beam correction on the a_1/a_2 ratio are not questionable, as merely the correct way of the selection is chosen, the next step is the additional omission of the $\Delta P_\perp$ filter. The blue graph in figure 6.16 shows the results, respectively.

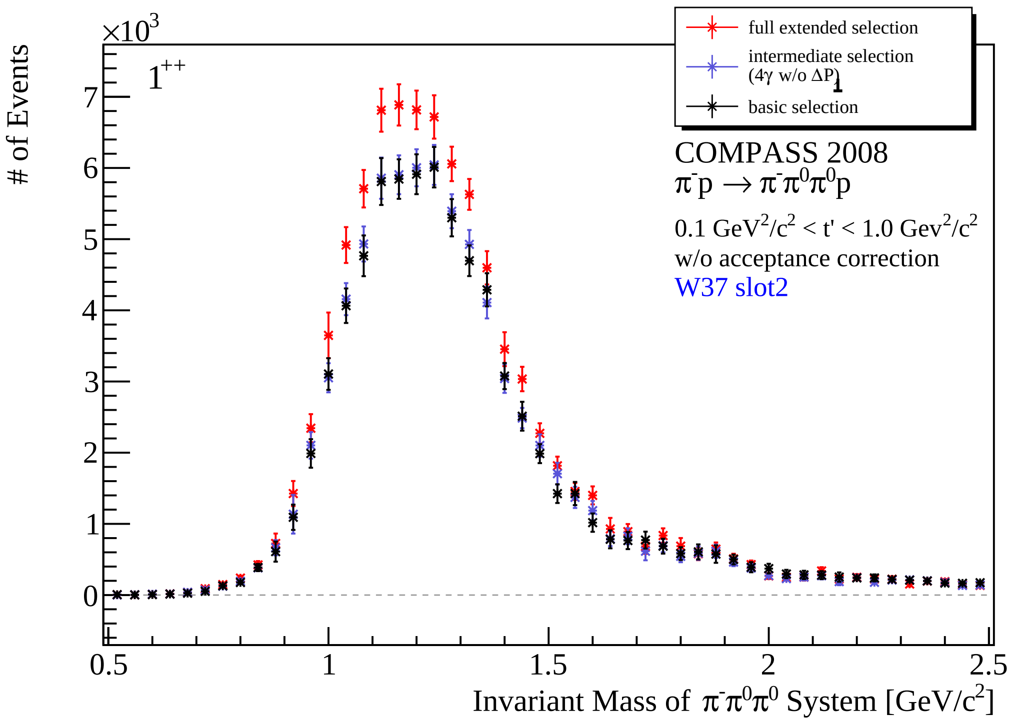

Figure 6.16: 1^{++} spin totals analog to 6.15. The intermediate selection in blue only uses events containing 4γ instead of 4-6. Additionally the $\Delta P_\perp$ filter was turned off.

Now the gain almost completely vanishes. Hence, if this filter is enabled, it will reduce the background, as shown by figure 6.6b. Therefore, the applied $\Delta P_\perp$ constraint must remove more a_2 signal and background as compared to a_1.

To see the full effect of the $\Delta P_\perp$ filter on the a_1/a_2 ratio, an additional selection has been made, in which only the $\Delta P_\perp$ filter of the full extended selection was turned off.

The result is shown in figure 6.17.

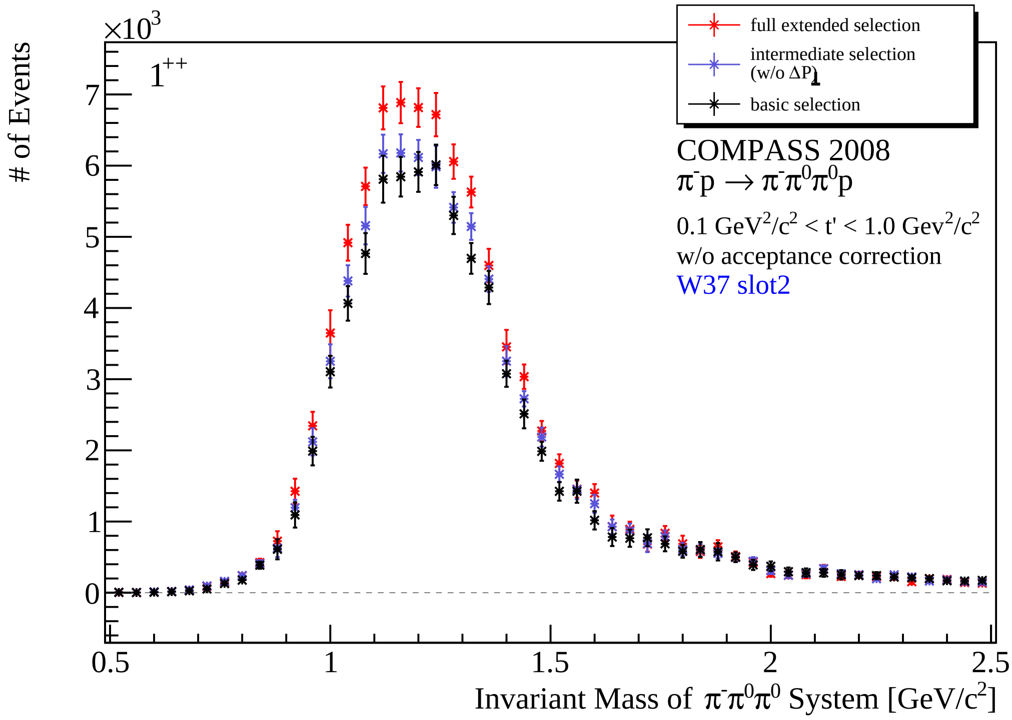

Figure 6.17: 1^{++} spin totals analog to 6.15. The intermediate selection in blue is the extended event selection withouth the $\Delta P_\perp$ filter.

To get a clear view of the magnitude of deviation, the integrals of the of the unscaled spin total waves in the a_1 and a_2 region for both the full extended selection and the intermediate selection w/o the $\Delta P_\perp$ constraint were calculated. The results are shown in table 6.2. Note integral in the a_1 region ranges from 0.85-1.65 GeV$/c^2$.

	extended selection	ext. selection w/o $\Delta P_\perp$ filter
a_1 integral $\pm$ stat. err.	102177 $\pm$ 668	109123 $\pm$ 689
a_2 integral $\pm$ stat. err.	20899 $\pm$ 225	24580 $\pm$ 315
a_1/a_2 ratio $\pm$ stat. err.	4.889 $\pm$ 0.062	4.439 $\pm$ 0.063

Table 6.2: Summary of the $a_1 a_2$ integrals and ratios for the full extended event selection and the same w/o the $\Delta P_\perp$ filter.

The amount of events removed by the $\Delta P_\perp$ filter is almost equal in absolute numbers for the a_1 and a_2 region.

Using the argumentation that the flat wave is not able to absorb the background and is preferentially absorbed by 1^{++} waves, only the opposite effect can be explained. The reason for this is the reduction of the background through the application of the $\Delta P_\perp$ filter, hence removing most of the background which was absorbed by the 1^{++} waves. Hence, the reason for this is yet unknown.

The last step towards the basic event selection is the omission of the beam-correction for the $\Delta\phi$ filter, next to the restriction to only 4γ and excluding the $\Delta P_\perp$ filter. These results are shown by the intermediate selection in figure 6.18.

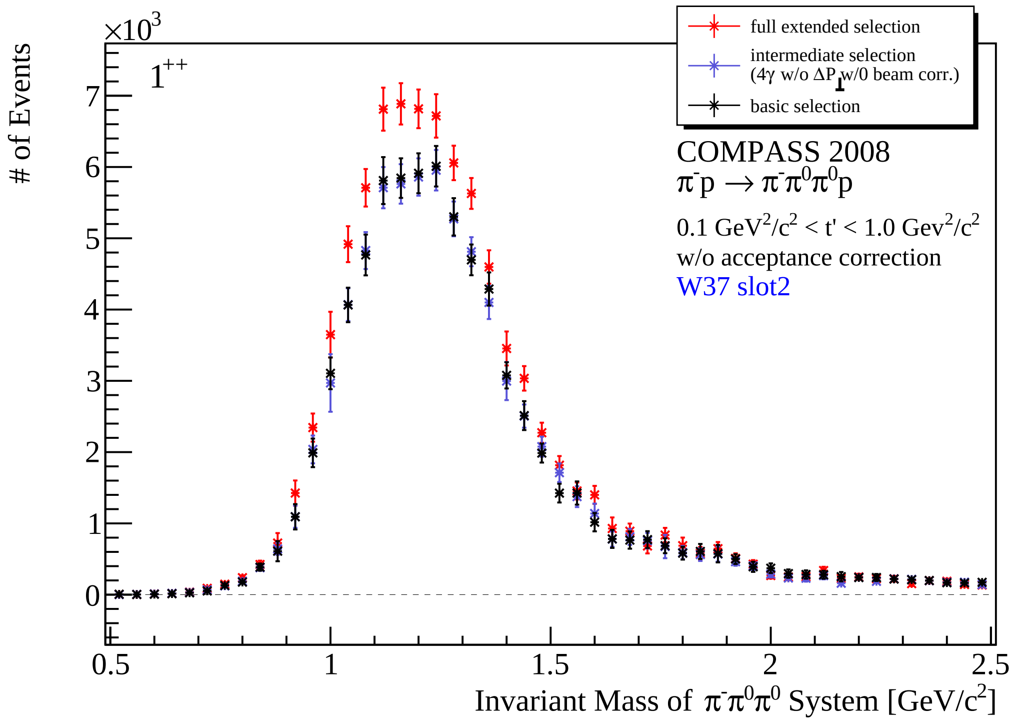

Figure 6.18: 1^{++} spin totals analog to 6.15. Here next to resorting to only 4γ events and not using the $\Delta P_\perp$ filter, no beam correction for the $\Delta\phi$ constraint was applied.

By comparing this with figure 6.16 only minor changes in the 1^{++} wave can be attributed to the beam correction introduced to the $\Delta\phi$ filter. The reason why the fit of the intermediate and basic selection are not completely identical, are the different calorimeter thresholds and the way of selecting events with the multiplicity unconstrained until the end.

Finally, table 6.3 shows the ratios for all selection and their statistical errors. Clearly the observed decrease in the ratio from the full extended selection to the basic selection cannot be explained by the statistical fluctuations.

Type of event selection	a_1/a_2 ratio $\pm$ stat. err.
extended selection	4.889 ± 0.062
basic selection	4.192 ± 0.058
ext. selection but 4γ	4.779 ± 0.065
ext. selection but 4γ, w/o $\Delta P_\perp$ filter	4.272 ± 0.062
ext. selection but 4γ, w/o $\Delta P_\perp$ filter and w/o beam corr.	4.191 ± 0.062
ext. selection w/o $\Delta P_\perp$ filter	4.439 ± 0.063

Table 6.3: Summary of the a_1/a_2 ratios for all different variations of the event selection. The a_1 integral of 0.85-1.65 GeV/c^2 and the a_2 integral of 1.1-1.5 GeV/c^2 were used for production yields.

6.3 Summary & Conclusions

First of all the way of filtering, by leaving the multiplicity unconstrained until the end and letting all of the remaining constraints decide upon best combination, is proven. Furthermore, a significant amount of exclusive $\pi^-\pi^0\pi^0$ final state events reside in the $\pi^-5\gamma$ and $\pi^-6\gamma$ events.

A new objective method for finding electromagnetic calorimeter thresholds by maximizing the π^0 significance was shown. Also the effect of the beam correction for the transversal momentum conservation filters on the was studied. By this the peaks in the respective distributions became enhanced and more narrow. Therefore this implementation should be included as more events are selected with a constant signal to background ratio.

The $\Delta P_\perp$ filter, which was included to additionally suppress background, by checking the magnitude of the transverse momentum conservation seems to distorted the a_1/a_2 ratio for a yet unknown reason. Until a detailed study upon this is made it cannot be used in selections, which should be planned for the future, as the background decreased by a factor of 50% within the extended selection.

Altogether the yield of additional events is 43% w.r.t. the basic selection and a quite similar signal to background ratio, due to the new $\Delta P_\perp$ filter was achieved. However, as mentioned above this filter cannot be used yet, and once it is left out of the selection the total amount of final selected events increases, while the signal to noise becomes worse.

Chapter 7

High Statistics Partial Wave Analysis

In this chapter an Partial Wave Analysis on a larger data set using optimizations from the extended event selection studied in chapter 6 is given.

At first the used event selection is presented in section 7.1. Here only changes to the extended event selection will be discussed briefly.

In section 7.2, the obtained fit results of the PWA from this data set are presented. Here only intensities and phases for a selected number of waves are shown. More fit results can be found in appendix C.

7.1 The Event Selection

This event selection was run on the complete data from the periods W37 and W35, using the newest software versions and reconstruction code available at the time. In contrast to the extended event selection in chapter 6, additional information provided by the new reconstruction code is used.

The overview of the complete event selection is shown in Table 7.1. Comparing the number of final selected events with the 277 405 final events of the extended event selection in chapter 6, the statistics gain by a factor of 10 is clarified. The differences and improvements are discussed below in more detail.

Applied cut	# of events (extended)
1 primary vertex	NA
1 outgoing track	NA
chargesum cut	NA
$2 \leq \#$ neutral clusters	NA
all preselected events	$7.77083 \cdot 10^8$
real target cut	$4.84467 \cdot 10^8$
$4 \leq N_\gamma \leq 6$	$8.69938 \cdot 10^7$
$E_{\pi^-} < 185.00\,\mathrm{GeV}$	$6.33962 \cdot 10^7$
$\lvert M_{\pi^0} - 134.98\,\mathrm{MeV}/c^2\rvert < 22\,\mathrm{MeV}/c^2$	$1.75930 \cdot 10^7$
$N_{\text{proton}} = 1$ & $\lvert p_{\text{proton}}\rvert > 250\,\mathrm{MeV}/c$	$1.28287 \cdot 10^7$
kaon veto: kaon prob. ≥ 0.8	$1.27317 \cdot 10^7$
$\lvert\Delta\phi\rvert < 0.21\,\mathrm{rad}$	$6.58266 \cdot 10^6$
$0.10\,(\mathrm{GeV}/c)^2 < t' < 1.00\,(\mathrm{GeV}/c)^2$	$5.22148 \cdot 10^6$
$\lvert M_{\pi^0} - 134.98\,\mathrm{MeV}/c^2\rvert < 17\,\mathrm{MeV}/c^2$	$4.24414 \cdot 10^6$
$\lvert E_{\text{beam}} - 191.65\,\mathrm{GeV}\rvert < 6.20\,\mathrm{GeV}$	$2.70450 \cdot 10^6$
multiplicity = 1	$2.66799 \cdot 10^6$

Table 7.1: Summary of the full event selection. Note that the number of gamma cut (N_γ) includes energy scaling and thresholding for the individual calorimeters and a cluster time cut.

In general for the obtained distributions the explicit cut parameters were obtained by a Gaussian-fit accepting events within 2σ of the mean value. Unfortunately the DT0 was not applied, as shown in table 7.1. However, as it is the primary trigger and the other triggers are damped by the requirement of a recoil proton and a pion beam, this effect is negligible.

Note from table 7.1 that the $\Delta P_\perp$ filter of the extended event selection was omitted in this selection, on the basis of the generated artefacts, which are not yet understood.

Tighter Target Cut:

The first change to the extended event selection is a stricter target cut in the xy-projection. The xy-distribution of primary vertices in shown in figure 7.1.

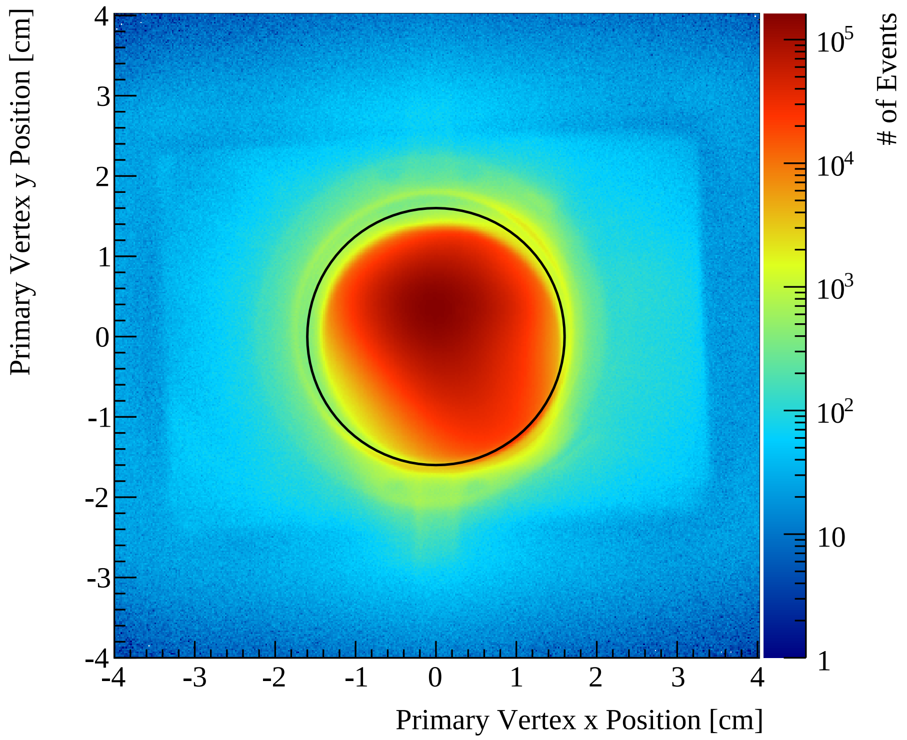

Figure 7.1: xy-distribution of primary vertices. The black circle indicates the applied cut.

The cut was reduced to a radius of $\sqrt{\mathrm{PV}_x^2 + \mathrm{PV}_y^2} < 1.60\,\mathrm{cm}$, because the original cut of 1.75 cm was cutting into the containment of the liquid hydrogen target on the bottom right. This can be seen from figure 4.2a. The primary vertex z-position cut is identical to the other event selections with $-68.4\,\mathrm{cm} < \mathrm{PV}_z < -28.4\,\mathrm{cm}$.

ECAL Cluster Selection:

Just as for the other selection at first all neutral clusters are selected. Then gamma energies were scaled by a factor of $\mathrm{m}_{\pi^0}^{\mathrm{PDG}}/0.1375$ for ECAL1 and $\mathrm{m}_{\pi^0}^{\mathrm{PDG}}/0.1367$ for ECAL2 in order to center the π^0 mass at the PDG value. At this point the calorimeter thresholds of 0.3 and 1.9 are applied. They were determined by the method developed in appendix B.

An additional feature of the this reconstruction software version are the time informations of the ECAL clusters. This is very useful for removal of noise in the calorimeters, which is randomly distributed in time. The distribution of cluster times for both ECALs is shown in figure 7.2.

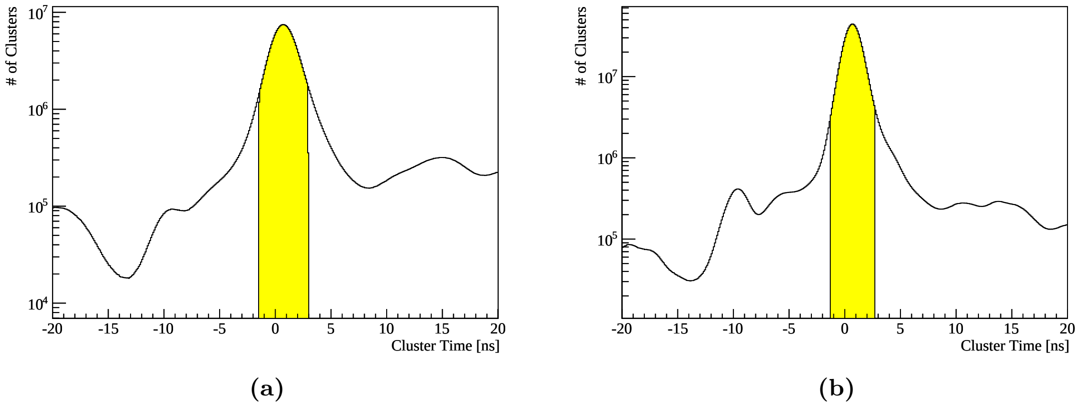

Figure 7.2: Neutral cluster times for ECAL1 in (a) and ECAL2 in (b) displayed in log scale. The filled yellow areas indicate the applied 2σ cut.

Applying these cuts one expects to reduce the amount events with more than 4 neutral clusters w.r.t. the case of exactly 4 clusters. The neutral cluster distribution is shown in figure 7.3. Comparing this with figure 4.3, one can see that the relative difference between the amount of 4 and 5/6 neutral clusters per event increases for the selection using the time cut.

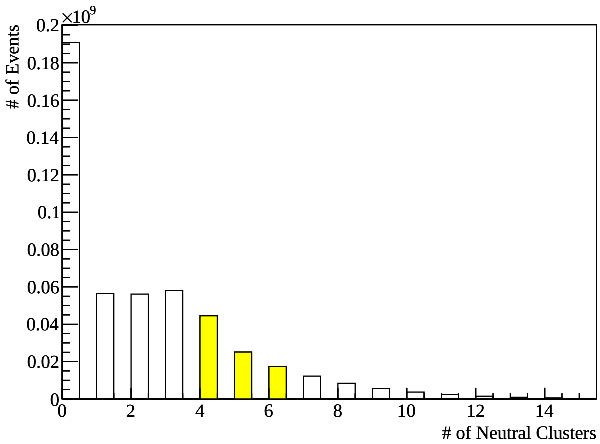

Figure 7.3: Number of neutral clusters per event before the gamma count cut. The values highlighted in yellow are selected (4-6).

Comparison of π^0 Mass Significances and Exclusivities:

For a better comparison of the different gamma counts, again the π^0 yields can be regarded. Therefore additional selections have been performed not restricting the π^0 mass, and the final π^0 mass distributions are shown in figure 7.4a. Note that the multiplicity is not constrained at this point.

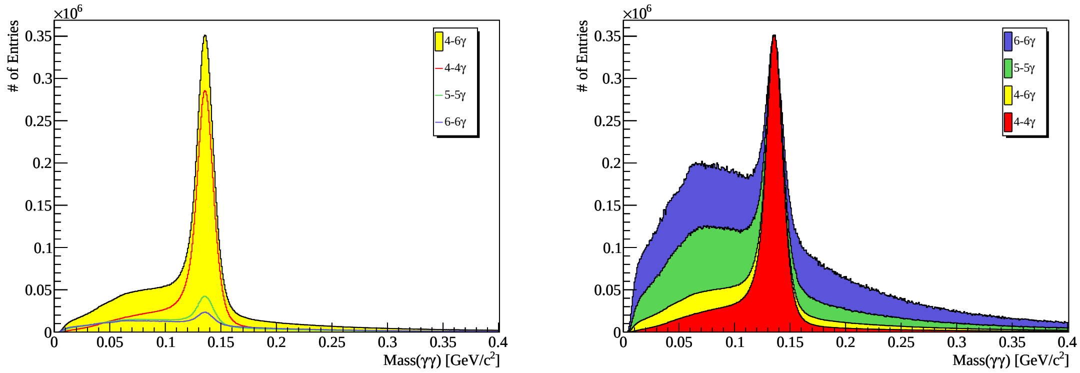

(a) **(b)**

Figure 7.4: (a): One-dimensional mass distributions for different gamma counts after all cuts except the multiplicity. Of course no restriction on the π^0 mass have been made. The red curve corresponds to 4γ events and exhibits the smallest background relative to the signal. In green, blue and yellow the 5γ, 6γ and 4-6γ selections are shown, respectively. For each combination consisting of two γ pairs, both the π^0 masses enter the histogram. Every event may possess more than one combination. **(b):** Same as in (a), however, here all curves have been scaled to the 4-6γ graph (yellow).

Comparing this with figure 7.4, the differences of the new reconstruction code using the cluster time cuts becomes apparent. Here both the distributions using the five and six gamma count decrease by a noticeable amount.

Similar to chapter 6, the multiplicities shadow the absolute yields and therefore do not allow a direct comparison. Since the π^0 mass cut is the only sensitive to the intrinsic combinatorics, an application of the same and regarding the exclusivity distribution, reduces the distortion cause by the multiplicities to a minimum. The exclusivity distributions for the various gamma counts is shown in figure 7.5a.

At this point, the small contributions of the 5 and 6 gamma counts becomes evident. As the restriction on 4-6γ arise from the extended selection, that was performed on older reconstruction code in which the cluster times are not available, a selection only taking into account the 5γ case should be regarded.

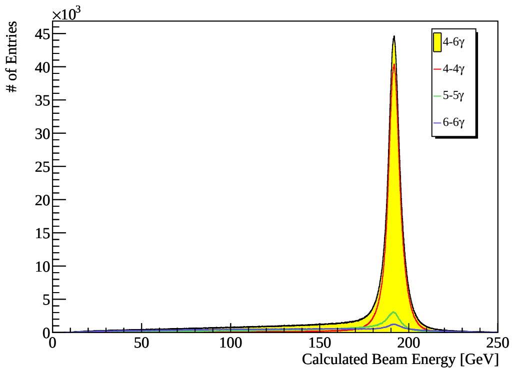

(a) Exclusivity peaks for different gamma counts. The 4γ case is shown in red, 5γ in green, 6γ in blue and 4-6γ in yellow.

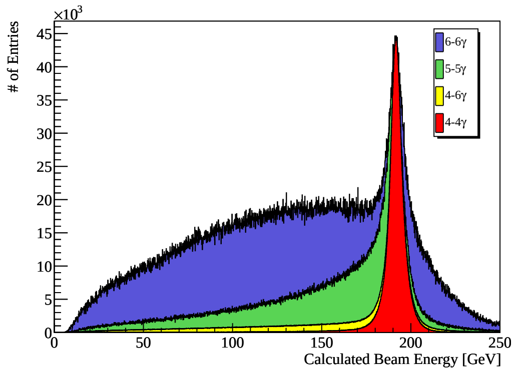

(b) Exclusivity peaks for different gamma counts, while all distributions have been scaled to the yellow curve which represents the 4-6 γ case, naturally being the strongest distribution. The coloring scheme is identical to (a).

Figure 7.5

Multiplicity:

The final multiplicities are shown in figure 7.6. Here higher multiplicities are suppressed by at least two order of magnitude.

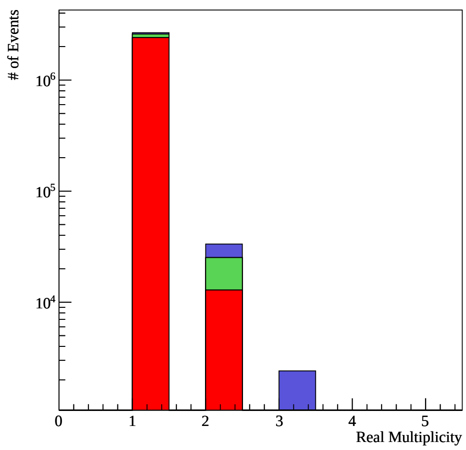

Figure 7.6: Final multiplicities in log scale, before the cut on the same has been made. The blue, green and red part of the histogram correspond to the 4, 5 and 6 gamma contributions, respectively.

3π Invariant Mass & Dalitz Plots:

Finally the 3π invariant mass spectrum reveals the major produced states as shown in figure 7.7. Similar to spectra of the other events selections the dominant $a_1(1260)$, $a_2(1320)$, and $\pi_2(1670)$ can be seen.

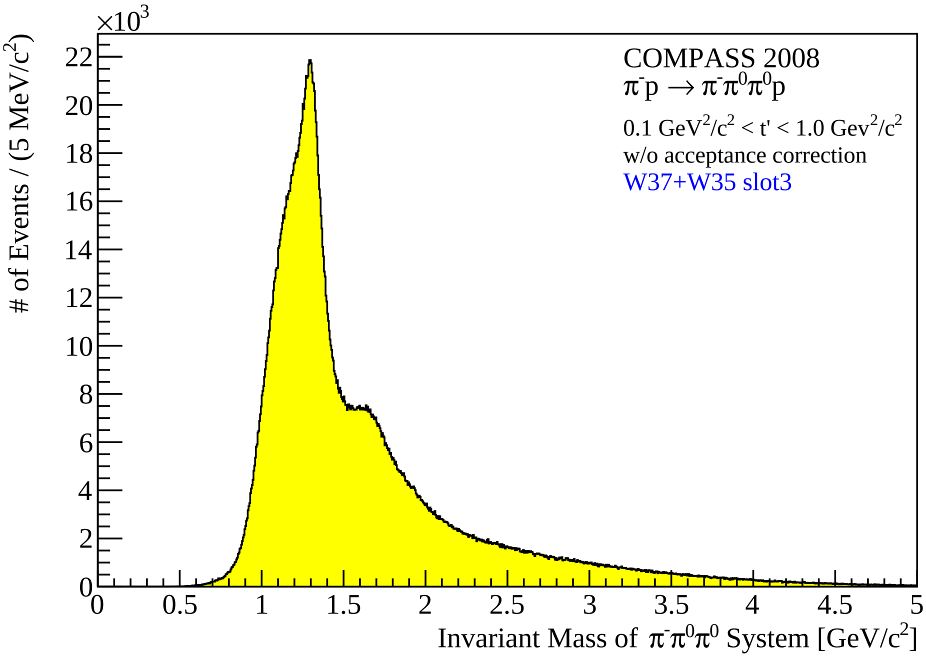

Figure 7.7: 3π invariant mass spectrum after all cuts.

Before moving on to the PWA results, the Dalitz plots reveal some of the isobar decays that actually occur for the created states. This is shown in figure 7.8 for the $a_1(1260)$ region.

Here the squared invariant mass of a randomly chosen π^0 and the π^- is plotted against the squared invariant mass of the π^0 pair. The remaining $\pi^-\pi^0$ mass combination is fixed by the other two and are constant along lines at $45\,°$. In case the a_2 state would be a 3 body phase space decay the Dalitz plot will not show any correlations. However, one observes a vertical band at around $0.6\,\mathrm{GeV}^2/\mathrm{c}^4$, that corresponds to a negatively charged $\rho(770)$ intermediate state, decaying into the $\pi^0\pi^-$ pair. The source of the diagonal band is also the ρ intermediate state.

Similar statements can be made for the Dalitz plot in the $a_2(1320)$ region, which is shown in figure 7.9.

However, for the case of the $\pi_2(1670)$, shown in figure 7.10, an additional band at the squared $\pi^0\pi^0$ mass of $1.6\,(\mathrm{GeV}/c^2)^2$ is visible. This corresponds to the neutral $f_2(1270)$ isobar state, which is also used for partial waves with the 2^{-+} quantum numbers of the π^2 state shown by table 7.2.

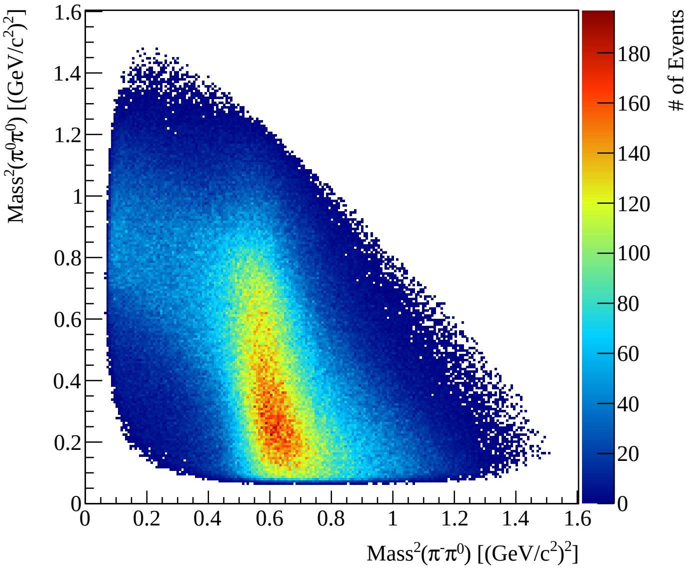

Figure 7.8: Dalitz plot in a_1 region, meaning events with an invariant mass of 1260 MeV $\pm$ 100 MeV were allowed.

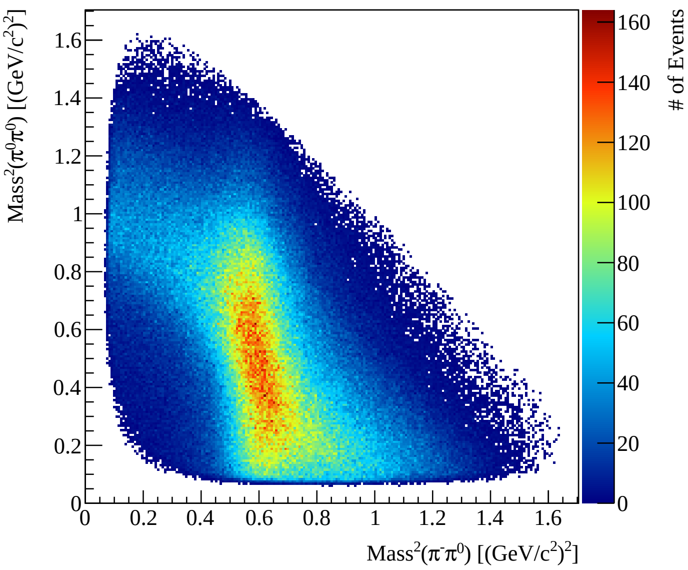

Figure 7.9: Dalitz plot in a_2 region, meaning events with an invariant mass of 1320 MeV $\pm$ 100 MeV were allowed.

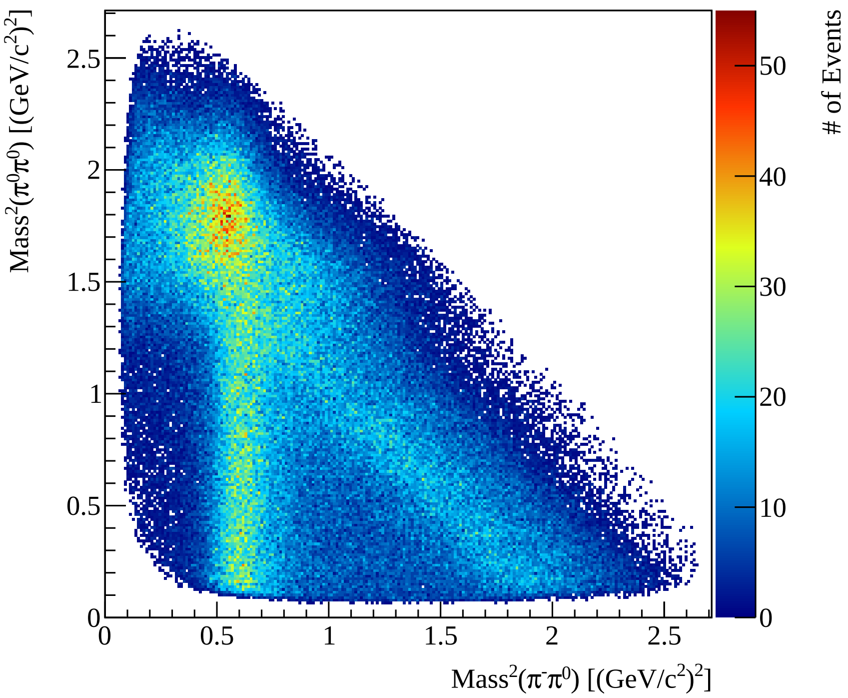

Figure 7.10: Dalitz plot in π_2 region, meaning events with an invariant mass of 1670 MeV ± 100 MeV were allowed.

7.2 PWA results

A mass independent fit was performed using the rootPWA framework svn revision 633(trunk). For this the data was divided into 50 3π invariant mass bins of $40\,\mathrm{MeV}/c^2$ width, ranging from $[0.5, 2.5]\,\mathrm{GeV}/c^2$. Thereof the number of final selected events is reduced to **2 394 916**. The waveset used in chapter 5 was extended to a total count of 53 waves, as shown in table 7.2. The normalization integrals were calculated by phase space MC, counting twice as many events as real data for each mass bin. For lower mass bins a minimum number of 10 000 phase space MC was used. Each mass bin was fitted only once. Note that the fit results are not acceptance corrected and therefore the results have to be regarded with caution. More fit results can be found in appendix C.

1^{++} :
At first waves with the J^{PC} quantum numbers of 1^{++} are regarded. Figure 7.11 shows the production intensities for two selected waves. At approximately $1.2\,\mathrm{GeV}/c^2$ the well established $a_1(1260)$ resonance can be seen, which is dominantly produced with an maximum intensity of 80 000 in the central bins. Also notice the small dip at a 3π invariant mass of $1.3\,\mathrm{GeV}/c^2$.

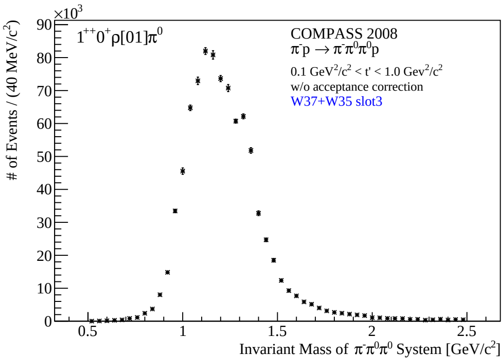

(a) Intensity of $1^-1^{++}0^+\rho(770)[01]\pi^0$ wave.

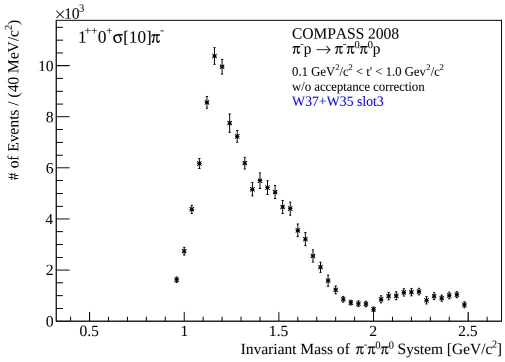

(b) Intensity of $1^-1^{++}0^+\sigma[10]\pi^-$ wave.

Figure 7.11

2^{++} :
The intensity for a selected 2^{++} wave is shown in figure 7.12a. Here an extremely well defined peak can be seen at an invariant mass of $1.3\,\mathrm{GeV}/c^2$. This corresponds to the $a_2(1320)$ resonance which is also well established. Now that two waves with different J^{PC} quantum numbers are at hand, their relative phase angle can be studied, as shown in figure 7.12b. In the invariant mass range of $1.0\,\mathrm{GeV}/c^2$ to $1.2\,\mathrm{GeV}/c^2$, the falling slope shows the resonating behaviour of the $a_1(1260)$. Above this mass, a rising phase motion can be observed, which is expected due to the $a_2(1260)$ resonance.

$J^{PC}M^{\epsilon}$	Isobar	L	S	Bachelor π	Threshold (GeV/c^2)
$0^{-+}0^{+}$	$\rho(770)$	1	1	π^0	-
$0^{-+}0^{+}$	$\sigma/f_0(600)$	0	0	π^-	-
$0^{-+}0^{+}$	$f_0(980)$	0	0	π^-	1.25
$0^{-+}0^{+}$	$f_2(1270)$	2	2	π^-	1.40
$0^{-+}0^{+}$	$f_0(1500)$	0	0	π^-	1.60
$1^{++}0^{+}$	$\rho(770)$	0	1	π^0	-
$1^{++}0^{+}$	$\rho(770)$	2	1	π^0	1.30
$1^{++}1^{+}$	$\rho(770)$	0	1	π^0	-
$1^{++}0^{+}$	$\sigma/f_0(600)$	1	0	π^-	0.94
$1^{++}0^{+}$	$/f_0(980)$	1	0	π^-	1.20
$1^{++}0^{+}$	$f_2(1270)$	1	2	π^-	1.20
$1^{++}1^{+}$	$\rho(770)$	2	1	π^0	1.40
$1^{++}1^{+}$	$\sigma/f_0(600)$	1	0	π^-	1.20
$1^{++}1^{+}$	$f_2(1270)$	1	2	π^-	1.40
$1^{-+}1^{+}$	$\rho(770)$	1	1	π^0	-
$1^{-+}1^{+}$	$f_2(1270)$	2	2	π^-	1500
$2^{++}1^{+}$	$\rho(770)$	2	1	π^0	-
$2^{++}1^{+}$	$f_2(1270)$	1	2	π^-	1.20
$2^{++}2^{+}$	$\rho(770)$	2	1	π^0	1.10
$2^{-+}0^{+}$	$\rho(770)$	1	1	π^0	0.80
$2^{-+}0^{+}$	$\rho(770)$	3	1	π^0	1.20
$2^{-+}0^{+}$	$\rho_3(1690)$	1	3	π^0	1.70
$2^{-+}0^{+}$	$\sigma/f_0(600)$	2	0	π^-	0.80
$2^{-+}0^{+}$	$f_0(980)$	2	0	π^-	1.40
$2^{-+}0^{+}$	$f_2(1270)$	0	2	π^-	1.20
$2^{-+}0^{+}$	$f_2(1270)$	2	2	π^-	1.50
$2^{-+}1^{+}$	$\rho(770)$	1	1	π^0	0.80
$2^{-+}1^{+}$	$\rho(770)$	3	1	π^0	1.20
$2^{-+}1^{+}$	$\sigma/f_0(600)$	2	0	π^-	1.20
$2^{-+}1^{+}$	$f_2(1270)$	0	2	π^-	1.20
$2^{-+}1^{+}$	$f_2(1270)$	2	2	π^-	1.50
$2^{-+}2^{+}$	$f_2(1270)$	0	2	π^-	1.50
$3^{++}0^{+}$	$\rho(770)$	2	1	π^0	1.20
$3^{++}0^{+}$	$\rho_3(1270)$	0	3	π^0	1.76
$3^{++}0^{+}$	$\sigma/f_0(600)$	3	0	π^-	1.25
$3^{++}0^{+}$	$f_2(1270)$	1	2	π^-	1.20
$3^{++}1^{+}$	$\rho(770)$	2	1	π^0	1.50
$3^{++}1^{+}$	$\rho_3(1270)$	0	3	π^0	1.76
$3^{++}1^{+}$	$f_2(1270)$	1	2	π^-	1.20
$4^{-+}0^{+}$	$\rho(770)$	3	1	π^0	1.00
$4^{-+}1^{+}$	$\rho(770)$	3	1	π^0	1.20
$4^{++}1^{+}$	$\rho(770)$	4	1	π^0	1.40
$4^{++}1^{+}$	$f_2(1270)$	3	2	π^-	1.60
$5^{++}0^{+}$	$\rho(770)$	4	1	π^0	1.25
$6^{-+}0^{+}$	$\rho(770)$	5	1	π^0	1.25
$1^{++}1^{-}$	$\rho(770)$	0	1	π^0	-
$1^{-+}0^{-}$	$\rho(770)$	1	1	π^0	-
$1^{-+}1^{-}$	$\rho(770)$	1	1	π^0	-
$2^{++}0^{-}$	$\rho(770)$	2	1	π^0	-
$2^{++}0^{-}$	$f_2(1270)$	1	2	π^-	1.30
$2^{++}1^{-}$	$f_2(1270)$	1	2	π^-	1.30
$2^{-+}1^{-}$	$f_2(1270)$	0	2	π^-	1.20
FLAT	-	-	-	-	

Table 7.2: The used 53 waveset.

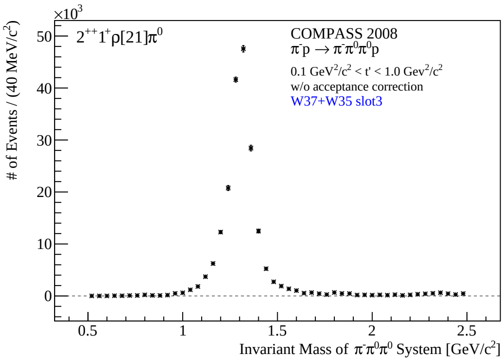

(a) Intensity of $1^{-}2^{++}1^{+}\rho(770)[21]\pi^{0}$ wave.

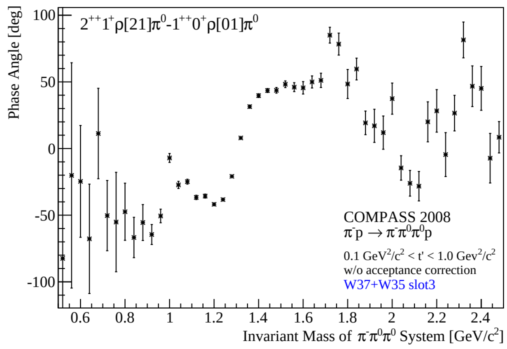

(b) Relative phase angle between the $1^{-}2^{++}1^{+}\rho(770)[21]\pi^{0}$ and $1^{-}1^{++}0^{+}\rho(770)[01]\pi^{0}$ wave.

Figure 7.12

2^{-+} :

Also the 2^{-+} waves exhibit quite strong intensities, as shown in figure 7.13a for a selected wave. One can nicely see a peak at an invariant mass of 1.7 GeV$/c^2$, which is the $\pi_2(1670)$ resonance. The relative phase with the reference $1^{-}1^{++}0^{+}\rho(770)[01]\pi^{0}$ wave nicely shows the rising phase motion of the π_2, emphasizing the resonant behaviour.

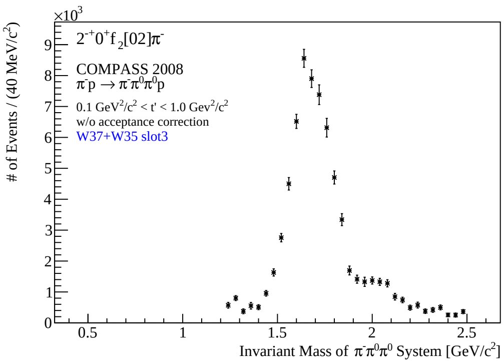

(a) Intensity of $1^{-}2^{-+}0^{+}f_2(1270)[02]\pi^{-}$ wave.

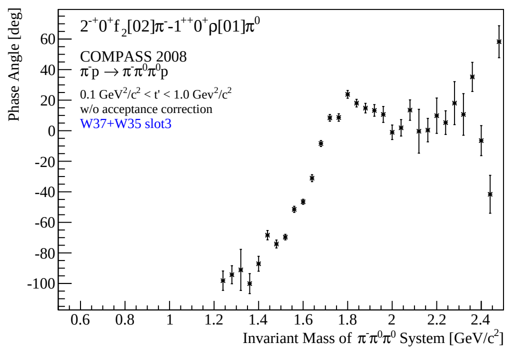

(b) Relative phase angle between the $1^{-}2^{-+}0^{+}f_2(1270)[02]\pi^{-}$ and $1^{-}1^{++}0^{+}\rho(770)[01]\pi^{0}$ wave.

Figure 7.13

1^{-+} :

The intensity for a selected 1^{-+} wave shown in figure 7.14a. Here only a peak structure at a mass of 1.4 GeV$/c^2$ can be seen. The $\pi_1(1600)$ state observed by other experiments obviously heavier and cannot explain this structure. In particular the relative phase with the reference $1^-1^{++}0^+\rho(770)[01]\pi^0$ wave shows no rising phase motion at this mass, but at the mass of the π_1 state. Apart from this, the expected falling phase motion at the mass of the a_1 resonance is seen. Another rising phase at the high mass of $2.2\,\mathrm{GeV}/c^2$ is revealed, however, as the intensity is extremely low at this point no physical state can be declared.

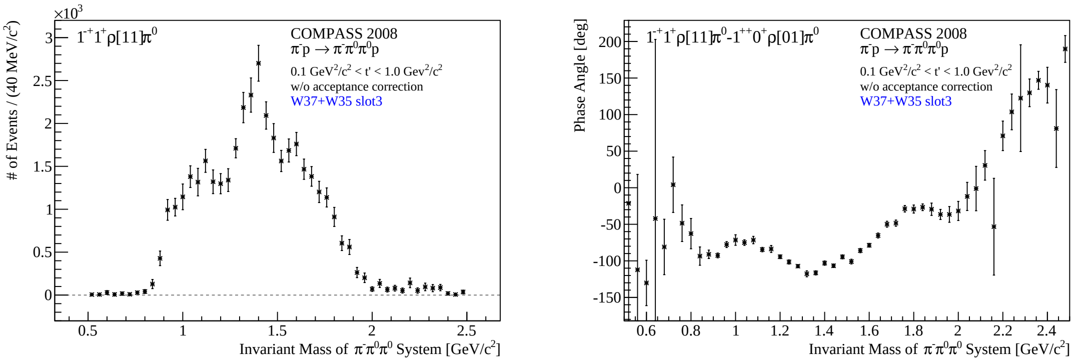

(a) Intensity of $1^-1^{-+}1^+\rho(770)[11]\pi^0$ wave.

(b) Relative phase angle between the $1^-1^{-+}1^+\rho(770)[11]\pi^0$ and $1^-1^{++}0^+\rho(770)[01]\pi^0$ wave.

Figure 7.14

0^{-+} :

Additional resonant behaviour can be observed in waves with 0^{-+} quantum numbers, as shown in figure 7.15. Here both the intensity and the relative phase with the $1^-1^{++}0^+\rho(770)[01]\pi^0$, exhibit a clear resonant peak at a 3π invariant mass of $1.8\,\mathrm{GeV}/c^2$, which corresponds to the $\pi(1800)$.

4^{++} :

The last unambiguous observation of a resonance can be made in 4^{++} waves. From figure 7.16a, showing the intensity of the $1^-4^{++}1^+\rho(770)[41]\pi^0$ wave, nicely peaks at a mass of about $2.0\,\mathrm{GeV}/c^2$. This corresponds to the $a_4(2040)$ state as listed by the PDG, and the relative phase angle with the $1^-1^{++}0^+\rho(770)[01]\pi^0$ nicely exhibits a rising phase motion at this mass, verifying this resonance.

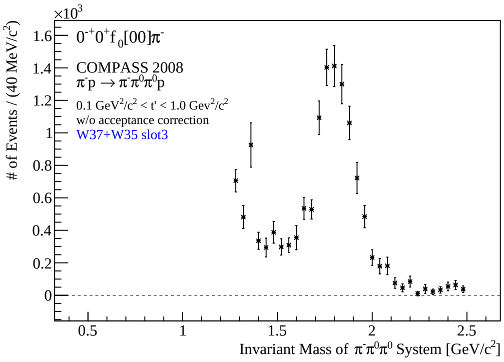

(a) Intensity of $1^-0^{-+}0^+ f_0(980)[00]\pi^-$ wave.

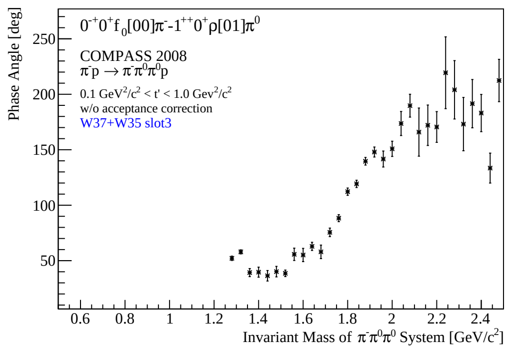

(b) Relative phase angle between the $1^-0^{-+}0^+ f_0(980)[00]\pi^-$ and $1^-1^{++}0^+\rho(770)[01]\pi^0$ wave.

Figure 7.15

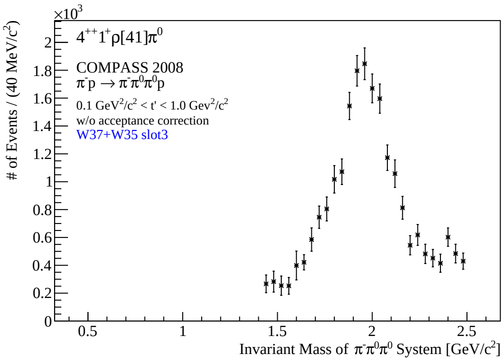

(a) Intensity of $1^-4^{++}1^+\rho(770)[41]\pi^0$ wave.

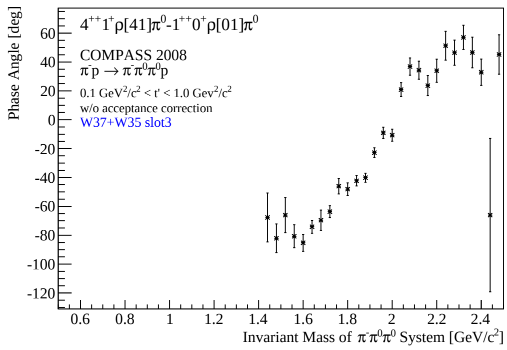

(b) Relative phase angle between the $1^-4^{++}1^+\rho(770)[41]\pi^0$ and $1^-1^{++}0^+\rho(770)[01]\pi^0$ wave.

Figure 7.16

Appendix A

Dependence of Fit Result on Starting Parameters

The dependence of the fit on the different starting parameter values will be described here on the basis of the $1^-2^{++}1^+\rho(770)[21]\pi^0$ wave shown in figure 5.1 and the exotic $1^-1^{-+}1^+\rho(770)[11]\pi^0$ wave displayed in figure 5.4.

In the mass-independent fit the mass bins are completely independent. For each mass bin 600 fits with different starting parameters were carried out, resulting in separate distribution of intensities. For the invariant mass bin $[1300, 1340]\,\mathrm{MeV}/c^2$ the distribution of the intensities of the 2^{++} wave is depicted in figure A.1a. This bin was chosen to illustrate the dependence in the $a_1(1260)/a_2(1320)$ region.

Obviously the cyan bands shown in section 5.2, calculated from the maximum and minimum intensity of the distribution, is not able to described the errors quantitatively. Because of the complex distribution of intensities, this simple estimation was chosen to qualitatively illustrate the magnitude of start parameter dependence. From figure A.1a it is obvious that not all values within the start parameter dependence band are reached by certain fit attempts, but the fit results cluster at certain regions of intensity, most likely corresponding to local log likelihood minima.

These intensity distributions are expected from a manifold offering a vast number of different local maxima, due to the clustering of fits results at certain intensities. From the high dimensionality of the log likelihood manifold, it is difficult to measure the structure of the manifold and no further statements can be made.

Similar distribution of fit result intensities can be seen in higher invariant mass bins, shown in figure A.1b for the selected mass bin of $[1740, 1780]\,\mathrm{MeV}/c^2$. Note that here the relative deviations are here in the order of $100\,\%$ as compared to the $3\,\%$ in the dominant a_1/a_2 region.

It is interesting to see the distribution of log likelihood values for these invariant mass bins, to gain insight on the dependence of intensity changes on deviations of the log likelihood. These distributions are shown in figure A.3 for the two selected invariant mass bins. As the log likelihood is only able to distinguish the goodness of fit relative to other results without a measure of the actual agreement with the real data, there is no universal scale for differences of the log likelihood. Nevertheless, on the basis of figure A.3 the deviations of the shown intensity distributions are generated by fluctuations of $10 - 100$ units in the log likelihood. Note that the relative variations are below $0.1\,\%$.

For the two chosen mass bins, the intensity distributions for the 1^{-+} wave are shown in figure A.2. The structure of distributions is similar, and the values will accumulate around these values. The main difference are the relative errors of the intensity clusters, that correspond to the individual likelihoods. Hence very small chances in the log likelihood generate large variations in the intensities.

As a conclusion, the fit can depend heavily on the starting parameters, and to eliminate this factor, the number of independent fits has to be as large as possible.

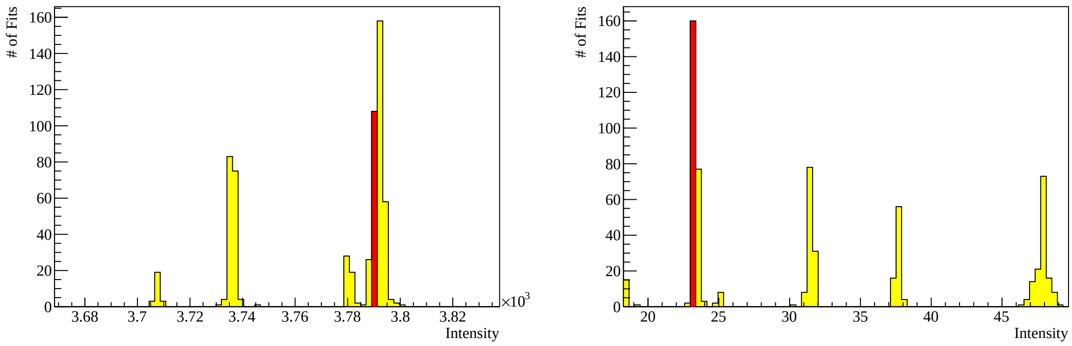

(a) Fit intensity distribution for the 1320 MeV/c^2 mass bin.

(b) Fit intensity distribution for the 1760 MeV/c^2 mass bin.

Figure A.1: Intensity distributions of two chosen mass bins for the $1^-2^{++}1^+\rho(770)[21]\pi^0$ wave. The highlighted intensity in red indicate the fits with the maximum log likelihood of the 600 performed fits.

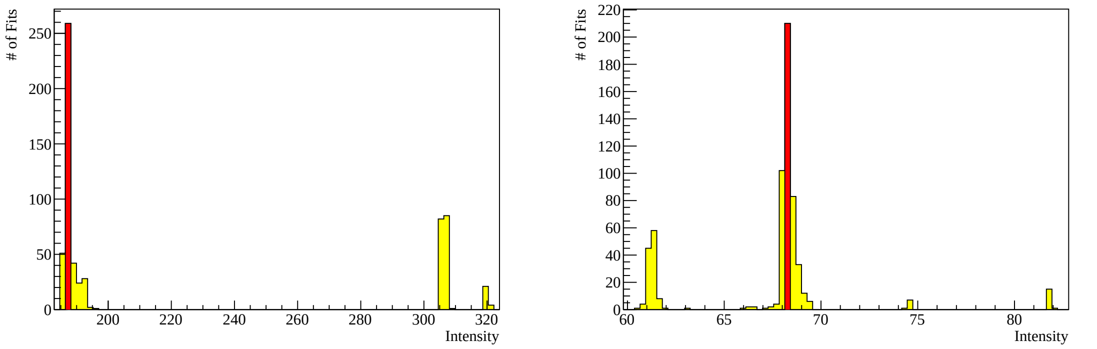

(a) Fit intensity distribution for the 1320 MeV/c^2 mass bin.

(b) Fit intensity distribution for the 1760 MeV/c^2 mass bin.

Figure A.2: Intensity distributions of two chosen mass bins for the $1^-1^{-+}1^+\rho(770)[11]\pi^0$ wave. The highlighted intensity in red indicate the fits with the maximum log likelihood of the 600 performed fits.

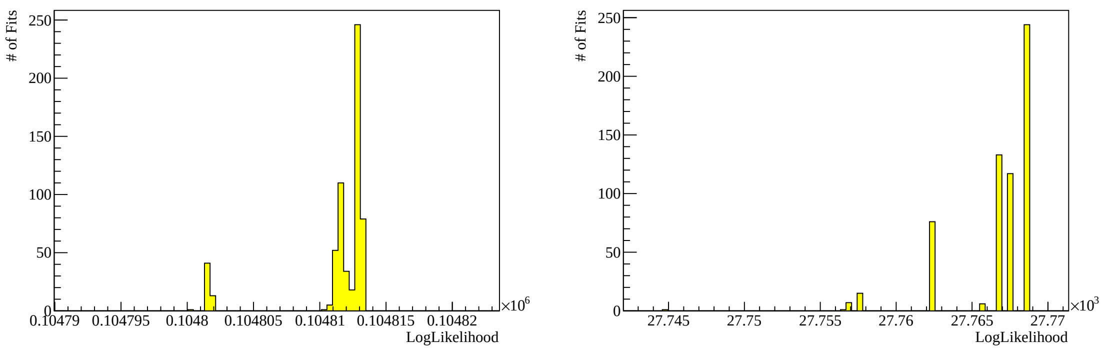

(a) Fit intensity distribution for the 1320 MeV/c^2 mass bin.

(b) Fit intensity distribution for the 1760 MeV/c^2 mass bin.

Figure A.3: Log likelihood distribution for the 3π invariant mass bin of 1320 MeV/c^2 in (a) and 1760 MeV/c^2 in (b).

Appendix B

Electromagnetic Calorimeter Thresholding

The procedure for the determination of the ECAL energy thresholds, used in the extended event selection, is described here. The reason to study this, were the extremely low thresholds of 0.25 GeV and 1.0 GeV for ECAL1 and ECAL2 used in [25]. For comparison the hardware thresholds of the calorimeters are about 0.20 GeV and 1.0 GeV, respectively. Instead of subjectively choosing new higher thresholds, a method for their quantitative calculation was developed.

The goal is to find ECAL thresholds that optimize the signal to background ratio of the π^0 signal, as higher thresholds remove more of the low energetic calorimeter noise. However, one cannot set the threshold arbitrarily high, because the signal loses intensity, so that an intermediate threshold is the right choice. In order to find the "best" threshold, a figure of merit is needed. Here the π^0 significance was used, which is defined in the following way.

$$\text{Significance} = \frac{\text{Signal}_{\pi^0}}{\sqrt{\text{Signal}_{\pi^0} + \text{Background}}} \tag{B.1}$$

In which Signal_{π^0} corresponds to the number of events below the background-subtracted π^0 peak.

Hence the goal is to create one-dimensional π^0 mass distributions for different ECAL energy thresholds and determine their significance, respectively. The optimal threshold is the given by the point of highest significance.

Figure B.1 shows the π^0 mass versus the energy threshold for both calorimeters.

Here x-projections of single y-axis bins correspond to the π^0 mass distributions for an energy threshold defined by the lower edge of the y-bin. A bin width of 50 MeV was chosen for the threshold energy. Then each 50 MeV wide slice of this histogram was fitted by a Gaussian on top of a 3rd order polynomial in the mass range of $[50, 200]\,\text{MeV}/c^2$. For both ECAL's an exemplary mass bin projection including the fit functions is shown in figure B.2.

An integral ranging from $134.98 \pm 20\,\text{MeV}/c^2$ was calculated for both the Gaussian and the background polynomial, which correspond to the signal and background values used for the significance. Then one obtains the significance as a function of the threshold for the individual calorimeters. This is depicted in figure B.3. The hardware thresholds of the calorimeters as noted above, are responsible for the constant significance at lower threshold energies.

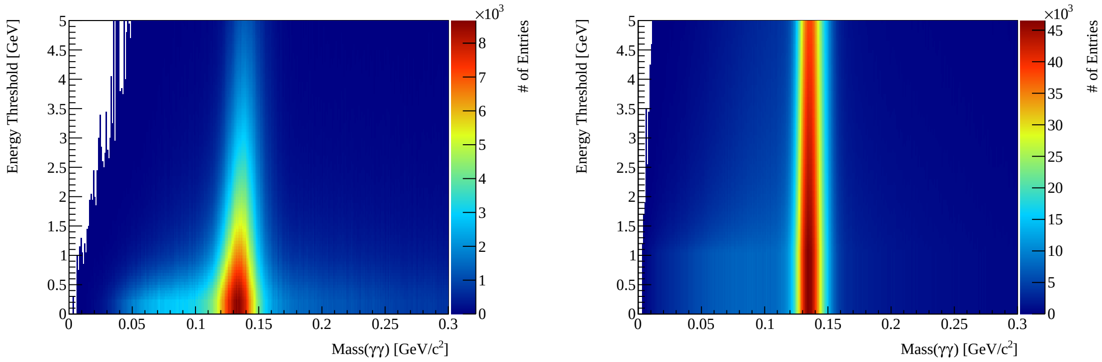

Figure B.1: π^0 mass distributions for different calorimeter energy thresholds. On the x-axis the invariant mass of the gamma pairs is displayed. The y-axis shows the energy threshold. All possible $\gamma\gamma$ combinations enter these plots, as long as both γ's were measured in the same calorimeter. Left: ECAL1. Right: ECAL2.

For the determination of the significance maximum, the curves in figure B.3 can in principle be fitted by a polynomial and then the maximum of this function can be calculated. However, as the thresholds are not needed to such a precision, only the individual points were compared. This resulted in the optimal thresholds of 0.9 GeV for ECAL1 and 2.1 GeV for ECAL2.

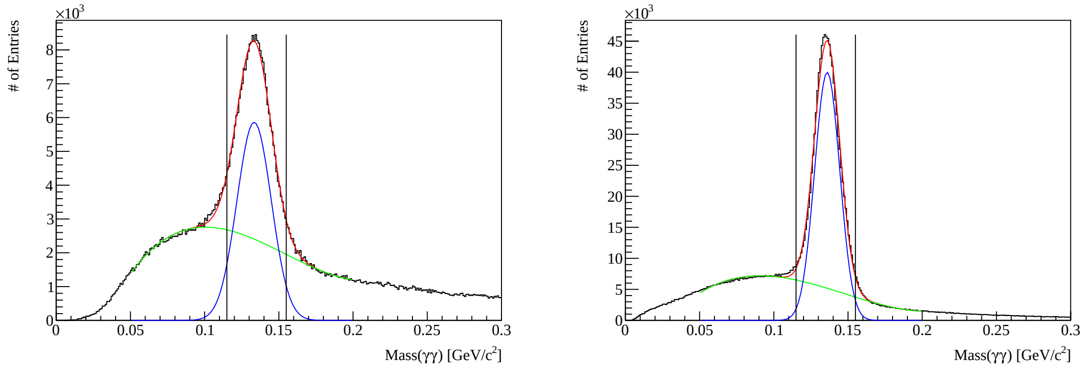

Figure B.2: π^0 mass distributions, on the left for ECAL1 with a threshold of 300 MeV and on the right for ECAL2 with a threshold of 1200 MeV. The red curve is the fitted Gaussian plus a 3rd order polynomial. The individual gaussian and polynomial parts are shown in blue and green, respectively. The two vertical black lines indicate the used integration interval.

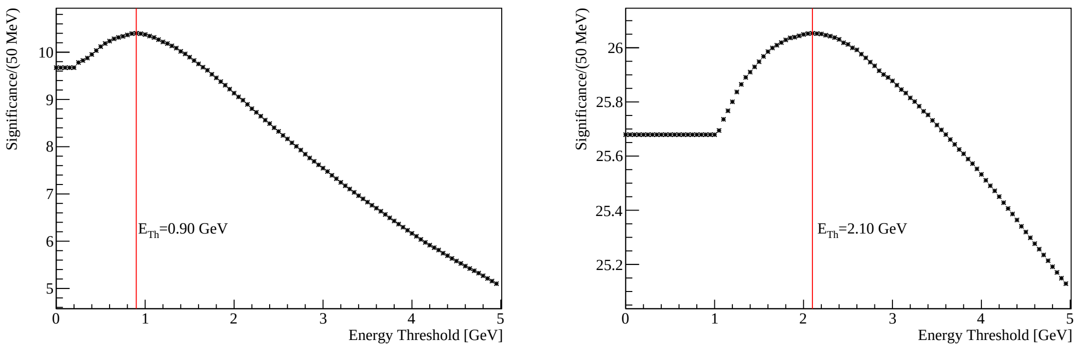

Figure B.3: π^0 significance as a function of the calorimeter energy threshold. Left: ECAL1. Right: ECAL2.

Appendix C

Additional Fit Results

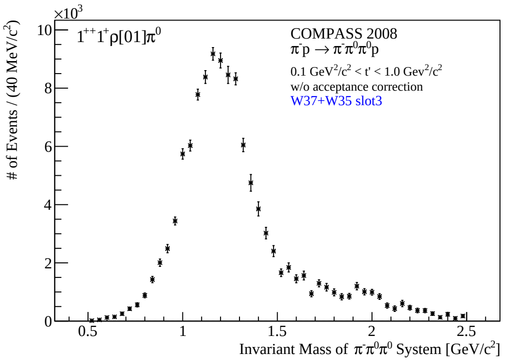

(a) Intensity of $1^-1^{++}1^+\rho(770)[01]\pi^0$ wave.

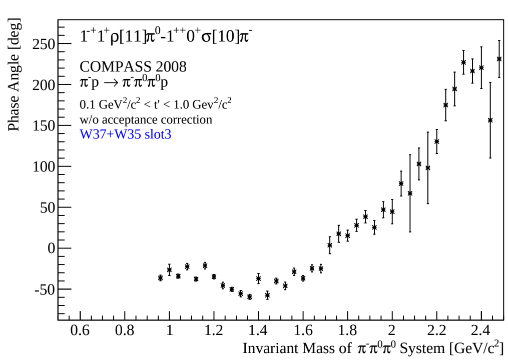

(b) Relative phase angle between the $1^-1^{-+}1^+\rho(770)[11]\pi^0$ and $1^-1^{++}0^+\sigma[10]\pi^-$ wave.

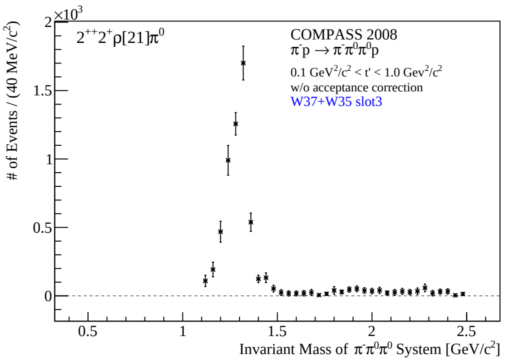

(c) Intensity of $1^-2^{++}2^+\rho(770)[21]\pi^0$ wave.

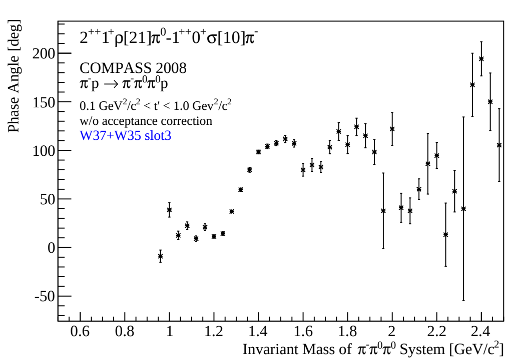

(d) Relative phase angle between the $1^-2^{++}2^+\rho(770)[21]\pi^0$ and $1^-1^{++}0^+\sigma[10]\pi^-$ wave.

Figure C.1

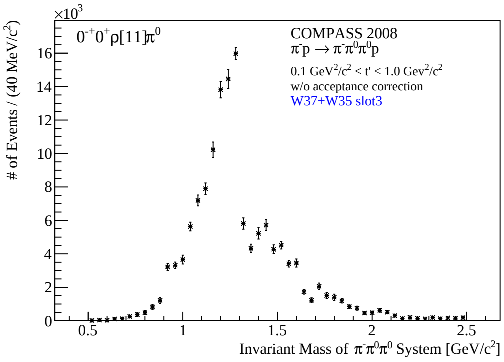

(a) Intensity of $1^-0^{-+}0^+\rho(770)[11]\pi^0$ wave.

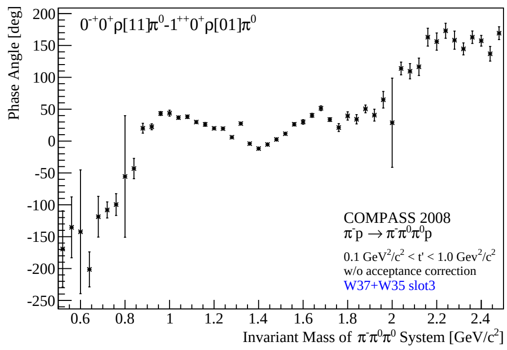

(b) Relative phase angle between the $1^-0^{-+}0^+\rho(770)[11]\pi^0$ and $1^-1^{++}0^+\rho(770)[01]\pi^0$ wave.

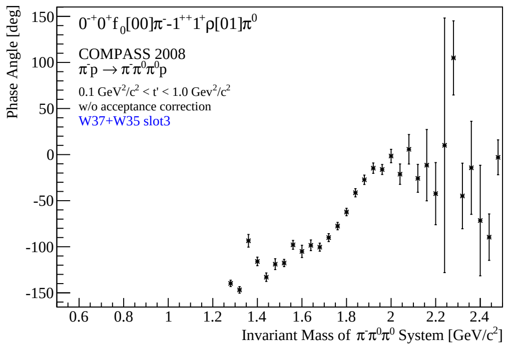

(c) Relative phase angle between the $1^-0^{-+}0^+f_0(980)[00]\pi^-$ and $1^-1^{++}0^+\rho(770)[01]\pi^0$ wave.

Figure C.2

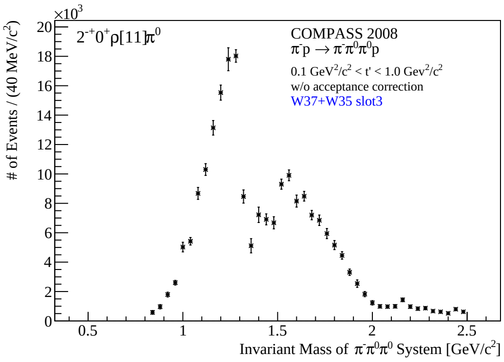

(a) Intensity of $1^-2^{-+}0^+\rho(770)[11]\pi^0$ wave.

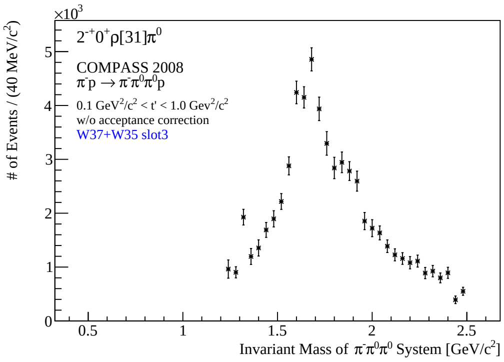

(b) Intensity of $1^-2^{-+}0^+\rho(770)[31]\pi^0$ wave.

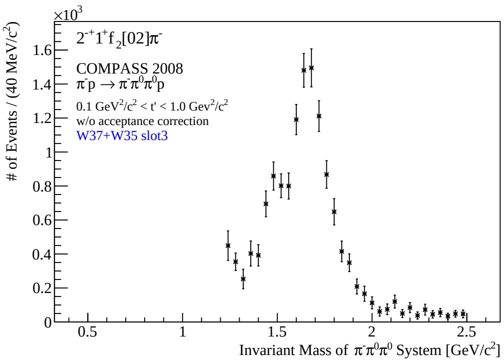

(c) Intensity of $1^-2^{-+}1^+f_2(1270)[02]\pi^-$ wave.

Figure C.3

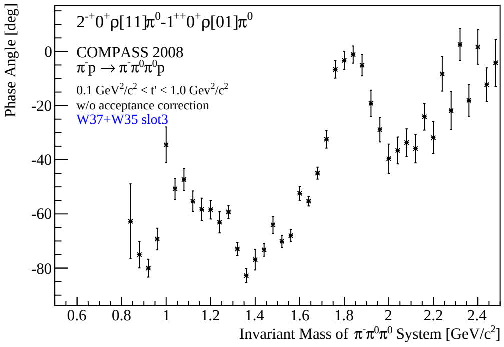

(a) Relative phase angle between the $1^{-}2^{-+}0^{+}\rho(770)[11]\pi^{0}$ and $1^{-}1^{++}0^{+}\rho(770)[01]\pi^{0}$ wave.

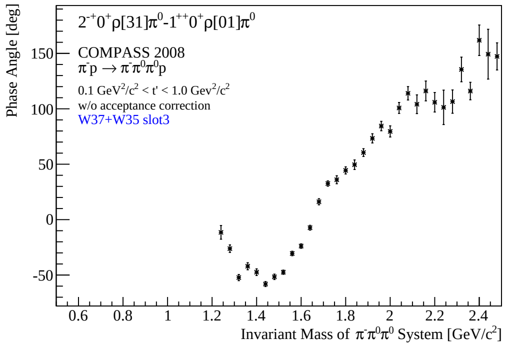

(b) Relative phase angle between the $1^{-}2^{-+}0^{+}\rho(770)[31]\pi^{0}$ and $1^{-}1^{++}0^{+}\rho(770)[01]\pi^{0}$ wave.

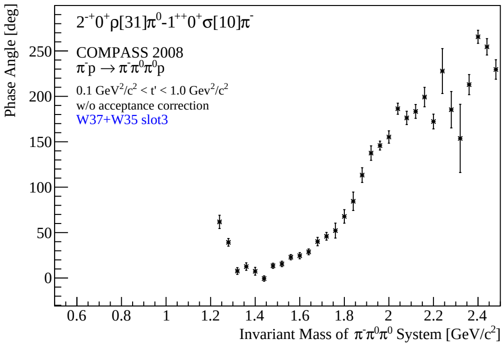

(c) Relative phase angle between the $1^{-}2^{-+}0^{+}\rho(770)[31]\pi^{0}$ and $1^{-}1^{++}0^{+}\sigma[10]\pi^{-}$ wave.

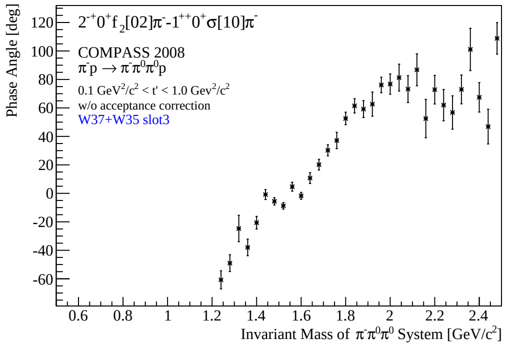

(d) Relative phase angle between the $1^{-}2^{-+}0^{+}f_2(1270)[02]\pi^{-}$ and $1^{-}1^{++}0^{+}\sigma[10]\pi^{-}$ wave.

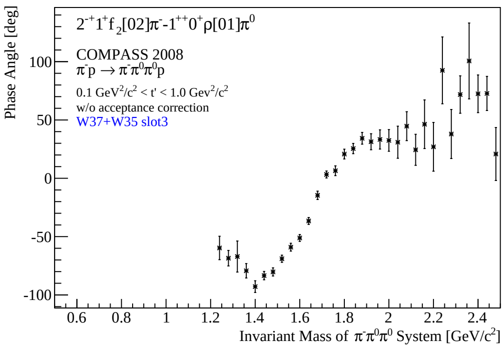

(e) Relative phase angle between the $1^{-}2^{-+}1^{+}f_2(1270)[02]\pi^{-}$ and $1^{-}1^{++}0^{+}\rho(770)[01]\pi^{0}$ wave.

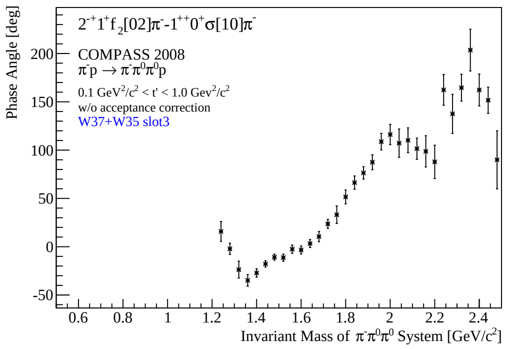

(f) Relative phase angle between the $1^{-}2^{-+}1^{+}f_2(1270)[02]\pi^{-}$ and $1^{-}1^{++}0^{+}\sigma[10]\pi^{-}$ wave.

Figure C.4

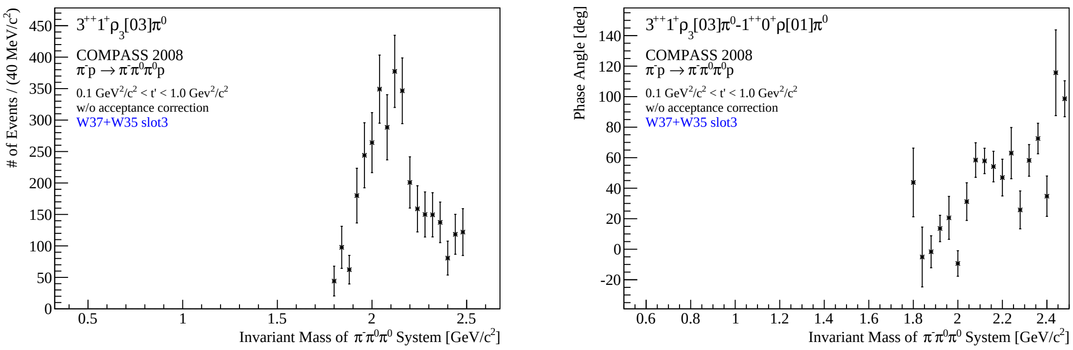

(a) Intensity of $1^{-}3^{++}1^{+}\rho_3(1690)[03]\pi^0$ wave.

(b) Relative phase angle between the $1^{-}3^{++}1^{+}\rho_3(1690)[03]\pi^0$ and $1^{-}1^{++}0^{+}\rho(770)[01]\pi^0$ wave.

Figure C.5

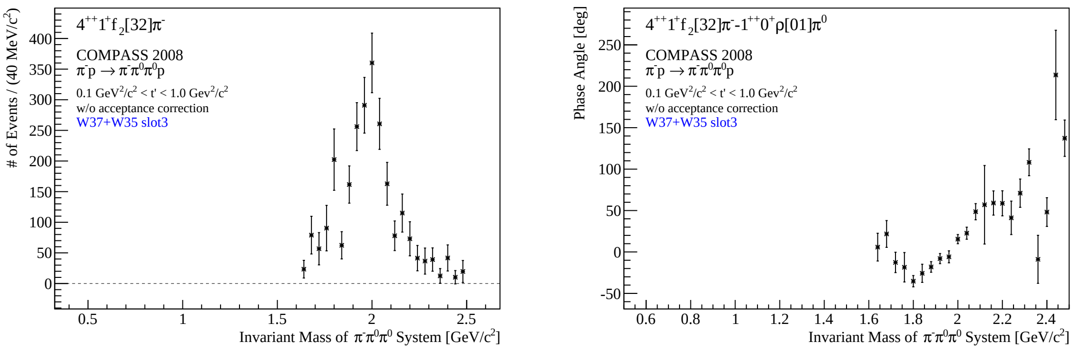

(a) Intensity of $1^{-}4^{++}1^{+}f_2(1270)[32]\pi^-$ wave.

(b) Relative phase angle between the $1^{-}4^{++}1^{+}f_2(1270)[32]\pi^-$ and $1^{-}1^{++}0^{+}\rho(770)[01]\pi^0$ wave.

Figure C.6

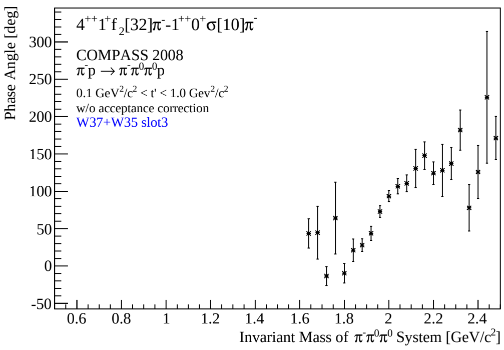

(a) Relative phase angle between the $1^-4^{++}1^+f_2(1270)[32]\pi^-$ and $1^-1^{++}0^+\sigma[10]\pi^-$ wave.

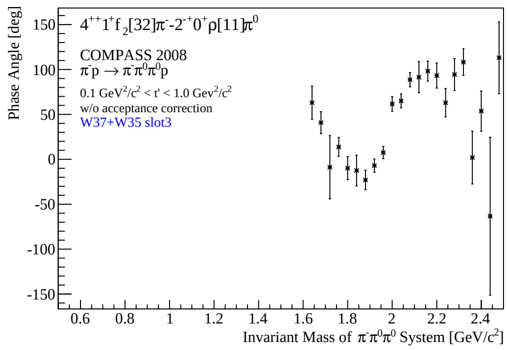

(b) Relative phase angle between the $1^-4^{++}1^+f_2(1270)[32]\pi^-$ and $1^-2^{-+}0^+\rho(770)[11]\pi^0$ wave.

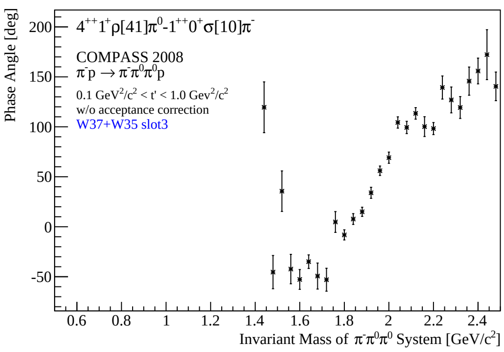

(c) Relative phase angle between the $1^-4^{++}1^+\rho(770)[41]\pi^0$ and $1^-1^{++}0^+\sigma[10]\pi^-$ wave.

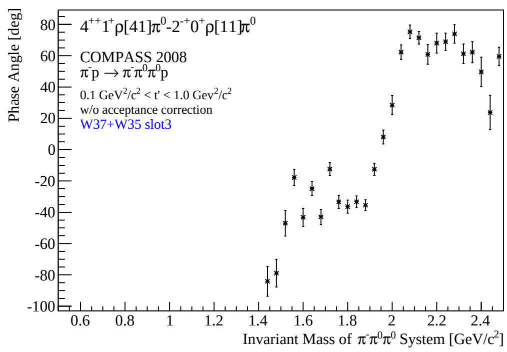

(d) Relative phase angle between the $1^-4^{++}1^+\rho(770)[41]\pi^0$ and $1^-2^{-+}0^+\rho(770)[11]\pi^0$ wave.

Figure C.7

Bibliography

[1] http://atlas.ch/etours_exper/images/decay_chart.gif.

[2] http://compassweb.ts.infn.it/rich1/jarda/Presentations/SPIN2008_Prague/nerlingCalorimetrySpinPraha08.pdf.

[3] http://en.wikipedia.org/wiki/Quark_model.

[4] http://public.web.cern.ch/public/en/research/AccelComplex-en.html.

[5] http://wwwcompass.cern.ch/compass/open_meetings//pre_villars_040702/Leberig_02-07-04.pdf.

[6] wwwkph.kph.uni-mainz.de/Compass/publikationen/DPG_09_bernhard.pdf.

[7] Gluon polarization in the nucleon from quasi-real photoproduction of high-pt hadron pairs. *Physics Letters B*, 633(1):25 – 32, 2006.

[8] A new measurement of the collins and sivers asymmetries on a transversely polarised deuteron target. *Nuclear Physics B*, 765(1-2):31 – 70, 2007.

[9] S. U. Chung. Techniques of amplitude analysis for two-pseudoscalar systems. *Phys.Rev.D*, 56(11):7299, 1997.

[10] S. U. Chung and T.L. Trueman. Positivity conditions on the spin density matrix: A simple parametrization. *Phys.Rev.D*, 11(3):633, 1975.

[11] S.U. Chung. Diffractive Dissociation for COMPASS (Version II). Appendix B, April 2008.

[12] Nils A. Törnqvist Claude Amsler. Mesons beyond the naive quark model. *Physics Reports*, 389:61–117, 2004.

[13] Jan Friedrich COMPASS collaboration. Tests of chiral perturbation theory with COMPASS. *AIP Conference Proceedings*, 1322(1):457–462, 2010.

[14] The COMPASS Collaboration. The COMPASS setup for physics with hadron beams. In Progress.

[15] P.D.B. Collins. *Introduction to Regge Theory*. Cambridge University Press, 1977.

[16] R.T. Deck. Kinematical interpretation of the first π-ρ resonance. *Phys. Rev. Lett.*, 13:169–173, 1964.

[17] P. Abbon et al. The COMPASS experiment at CERN. *Nuclear Instruments and Methods in Physics Research A*, 577:455–518, 2007.

[18] V. Palmieri et al. The COMPASS experiment at CERN. *Nuclear Instruments and Methods in Physics Research A*, 413:475–478, 1998.

[19] A. D. Martin F. Halzen. *Quarks and Leptons*. John Wiley & Sons, 1984.

[20] Jan Friedrich. Private communications.

[21] Particle Data Group. Review of particle physics. *Journal of Physics G*, 37(7A):184–192, 2010.

[22] N. Isgur and J. E. Paton. A flux tube model for hadrons in qcd. *Phys.Rev.*, D(31):2910, 1985.

[23] R. L. Jaffe and K. Johnson. Unconventional states of confined quarks and gluons. *Phys. Lett.*, B(60):201–204, 1976.

[24] Eberhard Klempt and Alexander Zaitsev. Glueballs, hybrids, multiquarks experimental facts versus QCD inspired concepts. *Physics Reports*, 454:1–202, 2007.

[25] Frank Nerling. Diffractive dissociation into 3 pion final states - neutral mode: $\pi^- + p \to \pi^-\pi^0\pi^0 + p$. 2009.

[26] B. R. Pollard W. M. Gibson. *Symmetry principles in elementary particles physics*, page 251ff. Cambridge University Press, 1976.

[27] S. Weinberg. *The Quantum Theory of Fields - Foundations*, volume I, chapter 5. Cambridge University Press, 2005.

[28] Quirin Weitzel. *Precision Meson Spectroscopy: Diffractive Production at COMPASS and Development of a GEM-based TPC for PANDA*. PhD thesis, TUM, 2008.

[29] K. G. Wilson. Confinement of quarks. *Phys.Rev.*, D(10):2445–2459, 1974.

Acknowledgements

First of all my sincerest thanks go to Prof. Stephan Paul for giving me the opportunity to work on this interesting topic. I have enjoyed working in his group a lot.

A special thanks goes to my proof reading staff Dr. Boris Grube, Florian Haas and Dr. Bernhard Ketzer, for their patience and very instructive criticism.

I want to point out the tremendous mentoring efforts of Dr. Boris Grube, Florian Haas and Sebastian Neubert and would like to express my deepest gratitude for their help, lectures and guidance throughout the year, even though I must have bothered them once or twice. I have learned incredibly much from them.

Furthermore, I am grateful for several computer related lessons from Sebastian Uhl and Julian Taylor. I also like to thank Dr. Dimitry Ryabchikov, Dr. Suh Urk Chung, Dr. Jan Friedrich, Dr. Bernhard Ketzer and Christian Höppner for several interesting and fruitful discussions and lectures. Also I would like to thank my work room mate Sverre Dørheim for his help particularly in the first weeks.

Next I would like to thank the whole E18 and COMPASS group for their hospitality and nice working atmosphere. Also I would like to thank Dr. Frank Nerling for his kind collaboration.

Last but not least, I would like to thank my whole family, most importantly my Mom and Dad, for supporting me throughout my whole studies. Also I'd like to thank my deceased grandfather Alex, who always strived to motivate me and work to the best of my abilities and would have loved to see my work.

Thank you all!